UNIVERSITY OF ILLINOIS
URBANA

AERONOMY REPORT NO. 56

PARTIAL-REFLECTION STUDIES OF D-REGION WINTER VARIABILITY

by
B. W. Denny
S. A. Bowhill

October 1, 1973

Supported by
National Aeronautics and Space Administration
Grant NGR 14-005-181

Aeronomy Laboratory
Department of Electrical Engineering
University of Illinois
Urbana, Illinois

CITATION POLICY

The material contained in this report is preliminary information circulated rapidly in the interest of prompt interchange of scientific information and may be later revised on publication in accepted aeronomic journals. It would therefore be appreciated if persons wishing to cite work contained herein would first contact the authors to ascertain if the relevant material is part of a paper published or in process.

UILU-Eng-73-2506

A E R O N O M Y R E P O R T

N O. 56

PARTIAL-REFLECTION STUDIES OF *D*-REGION WINTER VARIABILITY

by

B. W. Denny
S. A. Bowhill

October 1, 1973

Supported by
National Aeronautics and Space Administration
Grant NGR 14-005-181

Aeronomy Laboratory
Department of Electrical Engineering
University of Illinois
Urbana, Illinois

ABSTRACT

D-region electron densities were measured from December, 1972, to July, 1973, at Urbana, Illinois (latitude 40.2°N) using the partial-reflection technique. During the winter, electron densities at altitudes of 72, 76.5, and 81 km show cyclical changes with a period of about 5 days that are highly correlated between these altitudes, suggesting that the mechanism responsible for the winter anomaly in *D*-region ionization applies throughout this height region.

From January 13 to February 3, a pronounced wave-like variation occurred in the partial-reflection measurements, apparently associated with a major stratospheric warming that developed in that period. During the same time period, a traveling periodic variation is observed in the 10-mb height; it is highly correlated with the partial-reflection measurements. Electron-density enhancements occur approximately at the same time as increases in the 10-mb height.

Comparison of A1 and A3 absorption measurements with electron-density measurements below 82 km indicates that the winter anomaly in D-region ionization is divided into two types. "Type 1", above about 82 km, extends horizontally for about 200 km while "Type 2", below about 82 km, extends for a horizontal scale of at least 1000 km.

Diurnal partial-reflection measurements and monthly median electron-density profiles are also presented.

TABLE OF CONTENTS

Page

LIST OF TABLES

LIST OF FIGURES

1. INTRODUCTION

1.1 *Ionospheric Nomenclature*

The part of the atmosphere where ions and electrons are present in sufficient quantities to affect the propagation of radio waves is defined as the ionosphere. At one time, it was believed that the ionosphere had a layered structure with a maximum of electron density occurring in each layer. However, rocket observations revealed a nearly monotonic increase in electron density. *D* region, *E* region, and *F* region are the terms used to refer to the altitude regions below 90 km, from 90 to 160 km, and above 160 km, respectively.

The division of the ionosphere into three regions is attributed to Appleton. The *E* region was detected by reflected radio waves; as techniques improved, the *F* region was found. Appleton observed that a radio wave propagating in the ionosphere suffered an attenuation below the reflecting *E* region. He attributed this effect to an ionized region which he called the *D* region.

1.2 D-*Region Morphology and Processes*

1.2.1 *Ion-electron pair production.* Ionizing radiations from the sun and from the galaxy penetrate the earth's atmosphere and, as a consequence, produce ions and electrons. The energy of the radiation and the composition of the atmosphere at the altitude of ionization determines the nature of the ion-electron pairs produced. The altitude at which the solar flux attenuates to $1/e$ of its original intensity above the atmosphere with an overhead sun is shown in Figure 1.1. The wavelengths above 1900 Å penetrate into the *D* region, but they can ionize only the atmospheric metal atoms due to their low photon energy. However, the scarcity of such constituents prevents this process from contributing appreciably to the ionization in the *D* region.

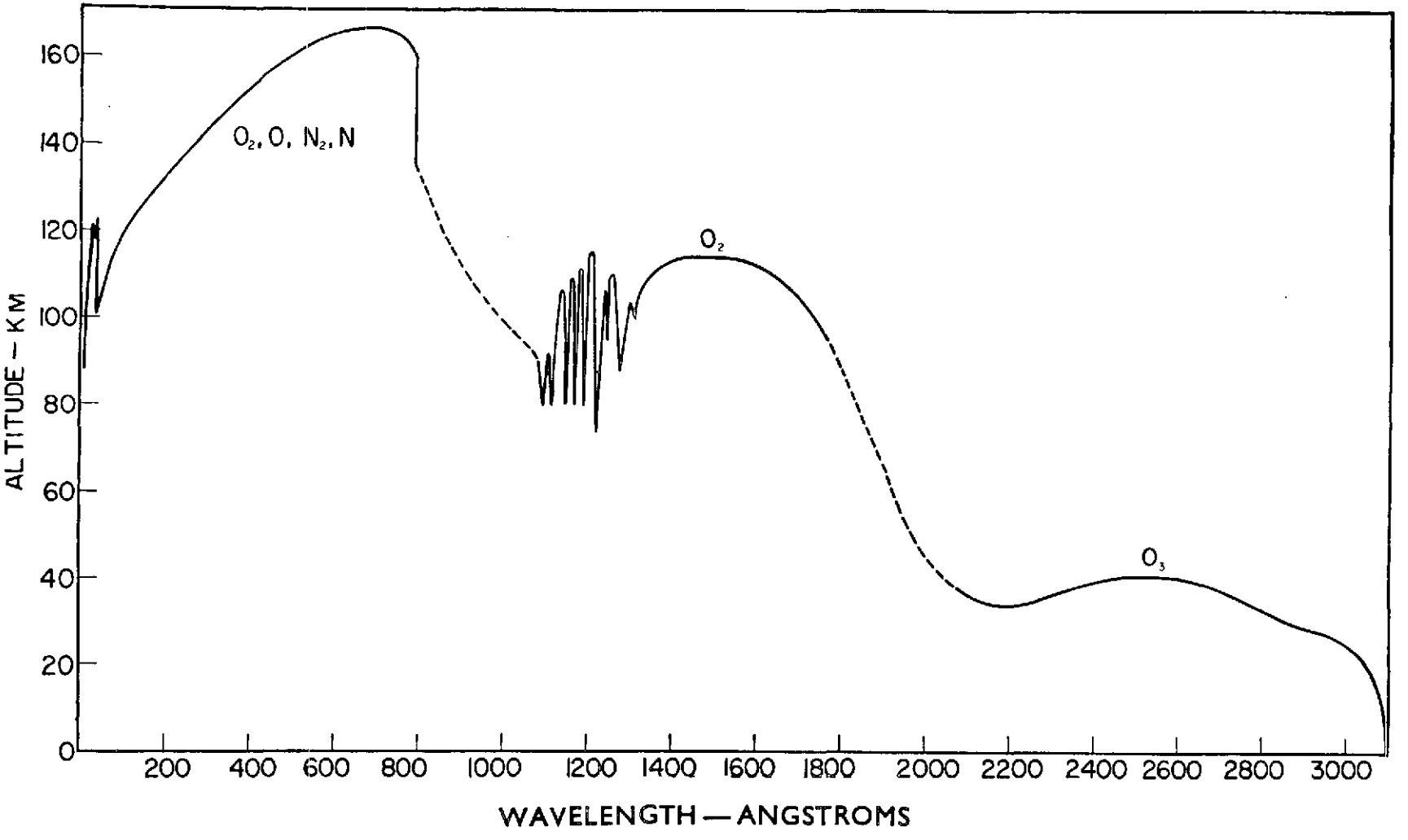

Figure 1.1 Penetration of solar radiation into the atmosphere [*Friedman*, 1960].

There are four types of radiation that are accepted as the principal contributors to ionization in the *D* region: Lyman-α radiation, solar X-radiation, galactic cosmic radiation (GCR), and extreme ultraviolet radiation (EUV) [*Whitten and Poppoff*, 1971]. Secondary sources of ionization are visible and ultraviolet solar radiation which can provide the energy to detach weakly held electrons from negative ions. Solar X-rays less than 10 Å are capable of ionizing all atmospheric constituents, but O_2 and N_2 are the major constituents in the *D* region. The Lyman-α emission line is coincidental with one of the atmospheric absorption windows between 1100-1300 Å. Lyman-α at 1216 Å (10.2 eV) can ionize only minor constituents, and nitric oxide is the most important of these. GCR in the form of very energetic charged particles is the dominant ionizing process of all atmospheric constituents from 50 to 70 km in the *D* region. EUV radiation in the band 1027 to 1118 Å will ionize oxygen molecules that are excited to the metastable state $O_2(^1\Delta_g)$ [*Whitten and Poppoff*, 1971].

The relative importance of each radiation depends on the position of the solar cycle, the fluxes of the different ionizing radiations, and the types and concentrations of the constituents. At solar minimum, Lyman-α is considered the strongest of the four ionizing radiations in terms of total energy above the earth's atmosphere; it is approximately three to five orders of magnitude greater than the solar X-radiation flux (< 10 Å) and more than one order of magnitude greater than the flux in the EUV radiation band 1027 to 1118 Å [*Whitten and Poppoff*, 1971]. At solar maximum, the solar X-radiation flux may increase by a factor of 10^3 from its solar minimum value, while the Lyman-α radiation flux may increase by only about 50 per cent. However, between solar minimum and maximum, GCR flux becomes weaker by a factor of about one-half. This effect is attributed to the deviation of GCR particles from the earth by the stronger solar magnetic field at solar maximum [*Ratcliffe*, 1972]. At

solar maximum, the relative importance of the solar X-radiation and Lyman-α radiation are close to equal in ion-electron production. The relative importance of each ionization source is shown in Figure 1.2.

There are other processes which play a significant role in the day-to-day variation of electron density, but they will be discussed later.

1.2.2 *Ion chemistry.* Immediately following the production of ion-electron pairs, several types of reactions occur; one type causes a change in ionic species while other types are ion and/or electron loss reactions. For a better understanding of the ion chemistry, the positive and negative ions can be arranged into the electrochemical series of Tables 1.1 and 1.2, respectively. The positive ions are arranged according to their ionization potentials while the negative ions are arranged according to their electron affinity. Positive ions with a high ionization potential have a greater tendency to gain an electron while negative ions with low electron affinity have a greater possibility of losing an electron.

Solar photons with sufficient energy can ionize neutral particles and create the positive ions of Table 1.1; these photons can also remove negative ions from Table 1.2 by photodetachment

$$X^- + h\nu \rightarrow X + e \tag{1.1}$$

where the symbols X, Y, etc. denote an atom or a molecule.

Reactions between electrons, ions, and neutral particles are important in the *D* region due to their comparatively frequent collisions. Among the reactions that play a significant role in the *D*-region ion chemistry are electron loss processes as three-body recombination

$$X^+ + e + M \rightarrow X + M \tag{1.2}$$

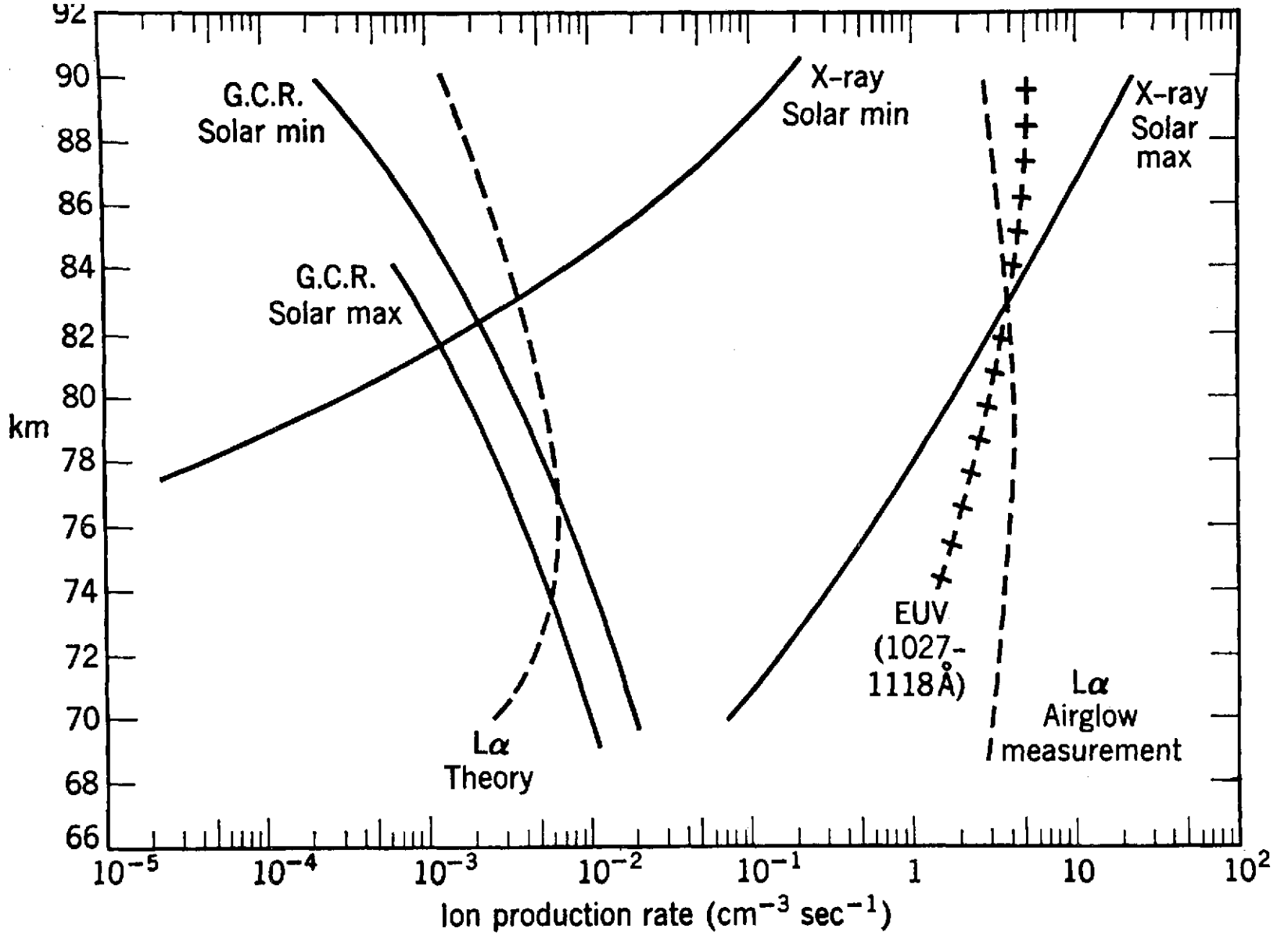

Figure 1.2 Illustrative example of ion production rates for GCR, X-ray, Lyman-α, and EUV (1027 - 1118 Å). The Lyman-α curves are shown for theoretical and measured NO concentrations; the GCR and X-ray curves are shown over a solar cycle [*Whitten and Poppoff*, 1971].

TABLE 1.1

Electrochemical series for positive ions [*Bowhill*, 1969].

Ion Produced	Ionization Potential eV	Wavelength Angstrom
N_2^+	15.6	790
H_2^+	15.4	803
N^+	14.5	852
CO^+	14.0	882
CO_2^+	13.8	895
O^+	13.6	910
H^+	13.6	910
OH^+	13.3	930
N_2O^+	12.9	960
O_3^+	12.8	970
H_2O^+	12.6	980
O_2^+	12.0	1030
O_2^+ from $O_2(^1\Delta_g)$	11.1	1118
NO_2^+	9.78	1260
NO^+	9.27	1330

TABLE 1.2

Electrochemical series for negative ions.

Negative Ion	Electron Affinity eV	Wavelength Angstrom	Reference
NO^-	0.09	140,000	*Berkowitz, et al.*, 1971
O_2^-	0.48	26,000	*Berkowitz, et al.*, 1971
CO_4^-	1.22	10,100	*Bowhill*, 1969
O^-	1.47	8,600	*Bowhill*, 1969
OH^-	1.83	6,750	*Bowhill*, 1969
O_3^-	1.96	6,300	*Berkowitz, et al.*, 1971
CO_3^-	Unknown		
NO_2^-	$1.8 < EA < 3.8$	<6,900	*Thomas*, 1971
NO_3^-	$> EA(NO_2) + 0.9$	<4,600	*Thomas*, 1971

where the symbol M denotes a neutral particle that does not take part in the chemical reaction; it is needed for the conservation of energy and momentum. Free electrons may also be lost by three-body attachment

$$X + e + M \rightarrow X^- + M \tag{1.3}$$

or radiative attachment

$$X + e \rightarrow X^- + h\nu \ . \tag{1.4}$$

The last significant electron loss reaction is dissociative recombination

$$XY^+ + e \rightarrow X^* + Y^* \tag{1.5}$$

where the asterisks indicate the atoms or molecules may be left in an excited state.

Some reactions that are considered as secondary electron production sources are collisional detachment

$$X^- + M \rightarrow X + M + e \tag{1.6}$$

and associative detachment

$$X^- + Y \rightarrow XY + e \ . \tag{1.7}$$

Associative detachment is a process whereby a negative ion is removed from Table 1.2 by a reaction with an active neutral constituent. The associative and collisional detachment reactions occur predominantly with negative ions at the top of Table 1.2 due to their low electron affinity.

Two reactions that involve only ions and neutral constituents are ion-ion recombination

$$X^+ + Y^- \rightarrow X + Y \tag{1.8}$$

and charge exchange

$$X^+_- + Y \rightarrow X + Y^+_- \tag{1.9}$$

The negative or positive ion produced by a charge-exchange reaction must be lower in the electrochemical series of Table 1.1 or 1.2 than the ion present before the reaction.

The principal positive ions formed directly by ionization are O_2^+, N_2^+, and NO^+. By charge-exchange reactions, there tends to be an accumulation of positive ions at the bottom of the electrochemical series (the same occurs with negative ions). The N_2^+ ion does not exist in significant quantities, because it reacts very rapidly with O_2 in a charge-exchange reaction. The resulting O_2^+ ion will react with NO to transfer a charge, but a large concentration of O_2^+ is still expected to exist, since the concentration of NO is small.

With a mass-spectrometer analysis of the positive ions in the *D* region, *Narcisi and Bailey* [1965] demonstrated that O_2^+ and NO^+ were the predominant ions above 82 km. They also detected metallic ions and water cluster ions. *Donahue* [1972] gives a reaction scheme shown in Figure 1.3 for the conversion of O_2^+ and NO^+ to water cluster ions. The chain beginning with O_2^+ works effectively to remove O_2^+ and build up the hydrates rapidly because of the adequate speed of the initial clustering reaction

$$O_2^+ + O_2 + M \rightarrow O_4^+ + M \tag{1.10}$$

and because the subsequent clustering reactions of the chain are between two bodies:

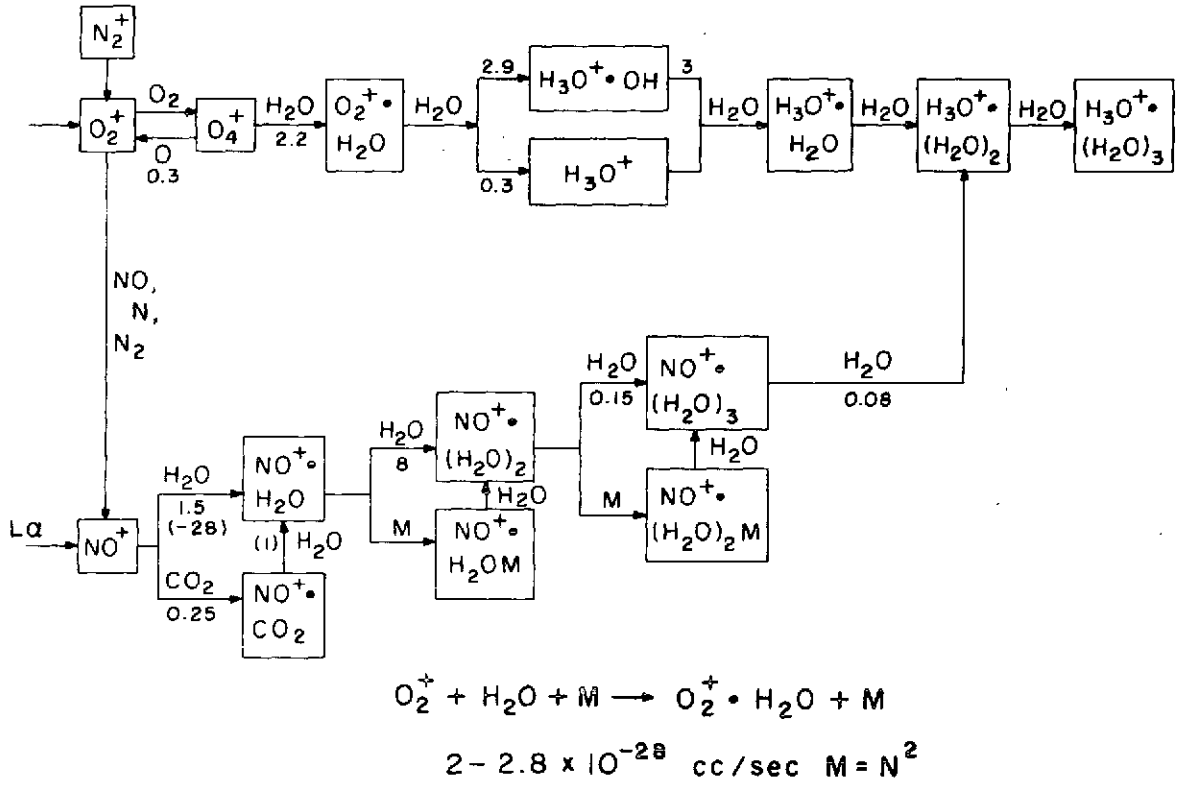

Figure 1.3 Reaction scheme for conversion of O_2^+ and NO^+ to hydrates. Three-body rate constants in units of 10^{-28} cm^6 sec^{-1}, two-body rate constants in units of 10^{-9} cm^3 sec^{-1} [*Donahue*, 1972].

$$O_4^+ + H_2O \rightarrow O_2^+ \cdot H_2O + O_2 \tag{1.11}$$

$$O_2^+ \cdot H_2O + H_2O \rightarrow H_3O^+ \cdot OH + O_2$$
$$\rightarrow H_3O^+ + OH + O_2 \tag{1.12}$$

$$H_3O^+ \cdot OH + H_2O \rightarrow H_3O^+ \cdot H_2O + OH \tag{1.13}$$

The chain beginning with NO^+ is based on the formation of the cluster $NO^+ \cdot H_2O$ in a three-body reaction, growth of the degree of hydration, and a switching reaction

$$NO^+ \cdot (H_2O)_3 + H_2O \rightarrow H_3O^+ \cdot (H_2O)_2 + HNO_2 \tag{1.14}$$

The scheme of Figure 1.3 is promising due to the large rate of production of O_2^+ ions down to 75 km provided by the ionization of $O_2(^1\Delta_g)$ molecules. Another promising feature is the reaction

$$O_4^+ + O \rightarrow O_2^+ + O_3 \tag{1.15}$$

which regenerates O_2^+ from O_4^+, thus controlling the production of the cluster ions. The sudden disappearance of cluster ions above 80 km is associated with an increased occurrence of reaction 1.15 due to an increased O concentration.

Donahue points out that the $NO^+ \rightarrow H_3O^+ \cdot (H_2O)_2$ procedure has some problems. The first hydrate created is $H_3O^+ \cdot (H_2O)_2$, having a mass of 55. However, the dominant species detected are 19^+ and 37^+; therefore, either the hydrates of mass greater than 37 fragment before they are measured by the mass spectrometer, or there is some unknown reaction which changes the NO^+ hydration scheme.

Another problem with the NO^+ hydration scheme is that the conversion of NO^+ to the hydrates via the three-body steps is too slow relative to dissociative recombination of the cluster ions, which causes a dominance of NO^+ relative to the hydrates at 80 km contrary to observation. At 70 km, this difficulty disappears because the three-body reactions converting NO^+ to hydrates become dominant compared to recombination.

A problem in the O_2^+ hydration scheme, according to *Donahue* [1972], is that it is based on an overestimated $O_2(^1\Delta_g)$ ionization rate below 77 km. The supply of O_2^+ drops drastically below 77 km due to a reduction of $O_2(^1\Delta_g)$ ionization. This causes the predicted hydrate concentrations to be much less than those observed.

Thus, the proposed scheme of Figure 1.3 might explain the measured water cluster ions if Lyman-α ionized NO only weakly above 75 km. The O_2^+ scheme would provide the cluster ions above 75 km while NO^+ would become the ancestor ion below 75 km. Donahue suggests that one possible explanation for Lyman-α only weakly ionizing NO above 75 km is that the Lyman-α photon does not directly ionize NO but rather causes an excited state with a relatively long lifetime against autoionization in contrast with fluorescence.

Thomas [1971] presents a block diagram illustrating the negative-ion reaction scheme at 65 km shown in Figure 1.4. It shows the lifetimes of electrons and negative ions, the reactants involved, and the number of the reaction, according to the list shown in Appendix I. The lifetimes are based on assumed concentrations for the reactants.

Thomas' model predicts a rapid change from O_2^- to CO_3^- ions, via O_3^- or O_4^- and CO_4^-. However, these CO_3^- ions undergo fast reactions with O to restore some of the O_2^- ions. Slower reactions of O_4^- or CO_4^- with NO produce the terminating ion NO_3^-. NO_3^- is also produced by the slow reactions beginning with CO_3^-.

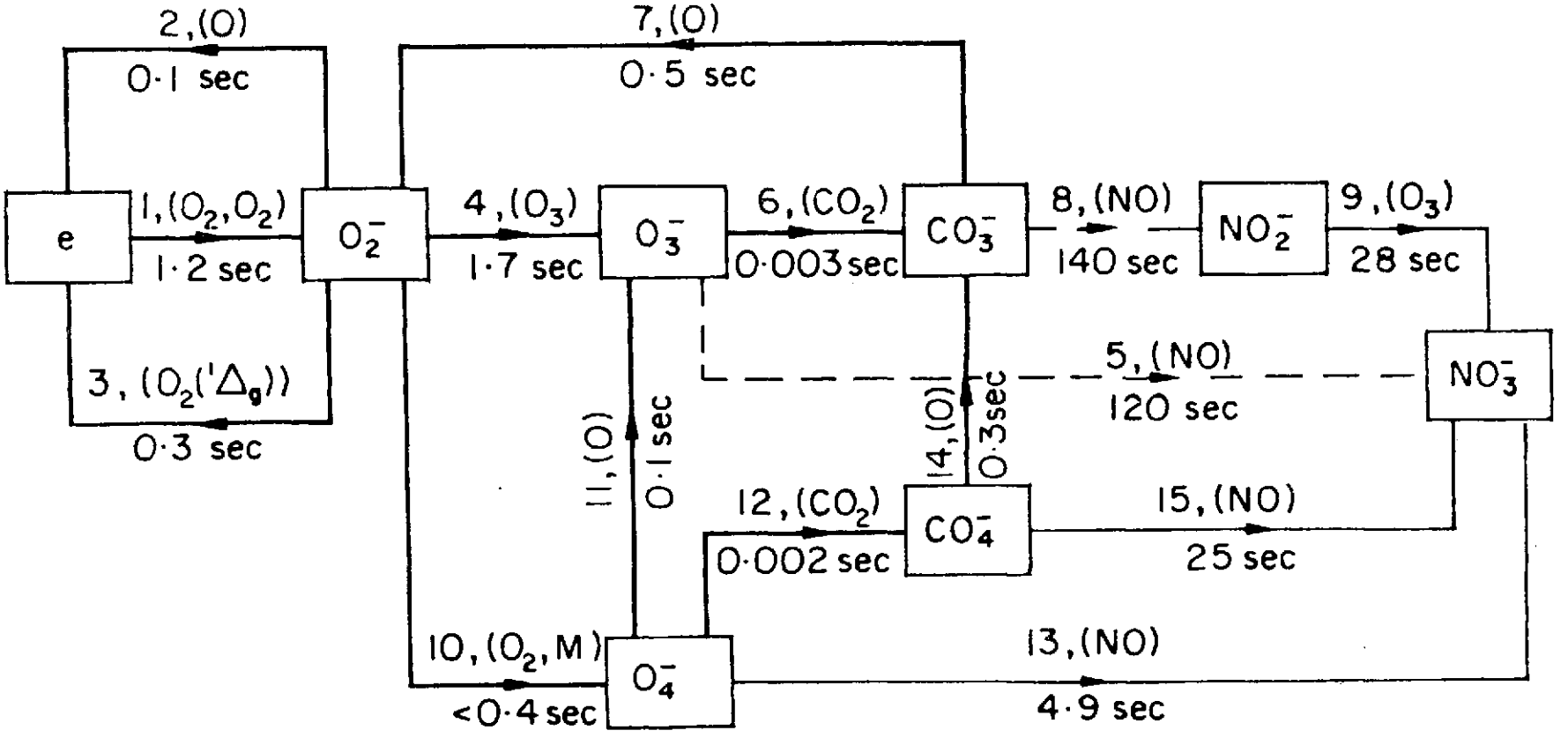

Figure 1.4 Negative-ion reaction scheme with lifetimes and reactants involved. Reactions are listed by number in Appendix I. [*Thomas*, 1971].

Ferguson [1972] points out that a feature not included in the negative-ion scheme is the hydration of long-lived ions. Hydration of the negative ions may not occur primarily by direct three-body association with H_2O molecules. Ions such as NO_3^- might first cluster to N_2, O_2, or CO_2 and then rapidly undergo a switching reaction with H_2O.

1.3 *History of Partial-Reflection Experiment*

1.3.1 *Other experimental facilities.* The weak reflections from the *D* region have been detected by several observers, but the technique has been used extensively by only a few groups to deduce electron densities. *Gardner and Pawsey* [1953] were the first to perform the experiment in its present form. They demonstrated that the electron-density profile could be deduced if the reflections were caused by electron-density irregularities by assuming a collision-frequency profile and measuring the *D*-region reflected amplitudes for both the ordinary and extraordinary mode waves. By choosing a site with very low noise, they attained unusually high sensitivity. Their transmitter operated at a peak power of about 1 kilowatt, a frequency of 2.28 MHz, and a pulse width of 30 microseconds. The receiver was located 20 or 30 kilometers from the transmitter and operated with a noise factor of 1.3 dB and a bandwidth of 50 to 60 kHz. The transmitting antenna was a horizontal half-wave dipole, while the receiving antenna was circularly polarized using two perpendicular half-wave dipoles with coincident centers. Initially, observations were made visually using an amplitude versus height (A-scan) display on a cathode-ray oscilloscope. Due to the large dynamic range of reflections, the receiver was modified to give approximately a logarithmic response. A photographic system was later used to record the intensity-modulated display on continuous moving film.

Fejer and Vice [1959] did the partial-reflection experiment at two different frequencies: 1.83 and 2.63 MHz. The 1.83 MHz and 2.63 MHz transmitters operated at peak radiated powers of 320 kW and 10 kW, respectively. They transmitted and received on circularly polarized antennas; this innovation produced a large discrimination between the magnetoionic components. A double beam cathode-ray tube displayed the A-scan with one beam and height calibration marks with the other beam. Every 10 seconds both the ordinary and extraordinary A-scan were recorded on one photograph by double exposing each frame. While Gardner and Pawsey read the amplitudes at fixed height intervals, Fejer and Vice read the amplitude at distinct echoes which occurred at the same height for both modes of polarization.

Holt [1963] used a circularly polarized receiving antenna utilizing two mutually perpendicular horizontal half-wave dipoles for partial-reflection measurements from 1958 to 1962. The reflections were displayed on an oscilloscope with height calibration marks and photographed with one mode deflected upward and the other downward; 80 photographs were taken every minute. In determining the electron densities, Gardner and Pawsey used the Appleton-Hartree approximation of the magnetoionic theory. Holt demonstrated that the partial-reflection method also holds for the quasi-longitudinal approximation of the generalized Appleton-Hartree formulas [*Sen and Wyller*, 1960].

Beginning in the spring of 1961 to the present, *Belrose and Burke* [1964] used the partial-reflection technique extensively for daytime study of the *D* region. Many of the previous workers experienced difficulties due to insufficient transmitter power, lack of discrimination between magnetoionic components, or oblique reflections. Belrose and Burke attempted to eliminate these problems by using high transmitter power and directive antennas. 2.66 and 6.275 MHz transmitters were operated at 1000 kW and 100 kW, respectively.

The antenna systems consisted of two circularly polarized 4-dipole arrays for each frequency. Later, the 6.275 MHz and 2.66 MHz antennas were changed to 128-dipole and 40-dipole circularly polarized arrays, respectively. The reflections were recorded every 1 or 2 seconds photographically similar to Fejer and Vice. *Belrose and Burke* [1964] analyzed their A-scan records by reading the peak amplitudes of clean reflections which appeared at the same height for both modes of polarization. However, with the advent of a more sophisticated digital recording system, *Belrose* [1970] recorded the A-scan amplitudes for both the ordinary and extraordinary components in 2 km intervals for a 40 km height range on an incremental tape recorder. The height range was changed on alternate seconds to cover the range 34-70 km and 68-104 km.

The partial-reflection experiment has been done by several other groups. *Thrane, et al.* [1968] measured partial reflections during the International Quiet Sun Years 1963-64. *Gregory and Manson* [1969a] used a modified version of the photographic recording technique of Fejer and Vice for measuring partial reflections during an eclipse. With a high pulse repetition rate and an A-scan oscilloscope display, an attenuator was adjusted to match the ordinary and extraordinary amplitudes at a particular height. An advantage to this method is that only ratios of well correlated reflections were recorded, but it was inferior, because the reflected structure and amplitudes were not recorded.

For synoptic studies of the *D* region, a network of partial-reflection installations is required. Stations exist in Canada, Colorado, Illinois, and Pennsylvania, providing an adequate cover for North America. Adequate coverage of the earth would be provided if stations were added and routinely operated at the equator, Australia, New Zealand, and possibly the Antarctic.

1.3.2 *Urbana installation.* The instrumentation designed for vertical-incidence absorption and partial reflections on board the NASA Mobile Launch

Research Expedition to the South Pacific in 1965 was moved to Urbana in February, 1966, for use there.

The transmitter had a peak power of 50 kW, a pulse width of 50 microseconds, a frequency of 3.03 MHz, and a pulse repetition rate of 1-double pulse every two seconds. The receiver had a bandwidth of 55 kHz and a noise factor of about 2 dB. The receiving and transmitting antenna arrays were four half-wave center-fed dipoles in a square box arrangement.

After installation, noise measurements indicated a need for an additional 20 dB system gain. Increasing the transmitter power or larger antennas would have provided the additional gain; the latter was chosen, and construction was completed in April, 1967. Two identical 60-dipole arrays were constructed for transmission and reception. Each consisted of two sub-arrays of 30 parallel half-wave dipoles; the sub-arrays were perpendicular to each other. Testing of the new antennas indicated that greater than 45 dB gain was added to the system.

The ordinary and extraordinary A-scans were displayed with opposing polarities on an oscilloscope. They were recorded by photographing an ordinary and extraordinary A-scan per picture. A logarithmic amplifier was used at the receiver output to obtain a greater dynamic range of data on the recording film. A height mark generator was incorporated in the time-base circuit providing an intensified dot at regular intervals on the oscilloscope.

The amplitudes of the ordinary (A_o) and extraordinary (A_x) reflections were recorded at heights where distinct peaks were observed for both modes. Daily graphs of the A_x/A_o ratio were plotted, and on the days of sufficiently low noise, the electron-density profile was calculated using a computer program. The quasi-longitudinal approximation was used with the generalized Appleton-Hartree formulas. The collision-frequency model was determined from rocket

measurements during the flight of Nike-Apache 14.143 [*Mechtly, et al.*, 1967] on April 16, 1964. The initial results and more details are reported by *Pirnat and Bowhill* [1968].

The Urbana installation participated in the SOMED (Synoptic Observation of Mesospheric Electron Density) Network which provided the *D*-region electron densities at several stations during the winter of 1969-70. *Reynolds and Sechrist* [1970] developed a system to record the values of A_x and A_o at 75 and 80 km for the calculation of the average electron density between the altitudes. A noise gate was included in the system between 40 and 55 km on both A_x and A_o waveforms; frames of data with excessive noise were rejected. The four A_x and A_o values were recorded using four sample-and-hold circuits and control circuitry to punch the values on paper tape every two seconds. The data were later processed to give electron densities at 77.5 km.

A PDP-15/30 computer was acquired in late 1970 for on-line, real-time collection and reduction of partial-reflection data; an HP 5610A analog-to-digital converter was used to sample the ordinary and extraordinary waveforms. The initial results and system description are found in *Birley and Sechrist* [1971]. The system provided for the collection of 25 minutes of A_x and A_o amplitudes followed by 15 minutes of processing to calculate an electron-density profile from 60 to 90 km.

The Urbana partial-reflection instrumentation was moved to Wallops Island, Virginia, in January, 1972, for the winter-anomaly program. A smaller version of the Urbana 2.66 MHz antenna was erected on the north end of the island. The antenna consisted of 12-dipoles arranged in two horizontal arrays and was used for receiving and transmitting. Data were recorded in the morning to determine if an anomalous condition existed; if it did exist, rockets were fired, and

partial-reflection data were collected the entire day. The equipment was returned to Urbana in March, 1972.

Wiersma and Sechrist [1972] used the existing partial-reflection experiment with some modifications to make differential-phase partial-reflection measurements to deduce *D*-region electron-density profiles. The technique consisted of measuring the amplitudes of six polarizations—two circular and four linear. A special polarization-changing network was incorporated between the antennas and the transmitting and receiving equipment to obtain these polarizations. A collision-frequency profile was deduced from the electron densities calculated from differential phase and differential absorption.

1.4 *D-Region Electron-Density Variations*

1.4.1 *Winter anomaly.* *Chapman* [1931] developed a theory of layer formation in which he assumed that solar radiation was the only cause of photoionization of a particular atmospheric constituent. He predicts that the peak concentration (N_m) of electrons is dependent on the solar zenith angle χ:

$$N_m = K(\cos \chi)^{1/2} \tag{1.16}$$

where K is a constant. This theory predicts a maximum electron density for a given layer in the summer, and a minimum in winter, but N_m would be nearly constant at a given time on consecutive days.

Appleton [1937] tested Chapman's theory by using radio wave absorption as a measure of electron density. A radio wave reflected by the *E* or *F* layer would suffer absorption in the *D* region while propagating upward then downward. Appleton's experiment indicated a large disparity between the predicted and measured absorption during the winter months; more absorption was observed than predicted. This phenomenon was termed the *D*-region winter anomaly and later confirmed by several workers [*Appleton and Piggott*, 1948, 1954; *Beynon and*

Davies, 1954; and *Thomas*, 1962]. The additional absorption on anomalous days was ascribed to a higher electron content of the *D* region, and any one occurrence covered an area on the order of 10^6 km^2 [*Thomas*, 1962]. *Dieminger* [1952] also observed the excessive absorption on groups of days in winter; he suggests a meteorological explanation for this phenomenon. This explanation and others are discussed in Section 1.4.3.

The anomaly in the *D* region consists of two types: seasonal and daily. *Mechtly and Smith* [1968] examined the seasonal anomaly of the electron-density profile at Wallops Island using the combined rocket-borne probe and radio experiment. Figure 1.5 shows the electron-density profiles measured in June and December, 1965, at a solar zenith angle of 60°. It is evident that the summer electron densities are about a factor of four larger than the winter values between 65 to 85 km. *Gregory and Manson* [1969b] used the partial-reflection technique to investigate the seasonal anomaly at Christchurch, New Zealand. They found larger noon electron densities occurring in winter than summer between 79 and 88 km. When the electron densities were corrected to equivalent overhead conditions, the winter/summer ratio was 1.9 to 1. *Coyne and Belrose* [1972] also observed a seasonal anomaly at Ottawa, Canada. Their observations indicated that the winter and summer electron densities were similar at 73 and 77 km, but at 69 km the winter electron densities were much lower. At low latitudes where there is very little distinction between the seasons, a seasonal anomaly would not be expected. Indeed, *Shirke* [1961] at Ahmedabad, and *Ganguly* [1972] at Calcutta observed no anomaly. The above results indicate a seasonal anomaly, but the exact effect on the *D* region is hard to discern because of the difficulty in distinguishing a true seasonal anomaly from variations due to solar activity.

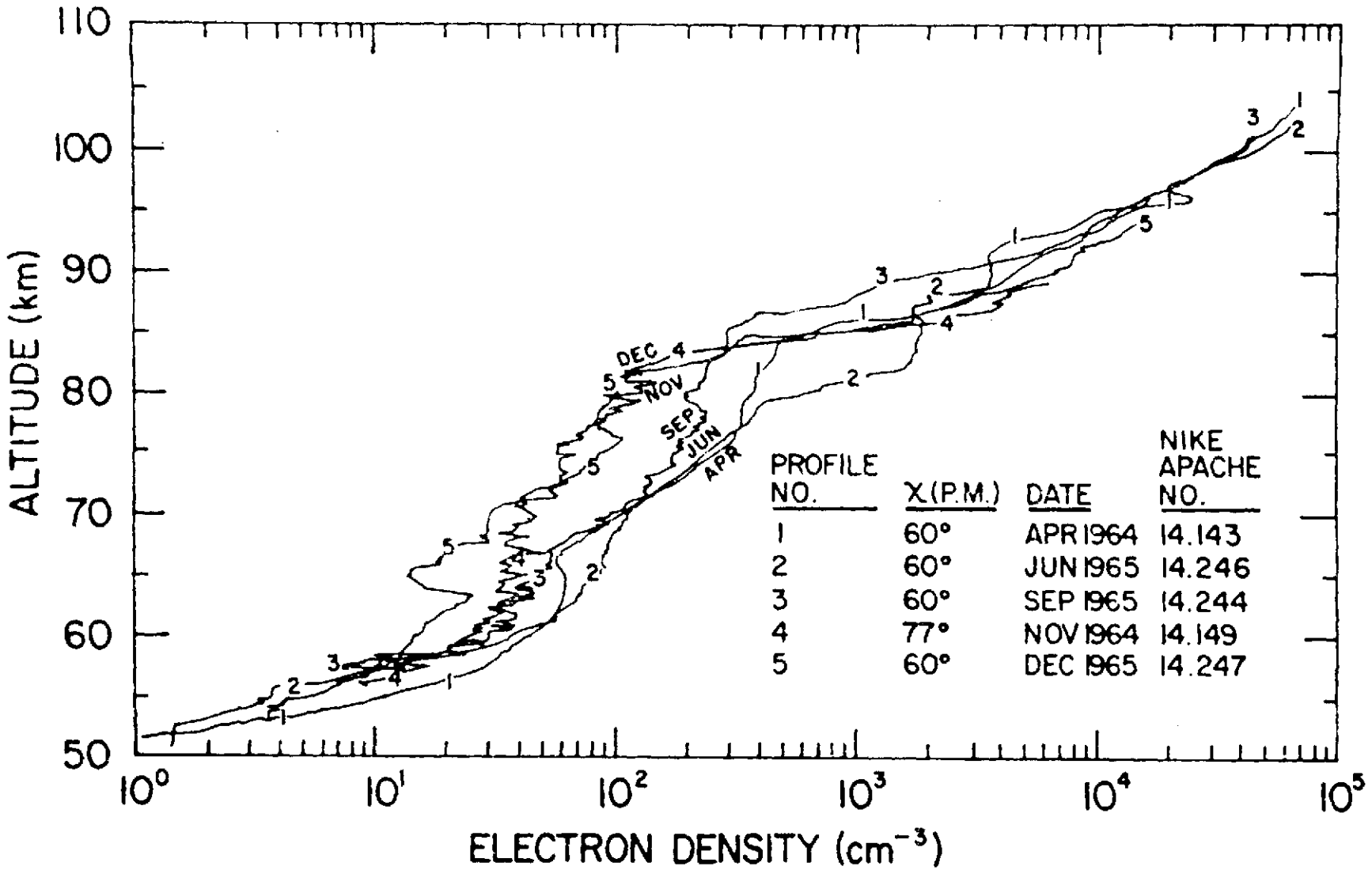

Figure 1.5 Electron-density profiles deduced at Wallops Island, by rocket-borne measurements. [*Mechtly and Smith*, 1968].

During the winter, the day-to-day fluctuations are not constant as Chapman's theory predicts. *Sechrist, et al.* [1969] showed from rocket results (Figure 1.6) that electron densities near 85 km increased by a factor greater than ten above the values for a normal day. This effect has also been observed using the partial-reflection experiment by *Gregory and Manson* [1969b] and *Belrose, et al.* [1966]. The daily fluctuations were much larger and more frequent in the winter months.

1.4.2 *Diurnal variation.* It is obvious from the processes that cause the *D*-region ionization that there will be differences between the daytime and nighttime ionosphere. The Chapman theory predicts a strong diurnal variation of electron density. As the sun drops below the horizon, production essentially ceases except for that due to GCR. Photodetachment also ceases and photochemical products begin to disappear. The attachment reaction is the loss process for electrons; however, some ionization still exists at night due to collisional and associative detachment. Also, small amounts of Lyman-α radiation can ionize NO because it is scattered into the night hemisphere by the hydrogen corona [*Whitten and Poppoff*, 1971].

Experimental results by *Thrane* [1969] indicated a diurnal variation at all altitudes of the *D* region while *Deeks* [1965] observed little change in the electron density at the lowest altitudes.

1.4.3 *Suggested causes of the winter anomaly.* *Dieminger* [1952] is perhaps the first to suggest a meteorological basis for the *D*-region winter anomaly. He attempts to correlate the daily variation of absorption with solar activity. Although he finds no correlation, he speculates that the anomaly might be caused by forces of a terrestrial rather than extraterrestrial nature. He is unable to test his speculations because of the scarcity of upper atmospheric data at the time.

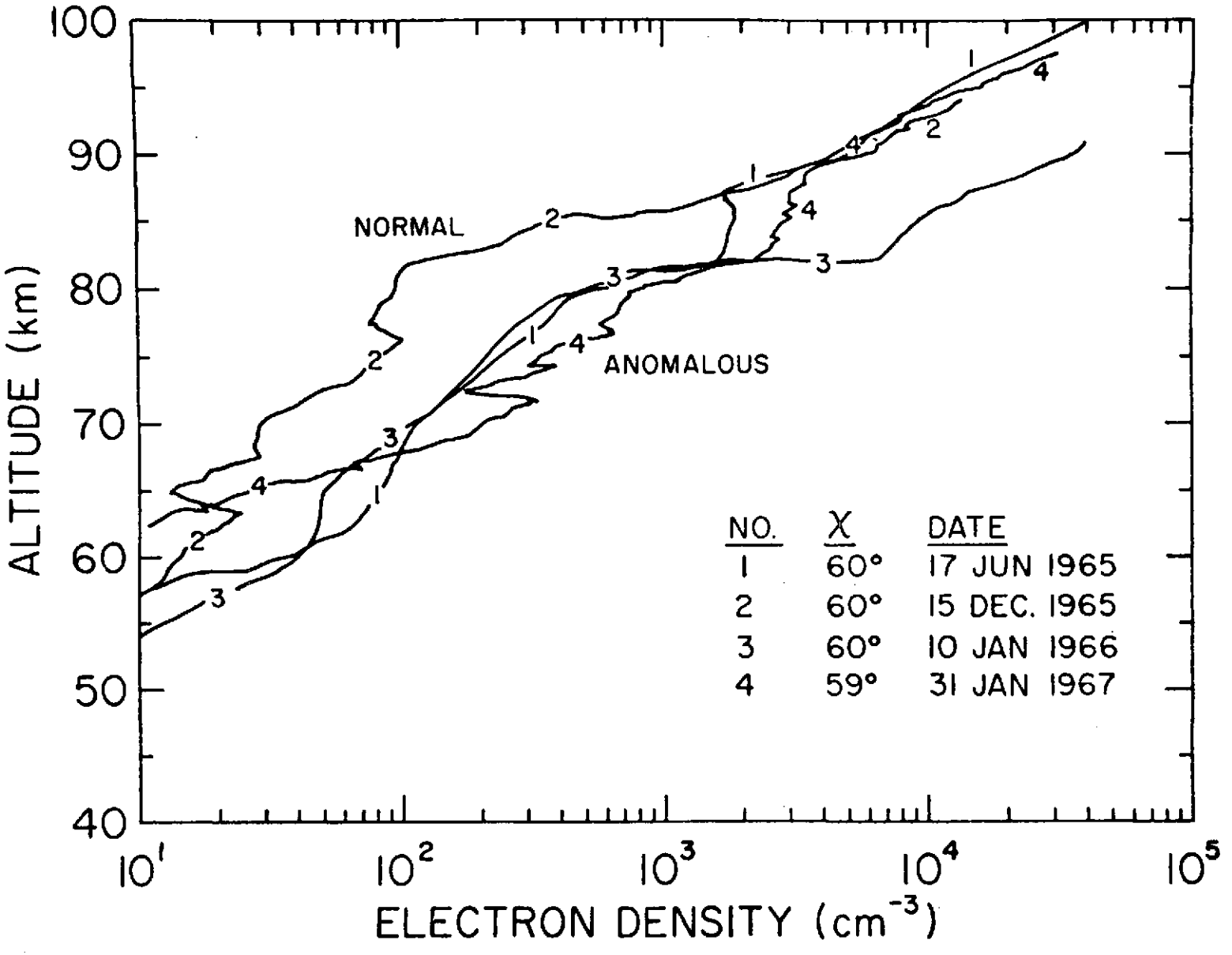

Figure 1.6 Electron-density profiles deduced at Wallops Island by rocket-borne measurements [*Sechrist, et al.*, 1969].

Bossolasco and Elena [1963] are finally able to investigate the existence of stratospheric-ionospheric coupling when a refined meteorological network operating on a global basis began. They plot the daily mean absorption values taken at Freiburg, Germany, during the winters of 1958-59 and 1960-61 against the daily variations of temperature at the 10-mb level. Figure 1.7 shows the high correlation of the data. Since the temperature and absorption patterns are separated by approximately 50 km, additional interest was incited in the meteorological basis of the anomaly.

Charney and Drazin [1961] consider the coupling of the lower atmosphere with the upper atmosphere by theoretically investigating the vertical propagation of stationary planetary waves. Planetary waves are the perturbations on a symmetric zonal circulation. These perturbations may be produced by forced disturbances which are created by continental elevations perturbing the zonal flow or may be generated spontaneously by a hydrodynamic instability. Interaction between stable atmospheric stratification and the earth's rotation gives rise to a situation enabling the propagation of these perturbations as waves to great heights. Charney and Drazin assume that the strength of the mean zonal wind is independent of latitude, and they use a β plane centered at 45° to retain variability of the Coriolis parameter. A β plane is a model of the spherical earth as a plane whose rate of rotation f (corresponding to the Coriolis parameter) varies linearly with the north-south direction. They find that the effective index of refraction for planetary waves depends primarily on the distribution of the mean zonal wind with height. Vertical energy propagation in the form of standing waves occurs in an atmosphere of uniform zonal velocity and temperature when the zonal wind velocity is eastward but less than a critical value. In all other cases, the waves are evanescent.

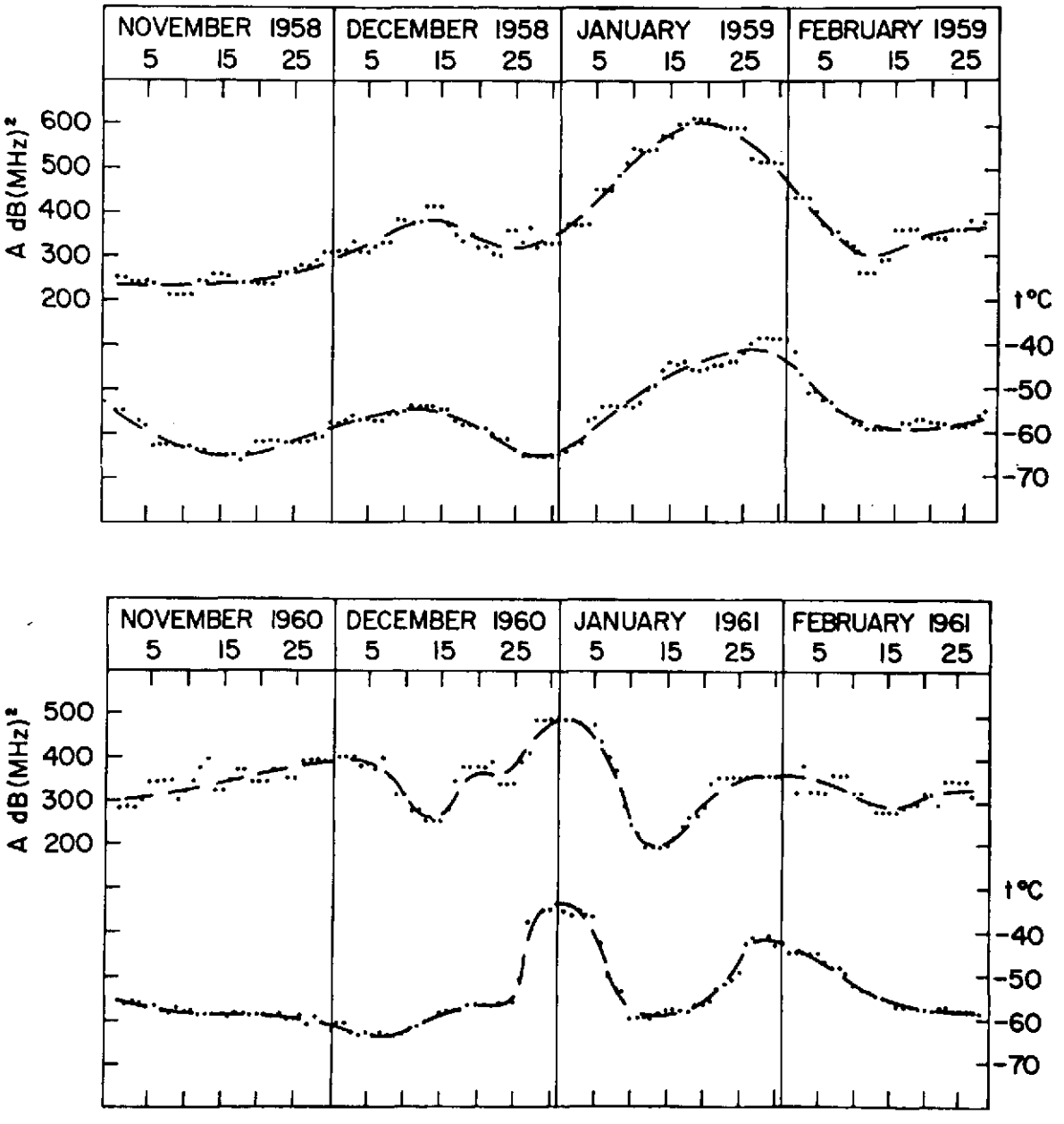

Figure 1.7 The variation of *D*-region absorption and 10 mb temperatures at Freiburg, Germany [*Bossolasco and Elena*, 1963].

Charney and Drazin [1961] conclude that stationary planetary waves at middle latitudes cannot be expected to penetrate above 20 km in the summer due to westward winds and 35 km in winter due to strong eastward winds; however, energy can escape into the *D* region near the equinoxes when the upper atmospheric zonal flow reverses. Data on the zonal wind structure of the upper stratosphere establish the essential correctness of Charney and Drazin's result concerning lack of propagation into a region of westward flow, but evidence shows that planetary wave motions do indeed occur in the upper stratosphere, apparently reaching as high as the lower thermosphere during most of the winter [*Dickinson*, 1968a].

Charney and Drazin's [1961] model indicates that when the Coriolis parameter is decreased, stationary planetary waves can propagate through stronger eastward winds. Assuming a middle-latitude value for the Coriolis parameter, they conclude that there is no propagation for zonal eastward winds exceeding 38 m/sec. However, *Dickinson* [1968a] considers the vertical propagation of planetary waves forced at a spherical lower boundary and finds six modes which propagate for eastward wind velocities greater than 38 m/sec and two modes for eastward wind velocities greater than 100 m/sec. This discrepancy of Charney and Drazin's conclusions with those of Dickinson is partially due to the fact that Dickinson's more realistic model includes the effect of a spherical earth on the Coriolis parameter. Also, on a spherical earth, significant disturbances of larger horizontal scale than the scales assumed by Charney and Drazin can occur.

A serious difficulty of *Dickinson's* [1968a] model is its prediction of excessively large upward propagating planetary waves. However, the disagreement between observations and Dickinson's theory is first of all a neglect of the latitudinal wind variations. Latitudinally variable zonal winds can confine a disturbance to limited latitudinal belts, greatly reducing the possible vertical propagation of disturbances [*Dickinson*, 1968b]. Dickinson also neglects the diabatic

damping of disturbances; *Dickinson* [1969] reveals that damping due to Newtonian cooling reduces waves propagating from the troposphere to the mesosphere by a factor of 2 in midwinter and a factor of 10 or more at the equinoxes.

Dickinson [1968b] examines the role of horizontal wind shears in guiding the upward propagation of stationary planetary wave motions around the winter hemisphere jet. He notes that actual zonal winds vary greatly with latitudes. Consequently, quantitative prediction of the upward propagation of planetary waves cannot be based only on the middle-latitude zonal winds as *Charney and Drazin* [1961] assume. For the idealized model of an atmosphere on a spherical earth in constant angular rotation, Dickinson concludes that ducts in regions of weak eastward wind enable upward propagation of waves.

Further experimental investigations concentrate on stratospheric warmings in which the temperature at the 10-mb level increases by tens of degrees for several days. *Shapley and Beynon* [1965] find a striking statistical correlation between absorption values and stratospheric temperatures during stratospheric warmings. During fourteen moderate stratospheric warmings, an increase of about 18 K in temperature at the 10-mb level is accompanied by a 25 per cent increase in the vertical-incidence absorption for a frequency of 1 MHz. They report that, on the average, the absorption and temperature reach a maximum approximately the same day; in roughly half the cases, the absorption maximum occurs on the day of the temperature maximum, but in the remainder, the times differ by two or three days either way. The possibility should be noted that when anomalous winter absorption is not accompanied by any temperature rise at the 10-mb level, there may nevertheless be a temperature rise at some greater altitude.

In a study of *D*-region electron densities during the stratospheric warming of June, 1963, at Christchurch, New Zealand, *Gregory* [1965] compares noon levels of constant electron density with radiosonde stratospheric temperature and

atmospheric thickness as shown in Figure 1.8. It is evident that a major increase in absorption, and hence in electron density, corresponds to an increase in temperature in the stratosphere at pressure levels of 20 to 30 mb. Gregory surmises that the winter anomaly is caused by a redistribution of ionizable constituents, particularly by vertical motion and possibly through turbulent transport. While the production of electrons is still due to solar radiation, the electron density is now presumed to be determined by the redistribution of ionizable constituents and negative ions due to mass transport.

The electron-density enhancement during an anomalous condition can possibly be caused by an enhancement of the nitric oxide concentration due to the effect of *D*-region warming on the equilibrium photochemistry of nitric oxide. *Sechrist* [1967] investigates this effect in the *D* region using as a basis the photochemical equilibrium theory of *Nicolet* [1965]. Assuming photochemical equilibrium conditions, the steady-state concentration of nitric oxide is calculated in the 60-90 km range using the equilibrium concentration $n^*(NO)$ of nitric oxide

$$n^*(NO) = 10^{-1} \exp(-3000/T)\, n(O_2) + 5 \times 10^{-7}\, n(O) \qquad (1.17)$$

where T is the absolute temperature in the *D* region. Electron-density profiles in the 60-90 km range are calculated assuming that nitric oxide is the only ionizable constituent. He suggests that a temperature increase produces enhancements of the nitric oxide concentration in the *D* region which in turn increase the electron density through effects of Lyman-α radiation. Thus, Sechrist attempts to demonstrate that warmings in the *D* region can produce anomalous conditions.

A possible explanation of the temperature increase in the *D* region necessary for *Sechrist's* [1967] theory is given by *Kellogg* [1961]. He suggests the

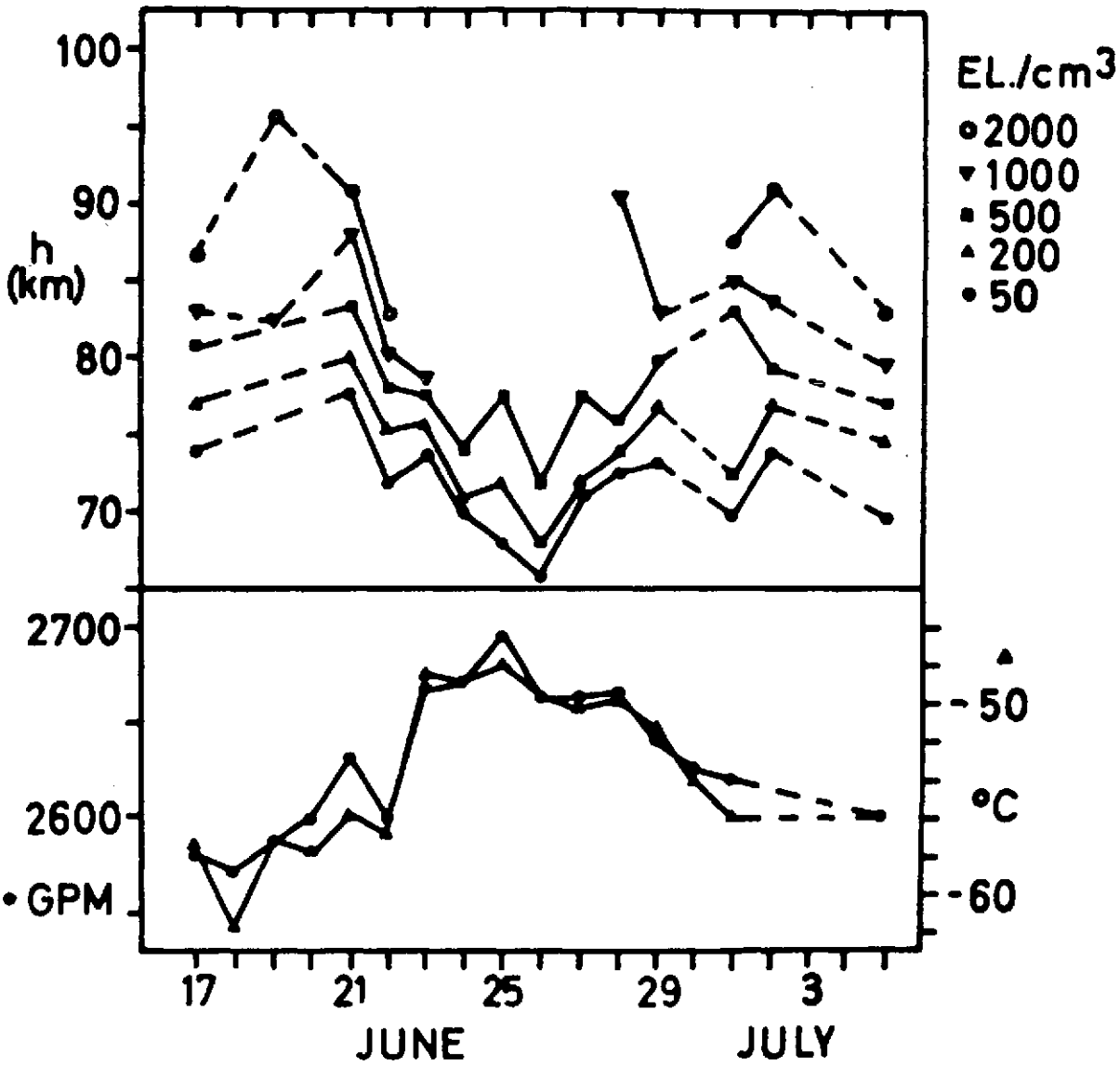

Figure 1.8 Constant noon values of electron density compared with stratospheric temperature and atmospheric thickness [*Gregory*, 1965].

large-scale subsidence of atomic oxygen as it moves northward into high latitudes. As the atomic oxygen descends into the *D* region, a reaction such as (1.18) will cause chemical heating.

$$O + O + M \rightarrow O_2 + M + 5.1 \text{ eV} \qquad (1.18)$$

Molecular oxygen which has a very large dissociation cross section in the 1300-1759 Å range (Schumann-Runge continuum) is a primary source of atomic oxygen by photodissociation at about 120 km (the height of the unit optical depth). Recombination takes place through a three-body collision, but it is a very slow process at this altitude since the density of constituents is greatly decreased. However, below 90 km three-body recombination becomes significant, thus, creating a sink for the downward diffusion of atomic oxygen.

Newell, et al. [1966] and *Newell* [1968] suggest that the winter anomaly can partially be due to large-scale motions transporting atomic oxygen into the *D* region from above. Thus, as the atomic oxygen descends, it will react with negative ions as in reactions (1.19) and (1.20) to increase the electron density.

$$O^- + O \rightarrow O_2 + e \qquad (1.19)$$

$$O_2^- + O \rightarrow O_3 + e \qquad (1.20)$$

Chapman [1969] investigates *Newell's* [1968] theory by considering the correlation between the transport of atomic oxygen and increases in ionospheric absorption. Chapman presents a postulated atomic oxygen mixing ratio gradient as illustrated in Figure 1.9. Any poleward motion between 85 and 100 km having a

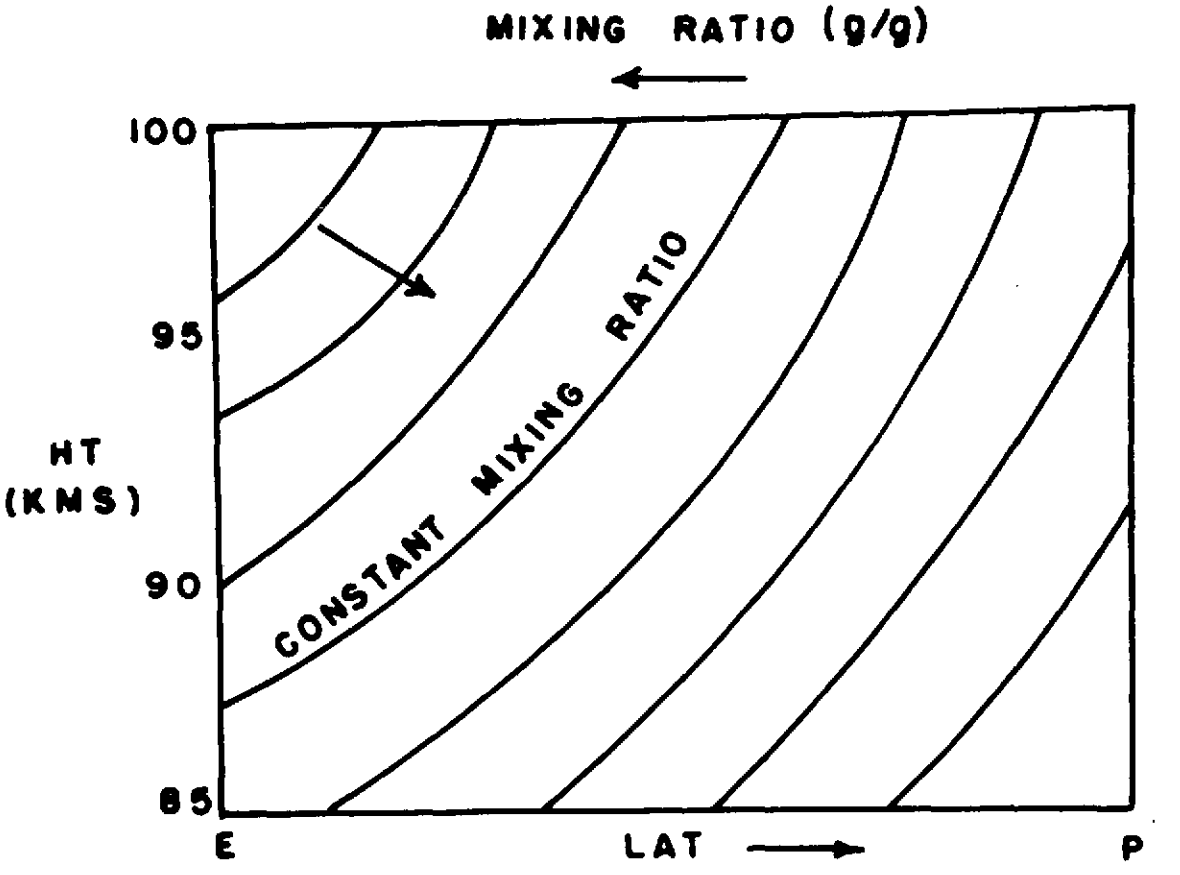

Figure 1.9 Schematic illustration of atomic oxygen mixing ratio gradient for the winter hemisphere. Arrow denotes motion down the gradient [*Chapman*, 1969].

vertical component transfers atomic oxygen down the mixing ratio gradient and results in an increase of atomic oxygen within the 85-100 km range.

During the first and fourth quarters of the year, the polar vortex and the associated pressure trough over North America are the main circulation features over the Northern Hemisphere, along with the Aleutian anticyclone. *Chapman* [1969] finds what he considers to be convincing correlations between absorption data at Washington, D.C., and the wind profiles in the upper stratosphere; thus, Chapman suggests that this pressure trough extending southwestward over North America into the lower latitudes of the Pacific Ocean is responsible for increasing the electron density in the *D* region over Washington, D.C. If the trough is present as high as 85 km and located west of Washington, an influx of air into the Washington area will be from the south where relatively cold air prevails and also where a surplus of atomic oxygen exists. The oblique motion will carry atomic oxygen down its mixing ratio gradient as it moves poleward at and above the 85 km level. This will provide an increase in atomic oxygen at the 80 to 85 km level and thus an increase in electron density due to reactions similar to (1.19) and (1.20). If the trough is located east of the Washington area at all levels, southward winds will prevail causing a decrease in the amount of atomic oxygen transported into this area.

With a scale analysis, *Geisler and Dickinson* [1968] examine the joint photochemical equations for nitric oxide and atomic nitrogen in the *D* region to demonstrate that *Sechrist's* [1967] assumption of photochemical equilibrium is not valid due to insufficient quantities of atomic nitrogen to produce a time constant short compared to transport. They, however, suggest that changes in nitric oxide can still cause the winter anomaly, but these changes in nitric oxide result from dynamic processes. Their results indicate that a vertical velocity

of the order of 0.5 cm/sec or greater, if presisting for several weeks, will produce a steady-state distribution of nitric oxide in the 70-85 km region which is nearly the same as that which would be produced by complete mixing. Planetary waves are accompanied by vertical motions of this order of magnitude. They also suggest that transient variations of the planetary wave pattern, with a time scale of a week or less, can be expected to produce variations in nitric oxide in the vicinity of the assumed upper boundary, but it is not clear whether a significant amount of nitric oxide can be transported down by such motions.

Gregory and Manson [1969b] derive seasonal electron-density profiles in the *D* region from measurements near Christchurch, New Zealand, during the period 1963-67. They notice an increase in monthly mean electron densities in the fall to early winter period. These increases occur during the establishment of the southern-winter eastward circulation from 20 to 100 km. This developing eastward system permits planetary motions to reach the *D* region. During the winter period, the mean noon electron densities from 80-88 km are constant despite the reduction of intensity of solar ionizing radiation; they suggest that this can be explained by the small value of the eastward wind velocity in this period, permitting transmission of wave energy into the *D* region.

Gregory and Manson [1970] examine in more detail the stratospheric-ionospheric associations which are evident in data for the two years 1963-64. The dates of the first obvious winter increase of ionospheric absorption, and also the largest increase during each winter, were determined by simple inspection, and the New Zealand Meteorological Service was asked to comment upon the flow conditions prevailing at upper balloon levels in each case. A common factor, namely the approach of a pressure ridge across the Tasman Sea, is easily identified in more than 80 per cent of the instances chosen.

Christie [1970] carries out an analysis largely by an analogy between ozone transport through the tropopause and NO transport through the mesopause. He points out many common features in the thermal, flow, and radiative temperature change distributions in the vicinity of the tropopause in mid-latitudes, and the winter mesopause in low latitudes. He states that NO is transferred along isentropic trajectories, while maintaining a constant mixing ratio near the mesopause, as are ozone and radioisotopes near the tropopause. Under these circumstances, it is quite plausible that NO transport can take place freely over heights of a few kilometers resulting from the intermittent passage of planetary-wave systems.

Deland and Friedman [1972] analyze the large-scale distribution of f-min, the minimum frequency at which reflection from the ionosphere is recorded from an ionosonde. This parameter is a rough indicator of ionospheric absorption in the D region. They do a statistical analysis of the relationship between the planetary-scale fluctuations of f-min and the fluctuations of stratospheric constant pressure surfaces. Their observational evidence of ionospheric planetary-scale disturbances which correlated with the fluctuations of planetary waves in the lower atmosphere is consistent with previous observations of the relation of anomalous absorption to synoptic patterns in the stratosphere and troposphere.

Maehlum [1967] suggests that precipitating energetic electrons cause the winter anomaly. He supports this theory by demonstrating that the anomaly is correlated at magnetically conjugate stations, and he further presents a correlation between precipitating electrons and ionospheric effects. Some support has also been found by *Bourne and Hewitt* [1968] and *Belrose and Thomas* [1968] in which anomalous absorption has been measured after some magnetic storms.

However, *Manson and Merry* [1970] present evidence indicating that electron precipitation is only a small contributor to the winter anomaly. Their results show that electron precipitation contributed 3 dB to the monthly mean noon absorption at 2.4 MHz compared to 15 dB absorption increases for anomalous conditions.

The enhancement of electron density during the *D*-region winter anomaly may be caused by a decrease in the electron recombination rate [*Geller and Sechrist*, 1971]. *Sechrist* [1970] suggests that changes in the electron recombination rate can be caused by variations in the water vapor concentration induced by atmospheric circulation. *Reid* [1970] suggests another mechanism for changes in the electron recombination coefficient. From *Narcisi and Bailey's* [1965] rocket measurements of positive ions, Reid speculates that large water clusters, of mass 55, 73, etc., exist which are broken up by the passage of the rocket. If the large water clusters have large recombination coefficients, it is possible that temperature increases would break up these clusters causing the electron recombination rate to decrease.

2. THEORY OF PARTIAL REFLECTIONS

2.1 *Brief Review of Magnetoionic Theory*

A magnetoionic medium is a gas consisting of a homogeneous mixture of neutral molecules and atoms, electrons, positive ions, and negative ions under the influence of an external magnetic field. Magnetoionic theory concerns radio wave propagation through this medium. The ionosphere is a magnetoionic medium which is only weakly ionized, but it is not homogeneous. However, magnetoionic theory can be applied by assuming the ionosphere is horizontally stratified into thin slabs in which the medium is homogeneous.

As a radio wave travels through the ionosphere, it sets the electrons into oscillations coherent with the electric field of the wave. The motion of positive or negative ions may be neglected because their greater mass inhibits their mobility. Due to collisions between the electrons and neutral particles, the wave loses energy, and the electron motion converts to random thermal motion. This process converts electromagnetic energy into heat.

Appleton [1927] and *Hartree* [1929] independently derived an expression for the complex refractive index given by Equation 2.1 which governs the propagation of high-frequency radio waves through a magnetoionic medium.

$$n_{o,x}^2 = 1 - \frac{X}{1 - iZ - \frac{Y_T^2}{2(1-X-iZ)} \mp \left(\frac{Y_T^4}{4(1-X-iZ)^2} + Y_L^2 \right)^{1/2}} \qquad (2.1)$$

where $X = Ne^2/\varepsilon_0 m\omega^2$

$Y = \omega_H/\omega$

$Z = \nu_{AH}/\omega$

ω = angular frequency of radio wave

ω_H = angular gyro frequency = Be/m

ν_{AH} = Appleton-Hartree electron collision frequency

Y_L = $Y \cos \phi$ = Longitudinal component of Y

Y_T = $Y \sin \phi$ = Transverse component of Y

ϕ = angle between the direction of propagation and the earth's magnetic field

e = electron charge = 1.6×10^{-19} C

m = electron mass = 9.1×10^{-31}kg

ε_0 = permittivity of free space = 8.85×10^{-12} Fm^{-1}

B = earth's magnetic field in webers/m^2

N = electron density in electrons/m^3

The subscripts o and x refer to the ordinary and extraordinary modes of propagation respectively; the positive and negative signs in the denominator are associated with the ordinary and extraordinary modes, respectively.

In deriving the Appleton-Hartree expression, it was assumed that the collision frequency ν_{AH} was independent of electron velocity; rather, they assumed the electron was subjected to a drag force. However, *Phelps and Pack* [1959] demonstrated by laboratory experiments that an electron's collision frequency is directly proportional to the kinetic energy of the electron. For propagation of a radio wave in regions where the collision frequency is small compared to the angular wave frequency, the Appleton-Hartree expression gives little error. However, in the *D* region, collisional effects become important causing the collision frequency and angular wave frequency to be the same order of magnitude.

Sen and Wyller [1960] successfully derive generalized magnetoionic equations incorporating the assumption that the collision frequency is dependent

on electron energy. They also assume that (a) the ionosphere is a weakly ionized gas, (b) the mass of the neutral molecules is much greater than the mass of the electrons, (c) electron-electron collisions are negligible compared to electron-neutral collisions, and (d) the imposed electric field is negligible compared with the thermal energy so that the electron and neutral-molecule velocity distributions are Maxwellian. The generalized form of the complex refractive index is

$$n^2_{o,x} = (A + B \sin^2\phi \pm \sqrt{B^2 \sin^4\phi - C^2 \cos^2\phi})/(D + E \sin^2\phi) \qquad (2.2)$$

where $A = 2\varepsilon_I(\varepsilon_I + \varepsilon_{III})$

$B = \varepsilon_{III}(\varepsilon_I + \varepsilon_{III}) + \varepsilon_{II}^2$

$C = 2\ \varepsilon_I\ \varepsilon_{II}$

$D = 2\ \varepsilon_I$

$E = 2\ \varepsilon_{III}$

The permittivity elements are

$$\varepsilon_I = (1-a) - ib$$

$$\varepsilon_{II} = \frac{1}{2}(f-d) + (i/2)(c-e)$$

$$\varepsilon_{III} = [\alpha - \tfrac{1}{2}(c+e)] + i[b - \tfrac{1}{2}(f+d)]$$

where $a = (\omega_0^2/\nu_m^2)\ \mathcal{G}_{3/2}(\omega/\nu_m)$

$b = (5\omega_0^2/2\omega\nu_m)\ \mathcal{G}_{5/2}(\omega/\nu_m)$

$c = (\omega_0^2(\omega-\omega_H)/\omega\nu_m^2)\ \mathcal{G}_{3/2}[(\omega-\omega_H)/\nu_m]$

$d = (5\omega_0^2/2\omega\nu_m)\ \mathcal{G}_{5/2}[(\omega-\omega_H)/\nu_m]$

$$e = [\omega_0^2(\omega+\omega_H)/\omega\nu_m^2] \; \mathcal{G}_{3/2}[(\omega+\omega_H)/\nu_m]$$

$$f = (5\omega_0^2/2\omega\nu_m) \; \mathcal{G}_{5/2}[(\omega+\omega_H)/\nu_m]$$

The following quantities need to be defined.

ω_0^2 = angular plasma frequency = $Ne^2/m\varepsilon_0$

ν_m = monoenergetic collision frequency

$$\mathcal{G}_p(x) = \frac{1}{p!}\int_0^\infty \frac{\varepsilon^p}{\varepsilon^2+x^2} e^{-\varepsilon} \, d\varepsilon$$

$\varepsilon = mv^2/2kT$

v = electron velocity

k = Boltzmann constant = 1.38×10^{-23} JK^{-1}

T = absolute temperature

The above generalized expression for the refractive index can be simplified by using the quasi-longitudinal approximation in which the angle between the direction of propagation and the earth's magnetic field is assumed to be zero. *Pirmat and Bowhill* [1968] demonstrate that this assumption can be made at Urbana, Illinois. With $\phi = 0$, the refractive index reduces to

$$n_{o,x}^2 = (A \pm \sqrt{-C^2 \cos^2\phi})/D$$

$$= 1 - [\omega_0^2(\omega\pm\omega_H)/\omega\nu_m^2] \; \mathcal{G}_{3/2}[(\omega\pm\omega_H)/\nu_m] \qquad (2.3)$$

$$-i(5\omega_0^2/2\omega\nu_m) \; \mathcal{G}_{5/2}[(\omega\pm\omega_H)/\nu_m]$$

2.2 *Development of Partial-Reflection Equations*

The amplitude $A_{o,x}$ of a radio wave partially reflected from the *D* region is dependent on the reflection coefficient $R_{o,x}$ of the scatterer and the absorption in the region below the scatterer. Thus, if the radio wave is reflected

from a scatterer at height h,

$$A_{o,x} = R_{o,x} \exp\left[-2 \int_0^h K_{o,x} dh\right] \tag{2.4}$$

[*Belrose and Burke*, 1964] where $K_{o,x}$ is the absorption coefficient and determined as follows.

By definition, $n_{o,x} = \mu_{o,x} - iX_{o,x}$

where $X_{o,x} = c\, K_{o,x}/\omega$

$X_{o,x}$ = absorption index

$\mu_{o,x}$ = phase refractive index

$n_{o,x}^2 = (\mu_{o,x} - iX_{o,x})^2 = \mu_{o,x}^2 - X_{o,x}^2 - i2\mu_{o,x} X_{o,x}$.

Equating the imaginary parts of the above equation with equation (2.3) and assuming $\mu \cong 1$, an expression for $K_{o,x}$ can be derived

$$K_{o,x} = (5Ne^2/4m\epsilon_0 c\nu_m) \; \mathcal{L}_{5/2}[(\omega \pm \omega_H)/\nu_m] \tag{2.5}$$

where c is the velocity of light.

Using equation (2.4), the ratio of the received amplitudes of the two magnetoionic modes is

$$A_x/A_o = (R_x/R_o) \exp\left[-2 \int_0^h (K_x - K_o) dh\right] \tag{2.6}$$

If Fresnel reflection is assumed, the reflection coefficient is approximately given by

$$R = \frac{n_2 - n_1}{n_2 + n_1} \tag{2.7}$$

where the refractive index changes from n_1 to n_2 at the boundary in Figure 2.1 [*Budden*, 1961]. If the change in the refractive index at the boundary is small, then equation (2.7) reduces approximately to

$$R \cong \frac{\delta n}{2n} \quad . \tag{2.8}$$

The ratio of the ordinary and extraordinary refraction coefficient is given by

$$\frac{R_x}{R_o} = \frac{\delta n_x}{2n_x} \; \frac{2n_o}{\delta n_o} \tag{2.9}$$

Assuming ν_m is constant across the boundary [*Belrose and Burke*, 1964], n is a function of N alone, i.e., the partial reflections are due solely to irregularities in electron density. Equation (2.3) can be differentiated with respect to N to give

$$2n \frac{\delta n}{\delta N} = -(e^2/\varepsilon_0 m \nu_m \omega) \left\{ [(\omega \mp \omega_H)/\nu_m] \; \mathcal{C}_{3/2}[(\omega \mp \omega_H)/\nu_m] \right.$$
$$\left. + i(5/2) \; \mathcal{C}_{5/2}[(\omega \mp \omega_H)/\nu_m] \right\} \tag{2.10}$$

The refractive indices for the two modes will be near unity because of the low electron density in the D region. By using this fact and substituting equation (2.10) into equation (2.9), this gives

$$\frac{R_x}{R_o} = \frac{[(\omega - \omega_H)/\nu_m] \; \mathcal{C}_{3/2}[(\omega - \omega_H)/\nu_m] + i(5/2) \; \mathcal{C}_{5/2}[(\omega - \omega_H)/\nu_m]}{[(\omega + \omega_H)/\nu_m] \; \mathcal{C}_{3/2}[(\omega + \omega_H)/\nu_m] + i(5/2) \; \mathcal{C}_{5/2}[(\omega + \omega_H)/\nu_m]} \tag{2.11}$$

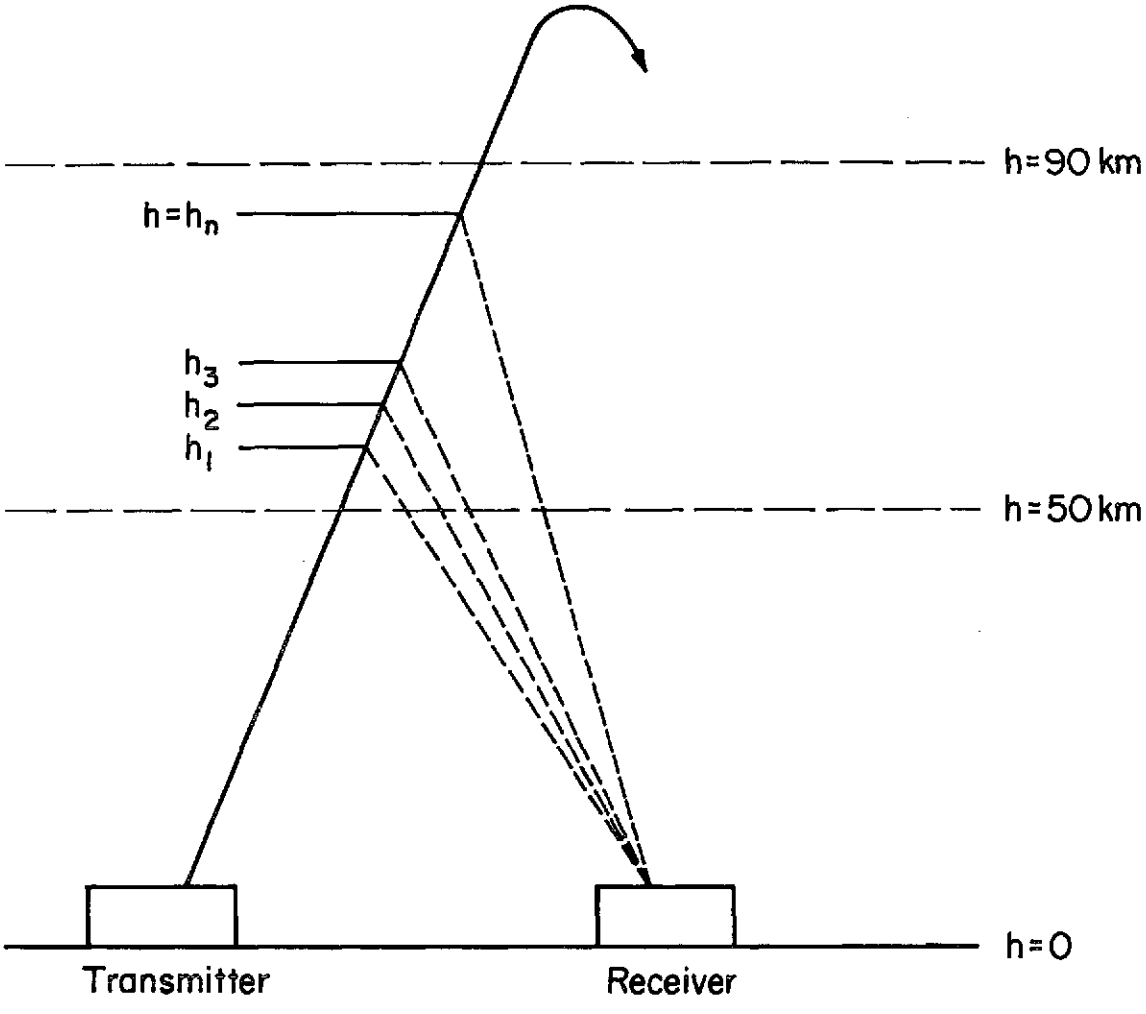

Figure 2.1 The partial-reflection model.

The magnitude of R_x/R_o is

$$\left|\frac{R_x}{R_o}\right| = \left[\frac{\left\{[(\omega-\omega_H)/\nu_m]\ \mathcal{L}_{3/2}[(\omega-\omega_H)/\nu_m]\right\}^2 + \left\{(5/2)\ \mathcal{L}_{5/2}[(\omega-\omega_H)/\nu_m]\right\}^2}{\left\{[(\omega+\omega_H)/\nu_m]\ \mathcal{L}_{3/2}[(\omega+\omega_H)/\nu_m]\right\}^2 + \left\{(5/2)\ \mathcal{L}_{5/2}[(\omega+\omega_H)/\nu_m]\right\}^2}\right]^{1/2}$$

The ratio of the reflection coefficients is a function of the operating angular frequency ω, the angular gyrofrequency ω_H, and the electron collision frequency ν_m.

The ratio of equation (2.6) evaluated at two heights, $h_1 < h_2$, is

$$\frac{(A_x/A_o)_{h=h_1}}{(A_x/A_o)_{h=h_2}} = \frac{(R_x/R_o)_{h=h_1}}{(R_x/R_o)_{h=h_2}} \exp\left[2\int_{h_1}^{h_2}(K_x-K_o)\,dh\right] \tag{2.12}$$

By choosing an interval $\Delta h = h_2-h_1$ that is small enough for the differential absorption (K_x-K_o) to be assumed constant, then $2\int_{h_1}^{h_2}(K_x-K_o)\,dh \cong 2(K_x-K_o)\Delta h$. Equation 2.12 can be solved for the differential absorption term to give

$$K_x-K_o = \frac{1}{2\Delta h}\ln\left\{[(A_x/A_o)/(R_x/R_o)]_{h_1}/[(A_x/A_o)/(R_x/R_o)]_{h_2}\right\} \tag{2.13}$$

The electron density N can be determined by combining equations (2.5) and (2.13)

$$N = \left[(5\Delta h e^2/2cme_0\nu_m)\ \left\{\mathcal{L}_{5/2}[(\omega-\omega_H)/\nu_m] - \mathcal{L}_{5/2}[(\omega+\omega_H)/\nu_m]\right\}\right]^{-1}$$
$$\times\left[\ln\left\{[(A_x/A_o)/(R_x/R_o)]_{h_1}/[(A_x/A_o)/(R_x/R_o)]_{h_2}\right\}\right] \tag{2.14}$$

The electron density is dependent on known quantities except for the electron collision frequency and received amplitude. Thus, if the electron collision frequency is either known or assumed, a measurement of the received amplitude ratio A_x/A_o as a function of height provides enough information to calculate the electron-density profile.

2.3 *Discussion of Assumptions and Limitations*

Several assumptions are made in the development of the partial-reflection theory. In arriving at equation (2.11), it is assumed that the refractive index for both modes of propagation does not differ greatly from unity. This assumption is certainly invalid at the height of total reflection because the electron density and wave frequency are such that the real part of the refractive index is near zero. However, at *D*-region altitudes, this is not the case because of the low values of electron density; therefore, by choosing an appropriate wave frequency, this assumption is justified.

It is assumed that the observed heights of the partial reflections are the true heights. This is not the case in the presence of off-vertical echoes. The problem of off-vertical echoes has plagued the partial-reflection experiment since Gardner and Pawsey's observations; it limits the height range of useful data because reflections from off-vertical irregularities will be recorded as coming from a higher altitude, and thus lead to a wrong value of A_x/A_o. *Belrose* [1970] points out that the construction of large high-gain antenna arrays seems to be the only way to overcome this problem. At Urbana, two large 60-dipole circularly polarized antennas, each covering about 20 acres, are used for transmission and reception to alleviate the problem.

Due to the weakness of the partial reflections, noise is often a limiting factor in partial-reflection measurements. This problem becomes more evident around dawn and dusk because of the increased background noise. Employing a high power transmitter and large gain antennas improves the signal-to-noise ratio. Also, a noise-defeating algorithm is used to eliminate much of the data contaminated by noise; this algorithm will be discussed later.

Minima in partial-reflection electron-density profiles between 75 and 85 km must be interpreted carefully. These minima are observed at Urbana, and similar

results are presented by *Belrose and Burke* [1964], but they are usually not observed in electron-density profiles determined by rocket measurements [*Mechtly, et al.*, 1972]. From measurements at Urbana, it was verified that the minima in electron density are related to a sharp increase in the backscattering cross section per unit volume at the same heights [*Edwards*, 1971]. Under such conditions, the minima cannot be considered real because measurements made close to a maximum in scattering cross section will be biased by strong reflections produced from the height where the scattering cross section is a maximum.

A necessary assumption is that of a collision-frequency profile. The collision-frequency profiles used are based on rocket measurements presented by *Lodato and Mechtly* [1971]. When the best data from electron-drift-velocity-tube measurements of cross sections for momentum transfer in molecular nitrogen and in molecular oxygen are used, they conclude that the electron collision frequency is given by

$$\nu_m = 9.97 \times 10^{-18} [N_2] T + [O_2] (2.61T + 121T^{1/2}) \times 10^{-18} \quad (2.15)$$

where $[N_2]$ and $[O_2]$ are the concentrations (m^{-3}), and T is the absolute temperature of both the electron gas and the neutral molecular gas [*Lodato and Mechtly*, 1971]. For *D*-region conditions, this result can be approximated by a constant times the neutral atmospheric pressure p

$$\nu_m = k\, p \quad (2.16)$$

where $k = 7.3 \pm 0.1 \times 10^5\ N^{-1}m^2s^{-1}$ and p is in Nm^{-2}. This result is used with the CIRA (1965) model pressure profile to obtain a collision-frequency profile. Seasonal variations in the collision frequency are taken into

consideration using the USSAS (1966) model atmosphere; three different profiles are used for summer, winter, and equinox.

It is very difficult to place firm numbers on the uncertainty in electron densities measured by the partial-reflection technique. However, *Belrose* [1970] points out that after considering errors in great detail, the electron density can be determined with an accuracy comparable or exceeding that deduced by other ground-based techniques.

3. SYSTEM DESCRIPTION

In the partial-reflection experiment, radio frequency pulses of ordinary and extraordinary circular polarization are transmitted into the ionosphere. Over a given distance, the extraordinary mode suffers an absorption which is greater than the absorption suffered by the ordinary mode. This difference in absorbed energy between the extraordinary and the ordinary mode of circular polarization is termed differential absorption. From the theory of Section 2.1, it is apparent that the electron density is proportional to the differential absorption of the radio wave.

The differential absorption is indirectly determined by measuring the ordinary and extraordinary wave amplitudes partially reflected from the *D* region. The received signals are very weak and this necessitates the use of a sensitive receiver, high-gain transmitting and receiving antennas, and a high-power transmitter. The equipment used at the Urbana installation will be described in Section 3.1 with a brief description of the collection and processing programs following. A block diagram of the system is shown in Figure 3.1.

3.1 *Equipment Description*

Pulser. The pulser controls the timing sequence of the various components of the system. Initially, the transmitting antenna is phased for transmission of the ordinary mode of circular polarization; energy supplied by the transmitter to the antenna will be radiated vertically in this mode. At t=0, the pulser sends a 10 μs pulse to the transmitter; the transmitter responds by feeding the transmitting antenna array with a radio frequency pulse. Several milliseconds later, a polarization control is activated which changes the transmitting-antenna phase from ordinary to extraordinary polarization. At

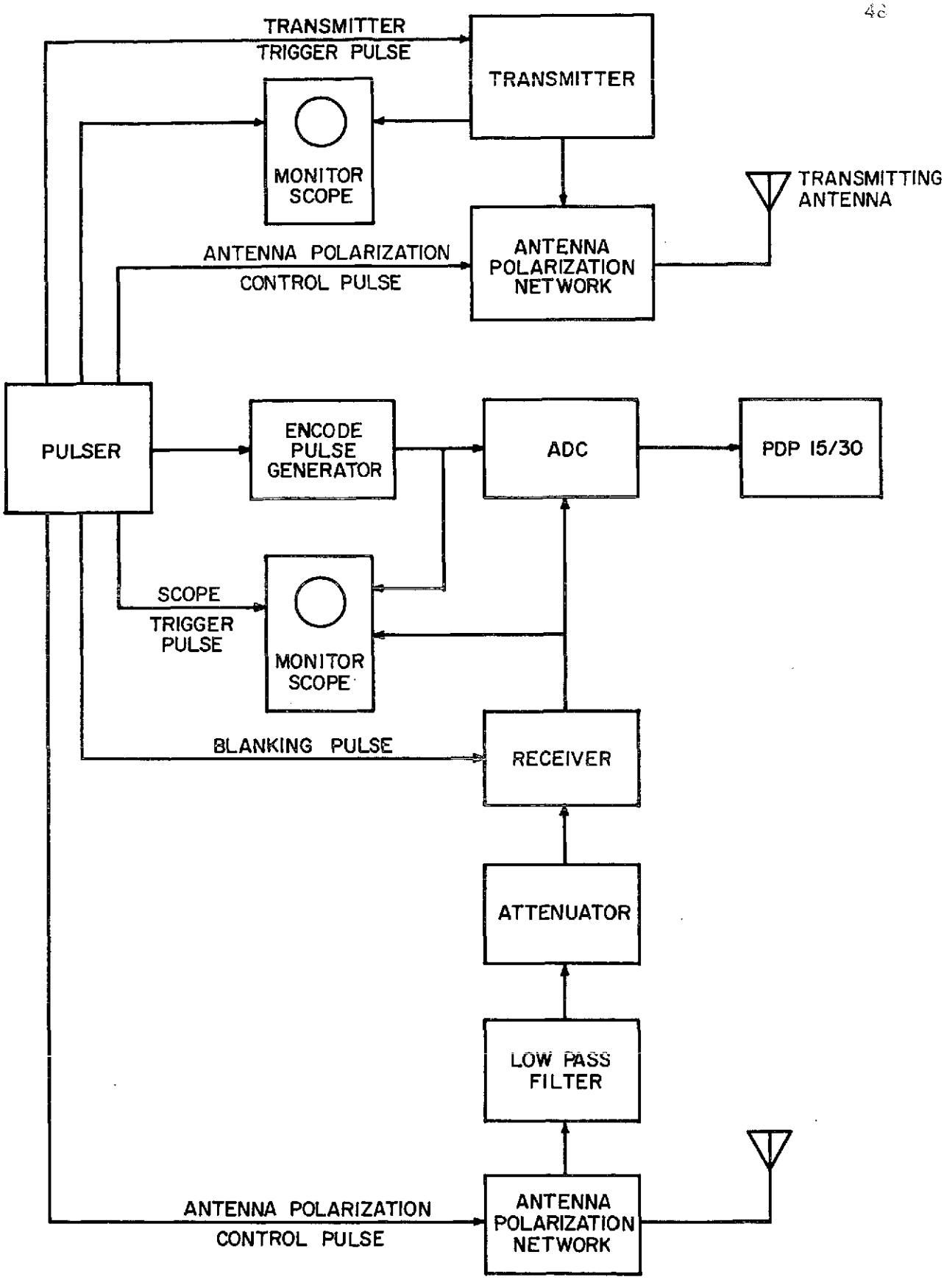

Figure 3.1 Block diagram of partial-reflection system.

t=33 ms, a second 10 μs pulse is sent to the transmitter from the pulser causing the transmission of the extraordinary pulse. The cycle is repeated at t=400 ms, giving a pulse repetition rate of 2.5 double pulses every second.

The receiving antenna system must be phased for reception of the ordinary and extraordinary modes after being partially reflected. The pulser controls this phasing as it is controlling the transmitting-antenna phase.

Transmitter. The transmitter operates at a frequency of 2.66 MHz with a peak power of 40 kW. The pulse width is 20 μs at the half-amplitude points. The unbalanced output impedance is 50 ohms, and all units of the transmitter are shielded. A detailed description of the transmitter design is given by *Henry* [1966]. An oscilloscope is used to monitor the transmitter pulse.

Receiver. Two receivers were used in the partial-reflection system. The data collected from December to about June 15 were collected by one receiver while the data after June 15 were collected by a new receiver with a redesigned detector circuit to make the input versus output characteristic linear.

The original receiver is a solid-state, superheterodyne design. It is divided into three modules: RF amplifier, IF amplifier/DC amplifier, and power supply. The receiver specifications are

Center Frequency	--	2.66 MHz
Noise Factor	--	15 dB maximum
Bandwidth	--	40 kHz at -3 dB points of bandpass response curve
Recovery Time	--	200 μs for receiver to drop into noise after 0.1 volts rms at the signal frequency applied is removed

Power Supply	--	External to RF portions of reciever, all voltages to the receiver are regulated to within 0.1% for AC line voltage variations of 10% and over the temperatures of 15°C to 35°C
RF Input Impedance	--	50 Ω, unbalanced
Output Impedance	--	10,000 Ω, unbalanced
Output Response	--	DC to 50 kHz, 1.5 volts maximum with capability of selecting either positive or negative-polarity output
Power Gain	--	Approximately 90 dB.

The RF amplifier module contains the RF amplifier, mixer, and local oscillator circuits as well as a blanking pulse generator. The blanking pulse shorts out the RF input to the receiver during the transmitter pulse. This protects the RF amplifier transistor and also prevents the receiver from saturating completely, a condition requiring approximately 200 μs from which to recover.

An oscilloscope is used to monitor the partial reflections at the receiver output.

At the input of the receiver is a manually-switched attenuator to attenuate signals that would otherwise saturate the receiver. A low-pass filter and a high-pass filter with cutoff frequencies of 3.1 MHz and 1.9 MHz, respectively, are also located at the input of the receiver to help eliminate interference from radio broadcast stations.

The new linearized receiver was designed because of the nonlinear response of the original receiver's detector circuit. The effect of this shortcoming in the original receiver is compensated by using a linearizing

subroutine in the data-processing system. However, it would be more desirable to have a receiver with a linear response.

The design and construction of the new receiver was done by G. W. Henry. The new receiver employs a detector circuit with a high-impedance constant current source devised by *Matheson* [1971]. When the detector operates at its design center frequency of 455 kHz, the detector output is linear from 10 mV to 10 V. From 10 μV to 10 mV, the output deviates by a maximum of 0.1 dB from linearity for an input change of 1 dB. However, when the detector was tested at center frequencies of 2.66 MHz or 5.00 MHz, the linear range decreases to about 33 dB; therefore, it was decided to use the Matheson circuit at its design frequency and convert the previous IF frequency of 5 MHz, down to 455 kHz.

A schematic of the Matheson detector and the modified IF amplifier module are shown in Figure 3.2. A new power supply module was designed, because the new IF amplifier created a need for different power supply voltages than were previously used. A schematic of the modified power supply is shown in Figure 3.3.

The linearized receiver operates at a center frequency of 2.66 MHz, a bandwidth of 37 kHz, a noise factor of 3.5 dB, and a gain of about 88 dB. The input versus output characteristic of the original receiver and the new receiver is shown in Figure 3.4; the improvement is apparent. The bandpass characteristic of the linearized receiver is shown in Figure 3.5. The symmetry of the pass-band is indicative of a very stable design. The response at 2.500 MHz is the second harmonic of the signal generator leaking through to the IF amplifier.

The RF module of the new receiver is basically the same except for an RF amplifier modification in the first stage biasing circuit; it was changed to a "two battery" system with a large amount of series emitter resistance to reduce

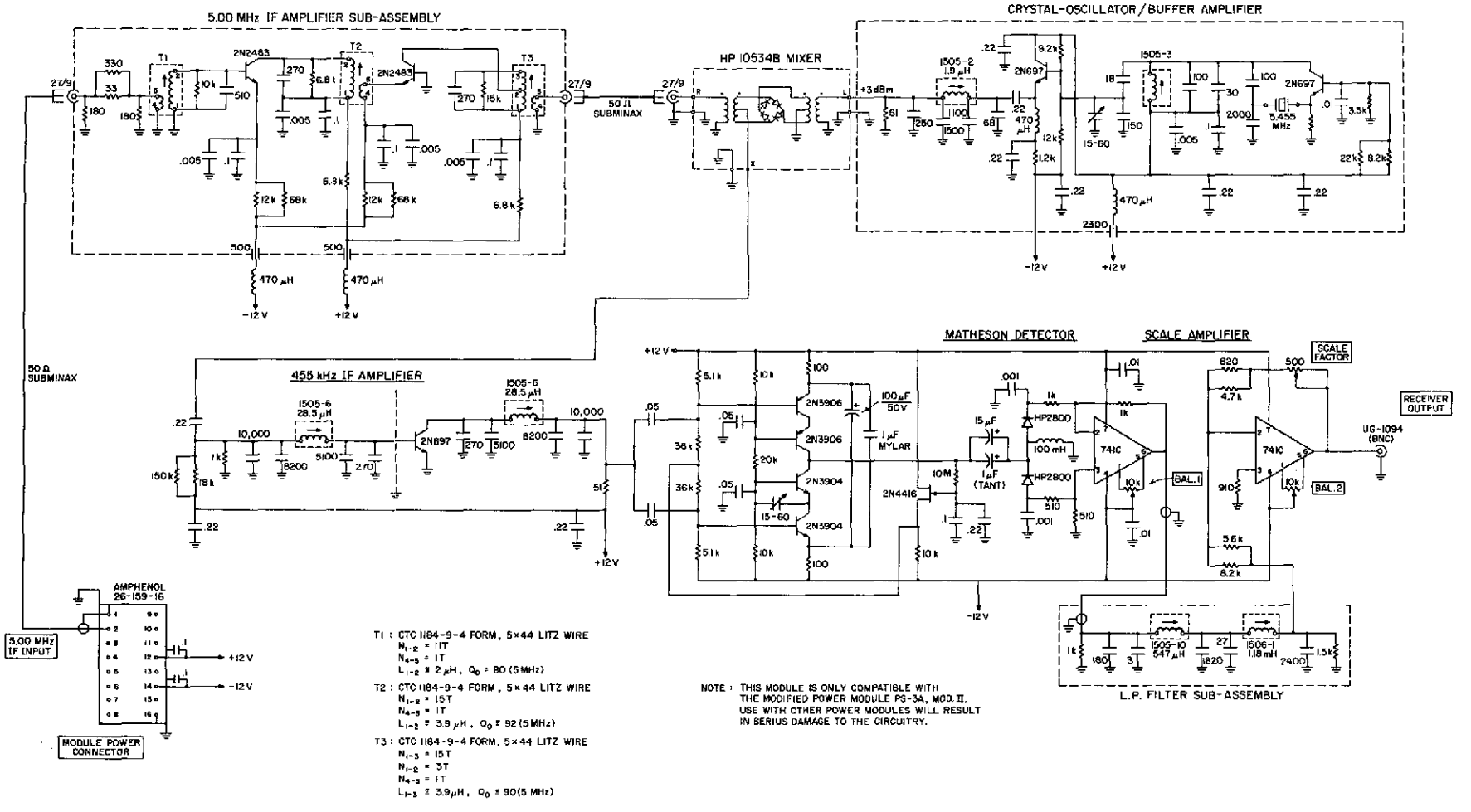

Figure 3.2 Schematic diagram of IF-7 module.

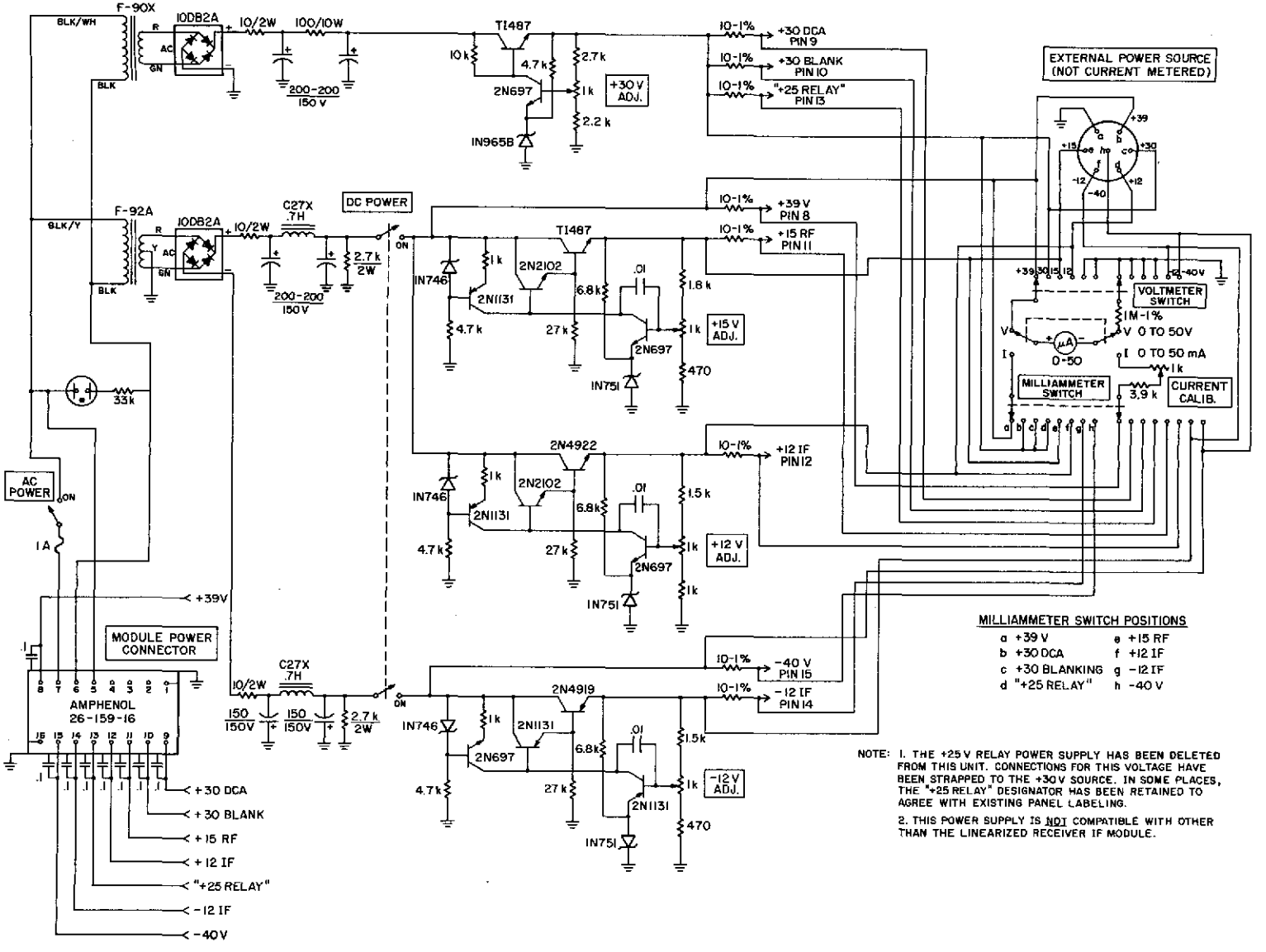

Figure 3.3 Schematic diagram of PS-3A MOD II module.

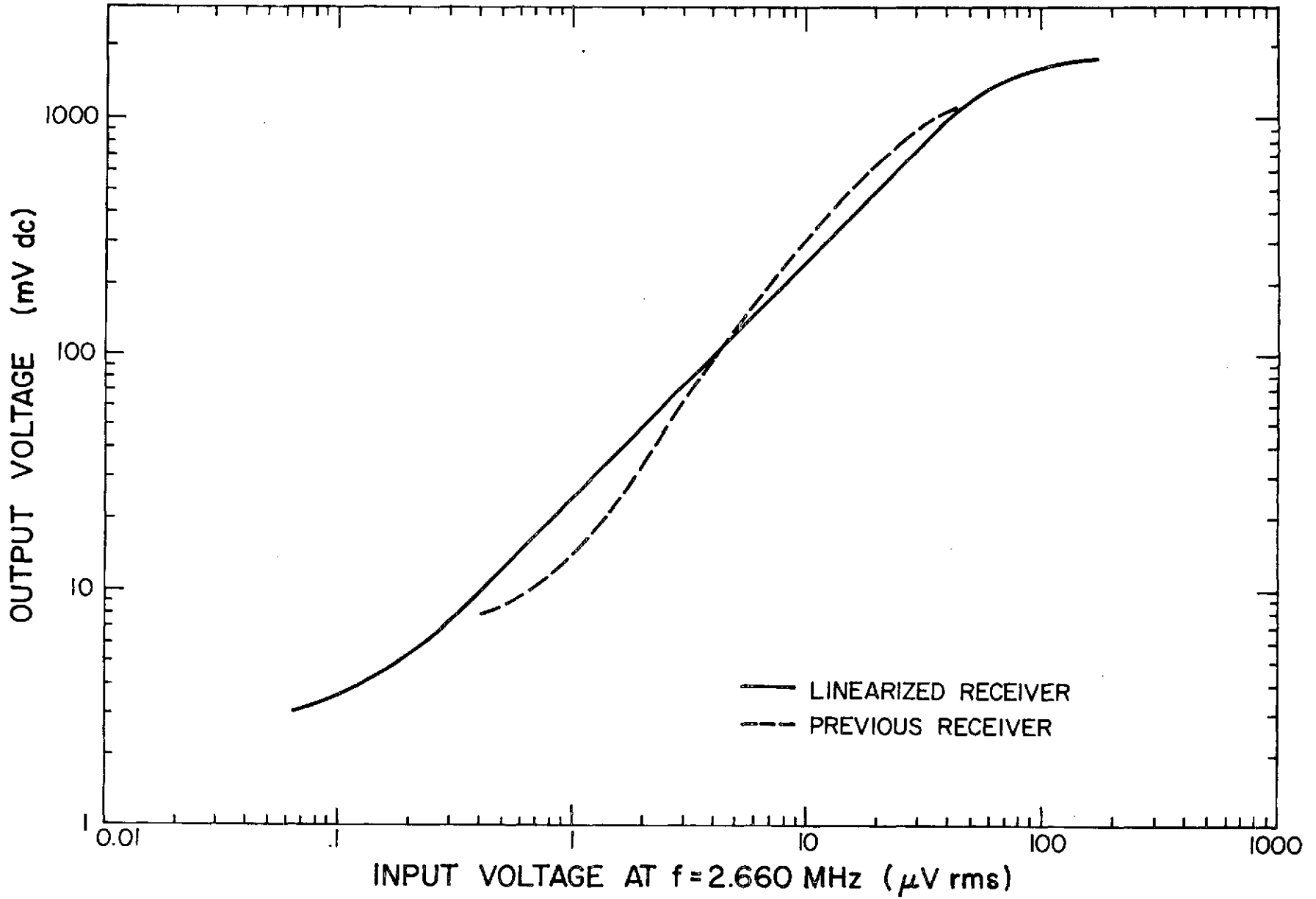

Figure 3.4 Input versus output response of receiver.

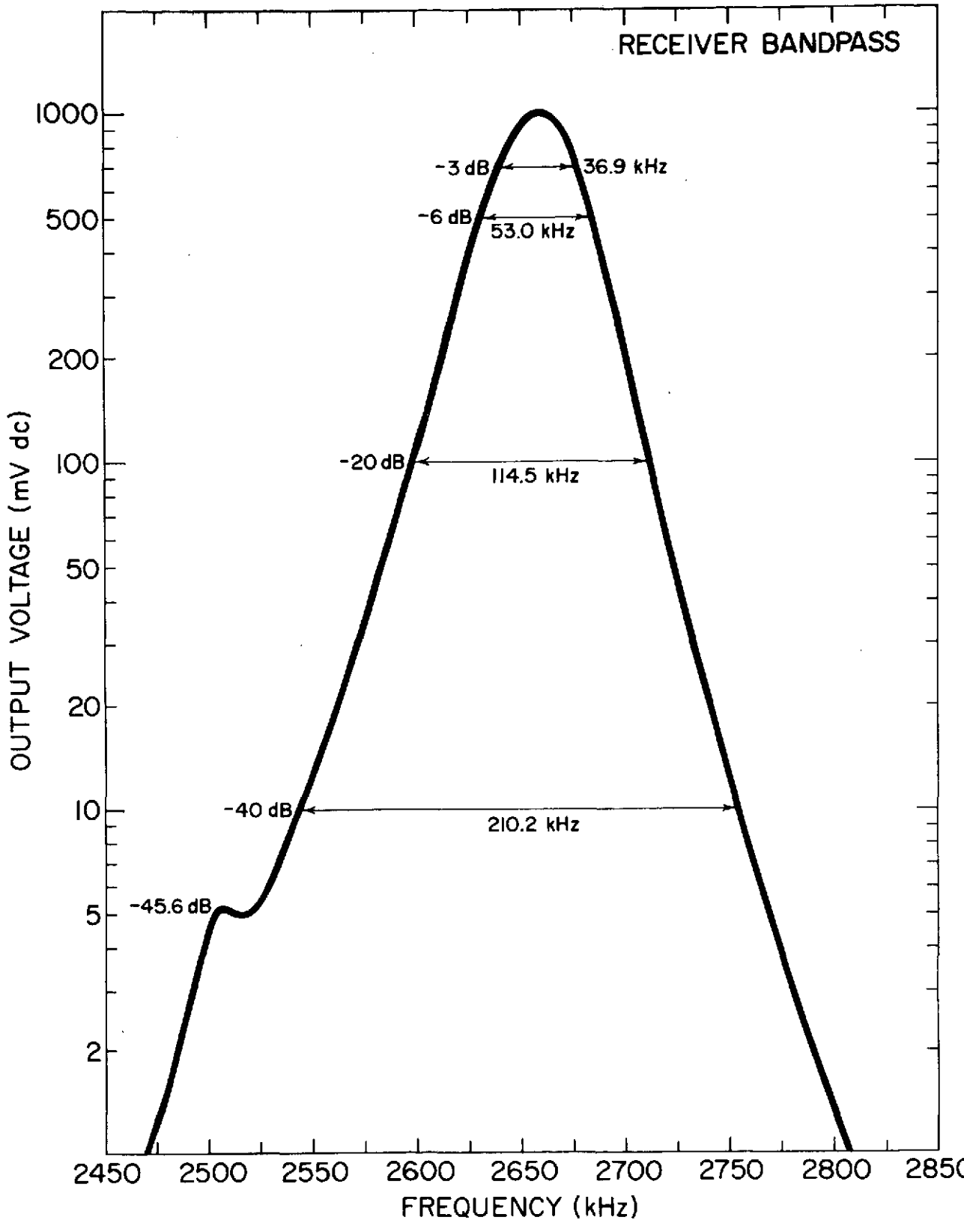

Figure 3.5 Bandpass characteristics of receiver.

the gain variation with temperature. The blanking pulse was also changed because it affected the new receiver gain; shortening the blanking pulse eliminated the problem.

Antenna Systems. Two 60-dipole antenna arrays, one for transmission and one for reception, are used in the partial-reflection experiment. Each array consists of two 30-dipole sub-arrays which are perpendicular to each other. The gain is directed vertically with a calculated 3 dB beam width of 14°.

In order to transmit a circularly polarized wave, the phasing system of Figure 3.6 is used; the two sub-arrays are denoted by "Antenna #1" and "Antenna #2". A 90° phase shift between the sub-arrays is introduced as shown. Each sub-array must be fed with an equal amount of power, or the transmitted wave will be elliptically polarized; this is done by the power divider and attenuators of Figure 3.6. The matching networks of Figure 3.6 are used for impedance transformation from the 50-ohm feedline to the 600-ohm antenna line. A polarization reversal control is used to introduce a 180° phase shift which is needed for switching between ordinary and extraordinary modes.

A block diagram of the receiving-antenna phasing system is shown in Figure 3.7. The matching networks, phase shifters, and attenuators perform the same function as in the transmitting-antenna phasing system. The received signals from each sub-array are summed to provide the receiver input.

Analog-to-Digital Converter and Computer. An HP 5610A analog-to-digital converter (ADC) digitizes the receiver output at a sampling rate of 100 kHz, allowing a height resolution of 1.5 km. It has a voltage resolution of 9 bits for an input voltage range from 0 to 1 volt. An encode pulse generator, which is triggered by the pulser, gates the analog-to-digital converter such that it digitizes the signal from 45 to 90 km in steps of 1.5 km.

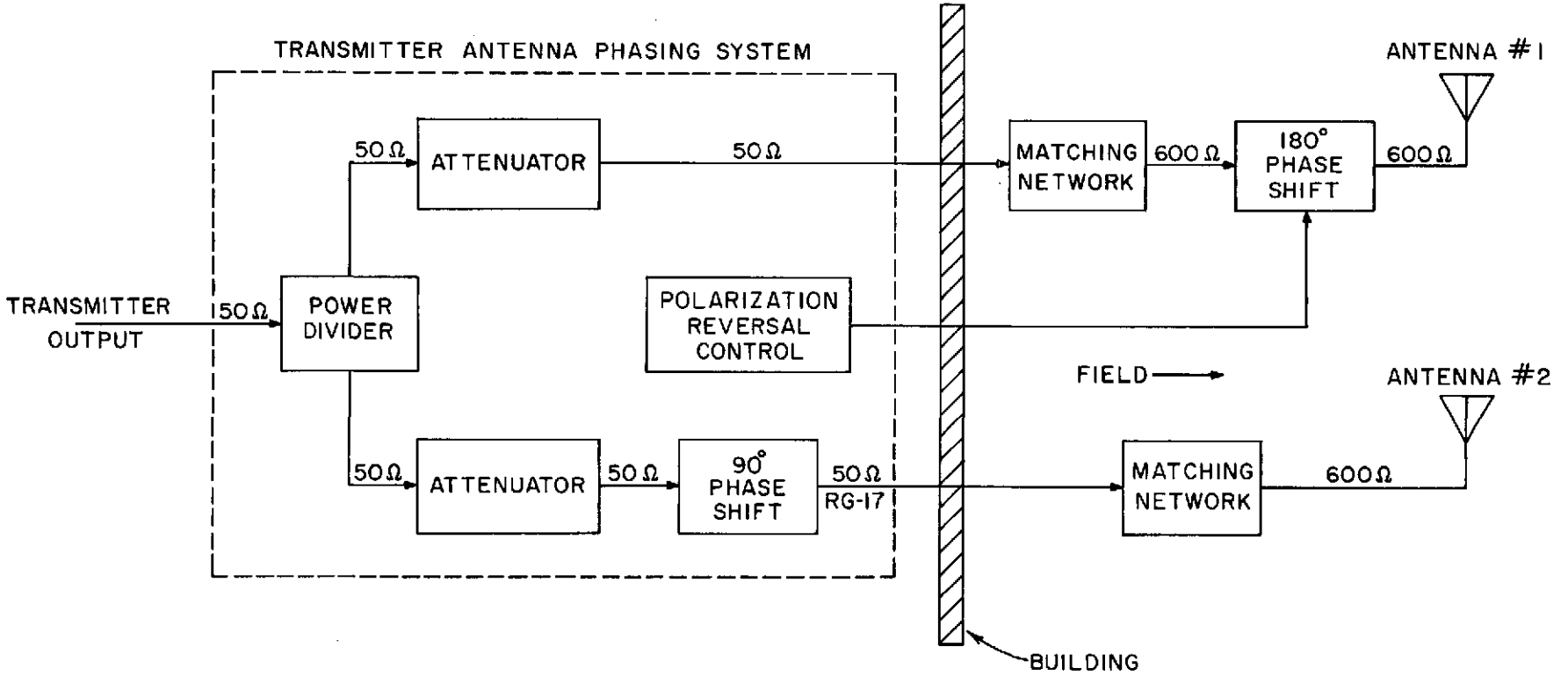

Figure 3.6 Block diagram of the transmitter antenna phasing system.

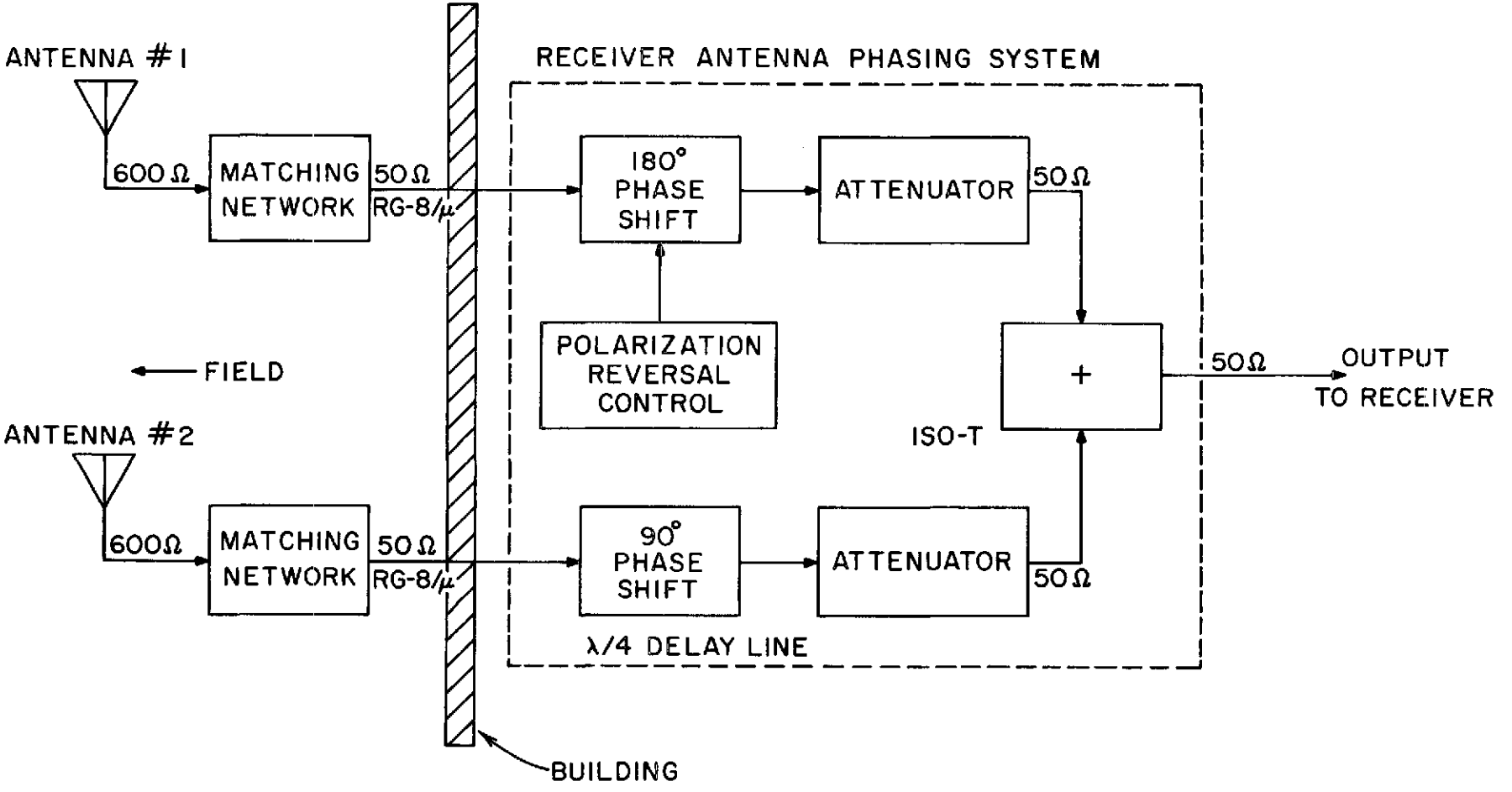

Figure 3.7 Block diagram of the receiver antenna phasing system.

A Digital Equipment Corporation PDP-15/30 computer is used to collect and process the data. It has 32 K words of core memory with each word 18 bits in length. The processing and collection programs are discussed in the next section.

3.2 *Software Description*

A flow diagram of the processing and collection programs is shown in Figure 3.8. Following is a brief description of these programs; a complete description of them is presented by *Birley and Sechrist* [1971] and *Bean and Bowhill* [1973].

The programs are initiated through the MACRO routine INTIM which reads the time given by the operator when the partial-reflection experiment begins. Control is then passed to CONTL which is the controlling program. CONTL reads introductory information supplied by the operator (e.g., the date) and initiates execution of the calibration programs: RADC, TBFORL, TTM, and LINAP.

The calibration programs determine an input versus output characteristic between the input of the receiver and the output of the ADC. This characteristic is used to alleviate any errors introduced by nonlinearities in the receiver or ADC. RADC reads the numbers from the ADC output and puts them in an array. TBFORL and LINAP calculate a straight-line-segment approximation for the input versus output characteristic. TTM stores the characteristic as a linearization table for later use during data collection.

After calibration, CONTL passes control to DLOGF which simultaneously initiates data collection through BEGIN and data processing through PROC.

BEGIN represents several subroutines that collect the partial-reflection data by sampling the receiver output. The received ordinary A-scan waveform is sampled in the range 45 to 90 km; 5 noise samples are taken at heights of 45 to 51 km, at which no signal is expected to be present, and 21 signal

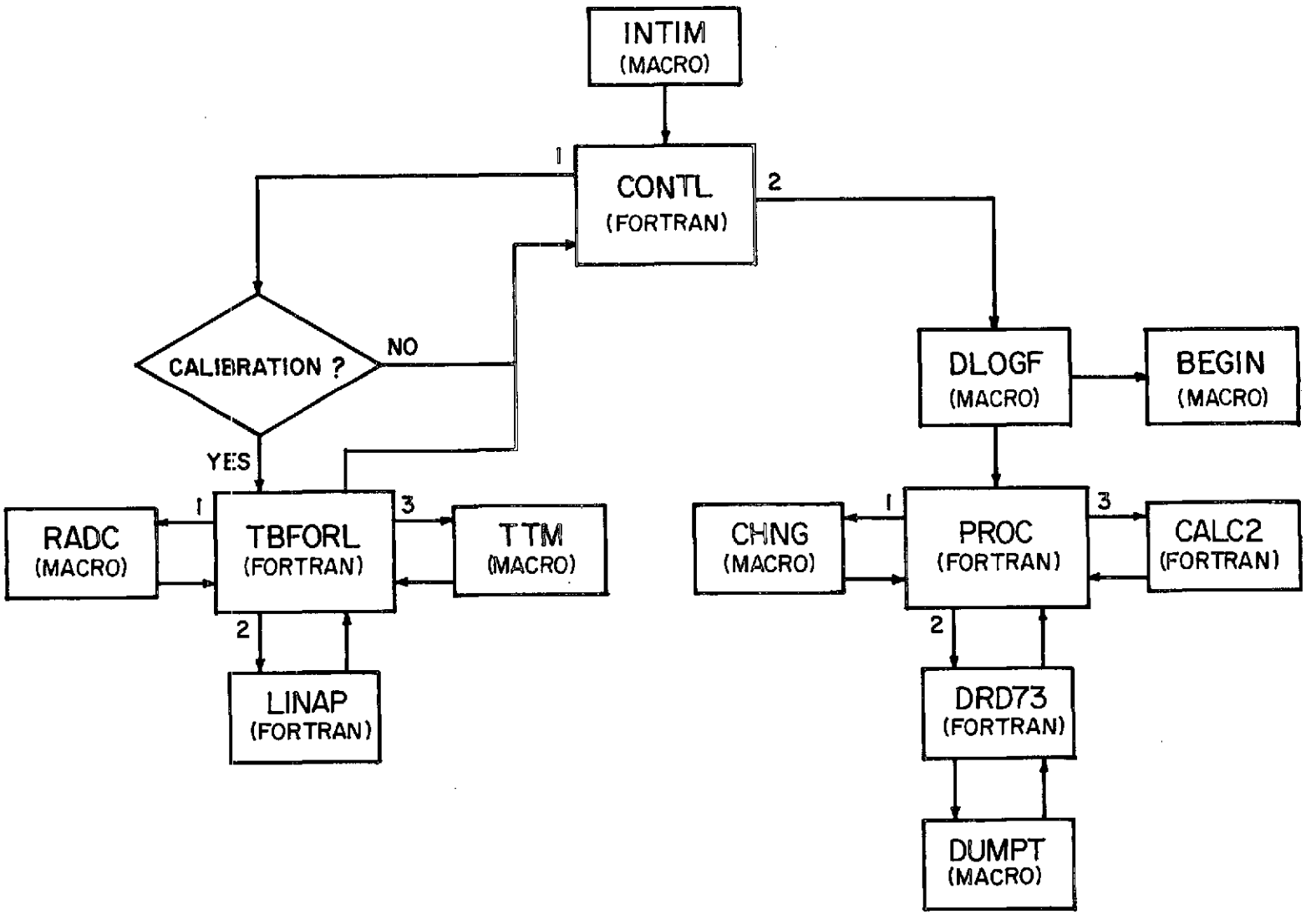

Figure 3.8 Flow diagram of the partial-reflection program.

samples are taken at heights of 60 to 90 km at 1.5 km intervals. These 26 samples make up one frame. Next, the same number of samples is taken for the received extraordinary waveform. The above cycle is repeated 513 times to collect one file of data; the file is put in disk storage. When a complete file is stored, the collection process begins again.

Also, the collection programs execute part of the noise-defeating algorithm which is referred to earlier. For the first nine frames of a file, the maximum of each frame's noise samples is determined. These nine maxima are compared to each other to determine the lowest maximum. The sum of the five noise samples with the lowest maximum is determined and stored for later use by PROC; this sum is determined for each file.

The processing programs are simultaneously operating with the data collection programs. PROC controls the other processing programs. It initiates the execution of CHNG which checks disk storage for the presence of a complete file of data; once a completed file is found, it returns execution to PROC. PROC then initiates the execution of DRD73. DRD73 and DUMPT read from disk storage the file found by CHNG and pass it to PROC. PROC applies the noise-defeating algorithm to determine the signal samples used to calculate an electron-density profile from 60 to 90 km.

The noise algorithm operates on one file of data at a time; it essentially consists of the following steps:

(a) The sum of the lowest maximum is determined for a file in the collection programs as described earlier.

(b) This sum and its corresponding file are passed to PROC where the sum is divided by five to determine the average.

(c) This average value is in effect multiplied by the square root of a "multiplying constant" to give a number which is called the

maximum allowable noise. The multiplying constant is chosen arbitrarily to give usable results. Any frame with an average noise (determined from the 5 noise samples) larger than the maximum allowable noise is rejected and not used in the electron-density calculations. The signal samples rejected by this criterion are termed "noisy" signal samples. The noise samples not rejected by this criterion are termed "acceptable" noise samples.

(d) Due to the large dynamic range of the received A_x and A_o signals, the signal samples often saturate causing the values recorded for these samples to be incorrect; therefore, any signal sample with a magnitude equal to the maximum ADC number is rejected. The signal samples rejected by this criterion are termed "saturated" signal samples.

(e) Finally, noise is extracted from the signal samples not rejected by using the noise samples in the following equations:

$$A_o = \left[\frac{\sum_{i=1}^{i=N1} (a_o)_i^2}{N1} - \frac{\sum_{i=1}^{i=N2} (a_n)_i^2}{N2} \right]^{1/2} \tag{3.1}$$

$$A_x = \left[\frac{\sum_{i=1}^{i=N3} (a_x)_i^2}{N3} - \frac{\sum_{i=1}^{i=N2} (a_n)_i^2}{N2} \right]^{1/2} \tag{3.2}$$

where a_o = the magnitude of a nonsaturated and nonnoisy ordinary signal sample

$N1$ = total number of a_o's

a_x = the magnitude of a nonsaturated and nonnoisy extraordinary signal sample

$N3$ = total number of a_x's

a_n = the magnitude of an acceptable noise sample

$N2$ = total number of a_n's.

The values of A_o and A_x given in equations (3.1) and (3.2) are determined for intervals of 1.5 km from 60 to 90 km.

PROC contains all the steps in the noise-defeating algorithm except step (a). PROC also contains equations which use the ordinary-mode noise samples to calculate an rms noise level; this noise level is also determined for the extraordinary mode. These two noise levels are again calculated after the acceptable noise samples of each mode are determined.

The values of A_o and A_x determined by equations (3.1) and (3.2) at each altitude are passed to CALC2 which calculates an electron-density profile. Control is returned to PROC which prints the results on a teletype (an example is shown in Table 3.1) and also punches the results on paper tape for storage purposes. In the near future, it is planned to use the paper tape output with an HP 9830 programmable calculator, paper tape reader, and plotter to automatically plot the data.

Once an electron-density profile has been calculated from a file of data, processing begins on the second file after CHNG finds it completed on disk storage.

As stated in step (d) of the noise-defeating algorithm, the signal samples often saturate. To alleviate this difficulty, the step attenuator of Figure 3.1 is used to attenuate the received signal; files of data are successively collected at 0 dB, 10 dB, and 25 dB attenuation.

TABLE 3.1

An example file of data that was processed by the PDP-15/30.

1210 CST 5-4-73 DAILY RUN 10 dB

MAX. ALLOW. NOISE = 77.7 MULT. CONST. = 8.000

O-NOISE AV.(1)* 17.1 O-NOISE AV.(2)** 12.1

X-Noise AV.(1) 26.7 X-NOISE AV.(2) 11.5

513 SAMPLES TAKEN 74 FRAMES REJECTED

REJ. (N.+S.)	HEIGHT (km)	AV. A_o	AV. A_x	A_x/A_o	N (cm^{-3})
74	60.0	12.2	6.6	0.54	-4536
74	61.5	13.9	18.9	1.37	2335
74	63.0	19.2	15.4	0.80	443
74	64.5	19.2	14.2	0.74	-946
74	66.0	15.4	18.9	1.23	-204
74	67.5	17.8	26.6	1.50	125
74	69.0	20.1	30.4	1.51	175
74	70.5	23.1	33.6	1.45	128
74	72.0	32.6	46.6	1.43	189
74	73.5	42.8	56.9	1.33	484
74	75.0	57.1	56.7	0.99	740
74	76.5	89.4	57.1	0.64	793
74	78.0	159.6	66.6	0.42	503
74	79.5	187.6	62.5	0.33	395
74	81.0	128.2	37.0	0.29	692
74	82.5	87.5	20.4	0.23	1274
74	84.0	77.4	13.0	0.17	2411
74	85.5	100.9	10.4	0.10	2788
74	87.0	125.8	8.3	0.07	8008
131	88.5	275.8	6.7	0.02	-5544
424	90.0	361.5	15.3	0.04	

*rms noise calculated from all ordinary noise samples.
**rms noise calculated from the acceptable ordinary noise samples.

4. EXPERIMENTAL RESULTS

4.1 *Daily Electron-Density Variations*

Preliminary results of this study are presented by *Bowhill and Denny* [1973]. Electron densities of the *D* region were measured using the partial-reflection technique at Urbana, Illinois (latitude 40.2° N) from December 1, 1972, to July 31, 1973. Signal amplitudes for the ordinary and extra-ordinary modes were recorded for a one-hour period around local noon (CST). The height resolution of these measurements was limited to 3.8 km, since the pulse width was 25 μs after passing through the receiver. Accordingly, electron densities were determined at 72, 76.5, and 81 km and plotted daily; these are to be interpreted as averages over a 4-km slab centered at the altitude specified. Following is a description of the method used to derive these electron densities.

A time interval of 3.5 minutes is needed to collect the noise and signal samples of a file. While the next file is being collected, an additional 25 to 30 seconds is required to calculate the electron densities and other information listed in Table 3.1.

The amplitudes of the received signals for both modes of circular polarization are often beyond the dynamic range of the receiver; thus, saturation results, and incorrect values are recorded for the A_x and A_o signal samples. To alleviate this difficulty, a step attenuator is used at the receiver input. The first file of data is collected with the received signals attenuated by 0 dB. Then, a file is collected at 10 dB attenuation after which a file is collected at 25 dB attenuation. This is continued until 15 files are collected and processed.

In most cases, the signal samples of a file will begin saturating at higher altitudes. Since the saturation of signal samples causes erroneous results, electron densities are rejected if they are calculated using an A_x/A_o ratio at an altitude where 10 or more signal samples saturated. The criterion of 10 saturated samples is arbitrarily chosen; it is approximately 2% of 513 samples (the number of A_o and A_x samples collected at each altitude). By using Table 3.1, the number of signal samples (A_o plus A_x) which saturate at a particular altitude is determined by subtracting the number of rejected frames from the number of total rejections; the number of rejected frames is the number of noisy signal samples rejected at each altitude, while the number of total rejections at each altitude is the number of rejected frames plus the number of saturated signal samples. (The number of total rejections is listed in the first column of Table 3.1.) For example, the number of saturated signal samples at 88.5 km and 90 km in Table 3.1 is 57 and 350, respectively; thus, the two electron densities which are calculated from the A_x/A_o ratios at these altitudes are not used. This process is done to the 0 dB, 10 dB, and 25 dB files to determine the acceptable electron densities in each.

Since partial reflections from 60 to 70 km are very weak, the electron densities at these altitudes are determined from those given in a file which is collected with the ordinary and extraordinary received signals unattenuated (0 dB). Thus, a composite electron-density profile is partially determined by using the acceptable electron densities from the 0 dB file; the acceptable electron densities of the 10 dB file are used for altitude intervals where electron densities are rejected in the 0 dB file. Finally, the acceptable electron densities of the 25 dB file are used to complete the composite electron-density profile.

Since there are 15 files of data collected each day, five composite profiles are determined. From these five profiles, the median electron density is found at each altitude, resulting in a daily profile. A daily profile of the A_x/A_o ratio is also determined in the same manner as the electron-density profile.

The median, rather than the mean, electron density is used to find the daily profile due to the extreme irregularities which can occur in the results, e.g. the negative electron densities of Table 3.1. Averaging will bias the values toward an extreme, while the median best represents the correct value.

As seen in equation (2.14), the electron density in a particular altitude interval is dependent on the A_x/A_o ratio at two altitudes. Once the daily profile is determined, the electron density which is dependent on the A_x/A_o ratios at 70.5 and 72 km is averaged with the electron density which is dependent on the A_x/A_o ratios at 72 and 73.5 km; this average electron density applies to an altitude interval centered at 72 km. Similarly, average electron densities which apply to altitude intervals centered at 76.5 and 81 km are determined. These three values are plotted daily and presented in Figures 4.1 to 4.8. The electron densities at 72, 76.5, and 81 km are indirectly related to a different set of three A_x/A_o ratios; therefore, each electron density is independent of the other two. The curves which are presented in Figures 4.1 to 4.8 are left blank on days when measurements were not made. The dashed sections of the 81-km electron-density curve indicate that the differential absorption produced was too high to be accurately measured at the frequency used; on those days simultaneous measurements at a higher frequency would have been helpful. On December 12, 1972, and February 21,

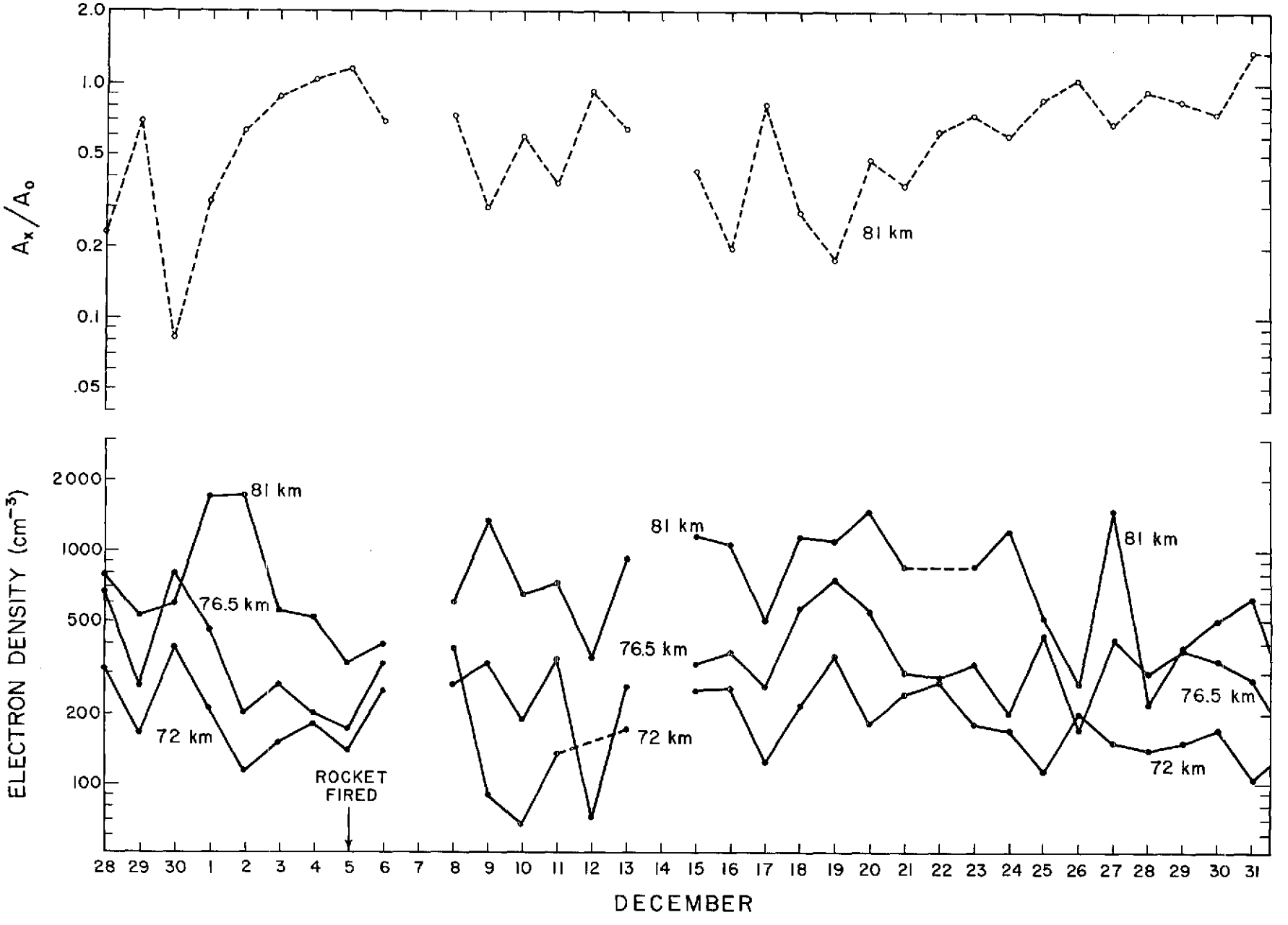

Figure 4.1 Daily plot of electron density at 72, 76.5 and 81 km and A_x/A_o ratio at 81 km for December, 1972.

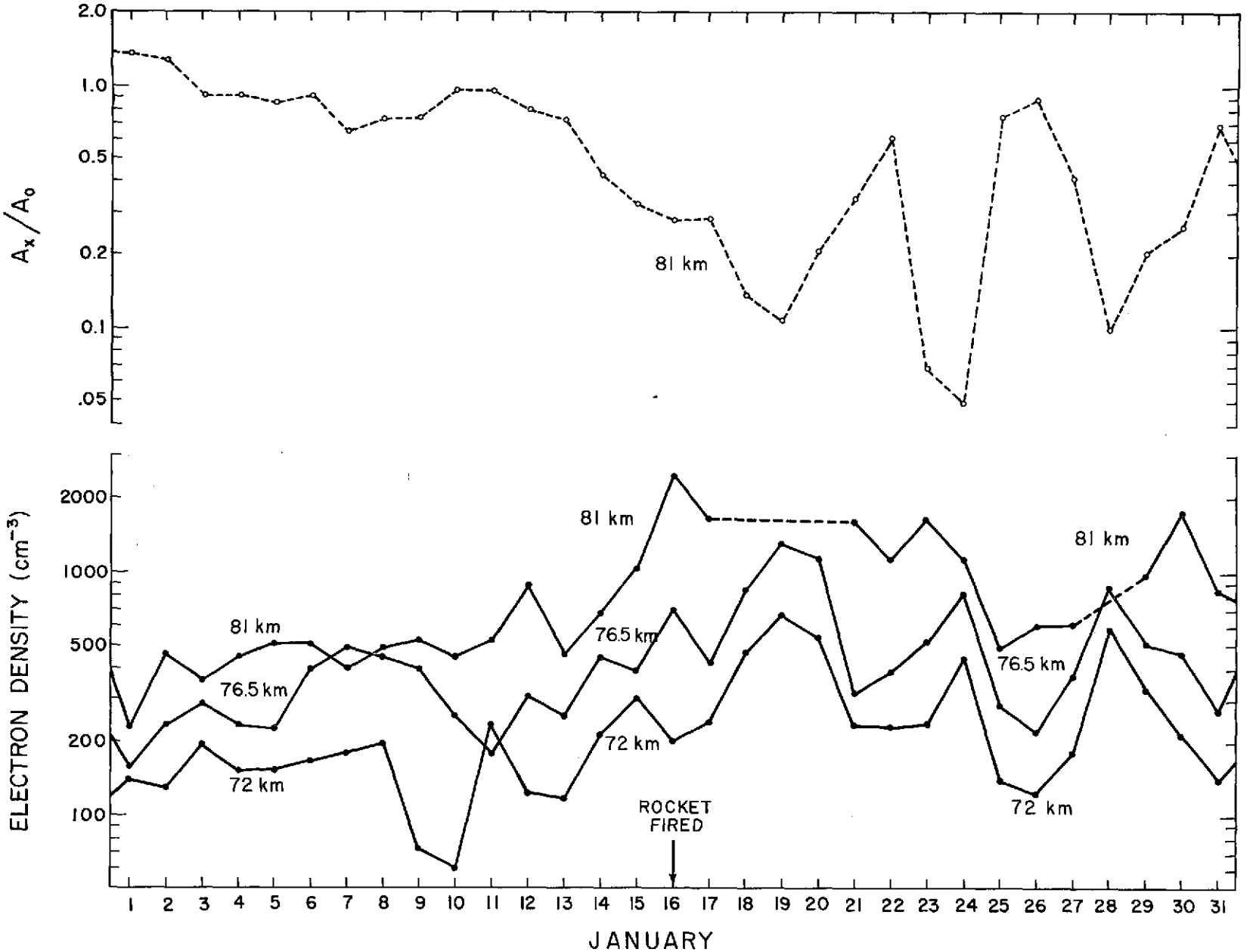

Figure 4.2 Daily plot of electron density at 72, 76.5 and 81 km and A_x/A_o ratio at 81 km for January, 1973.

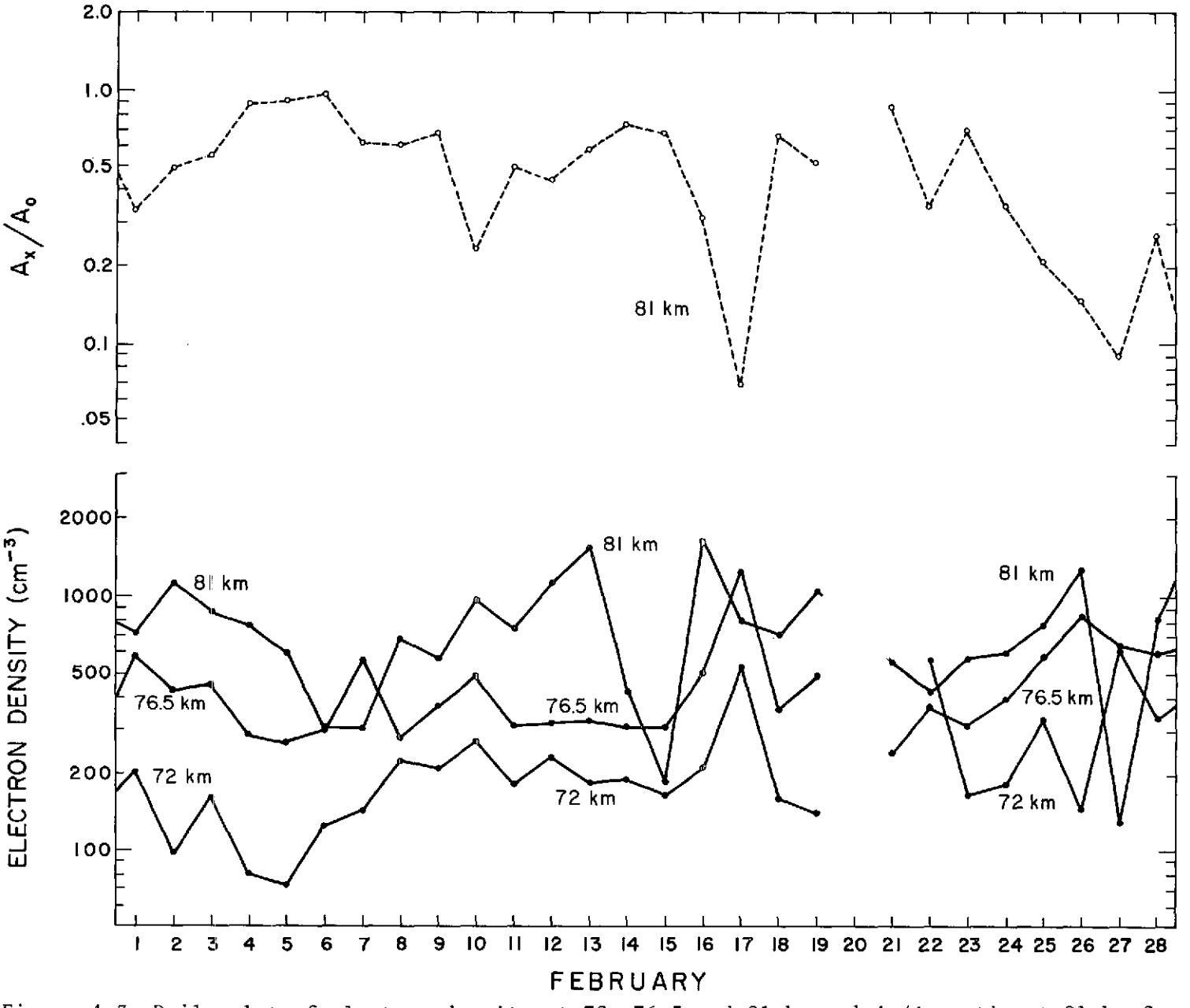

Figure 4.3 Daily plot of electron density at 72, 76.5 and 81 km and A_x/A_o ratio at 81 km for February, 1973.

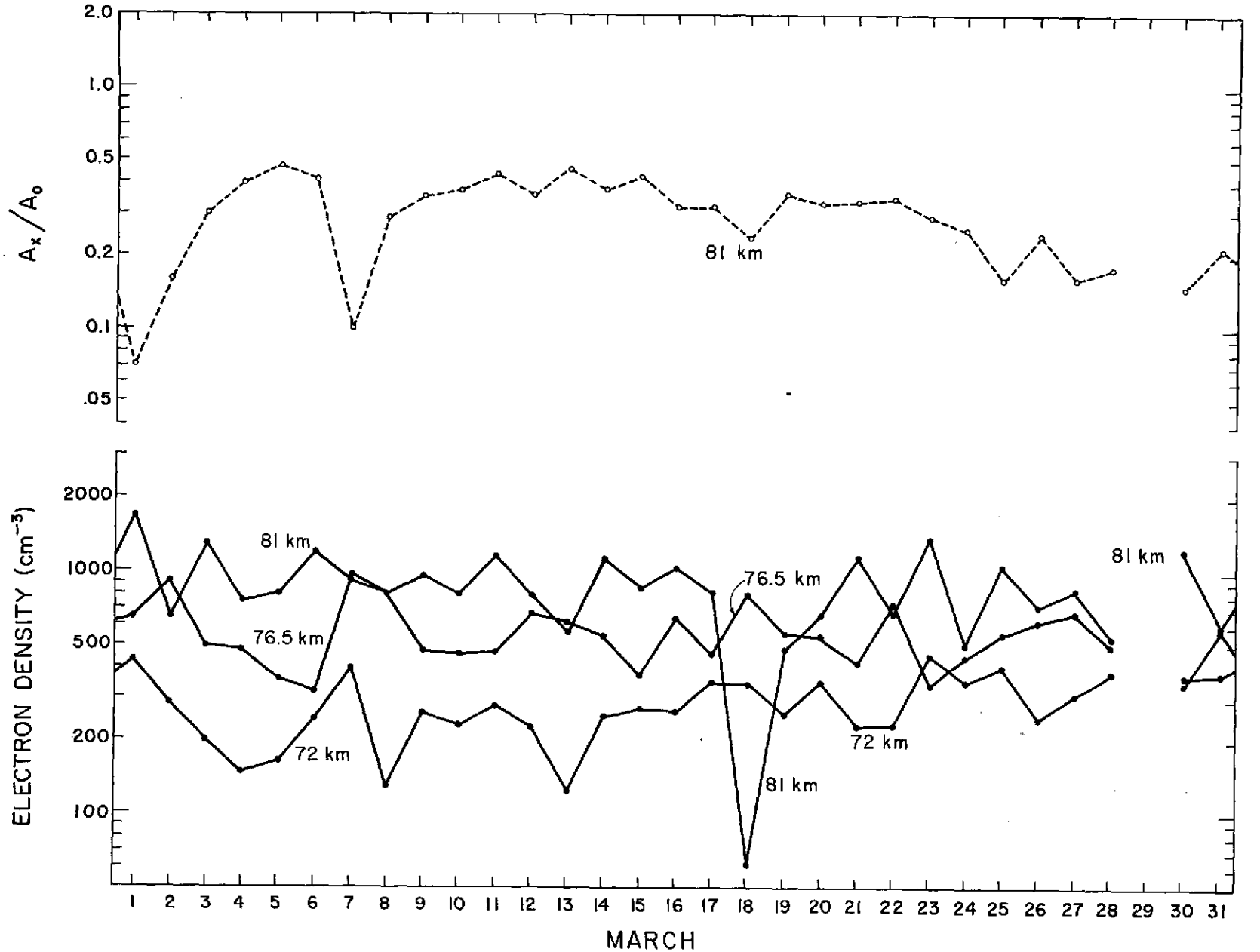

Figure 4.4 Daily plot of electron density at 72, 76.5 and 81 km and A_x/A_o ratio at 81 km for March 1973.

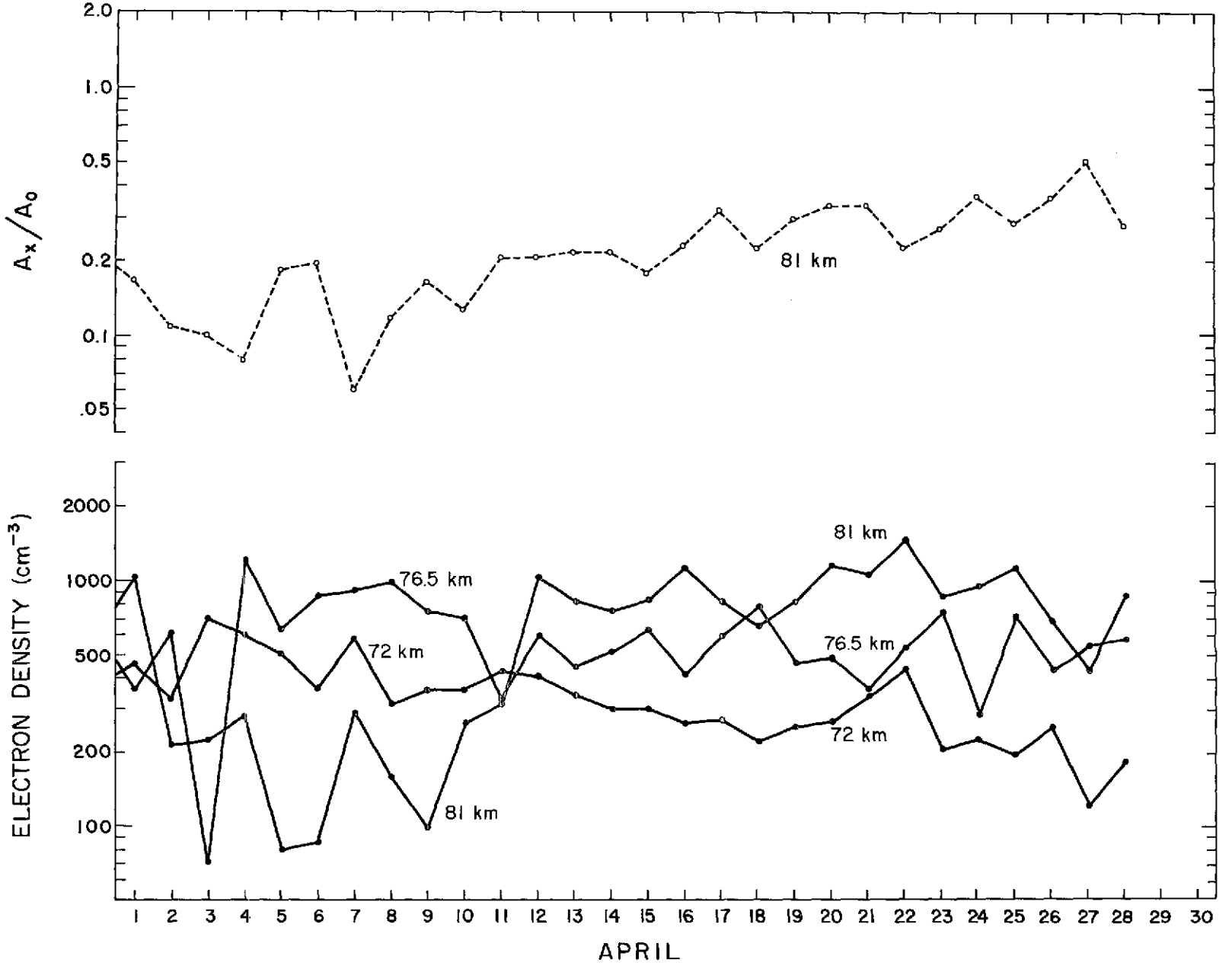

Figure 4.5 Daily plot of electron density at 72, 76.5 and 81 km and A_x/A_o ratio at 81 km for April, 1973.

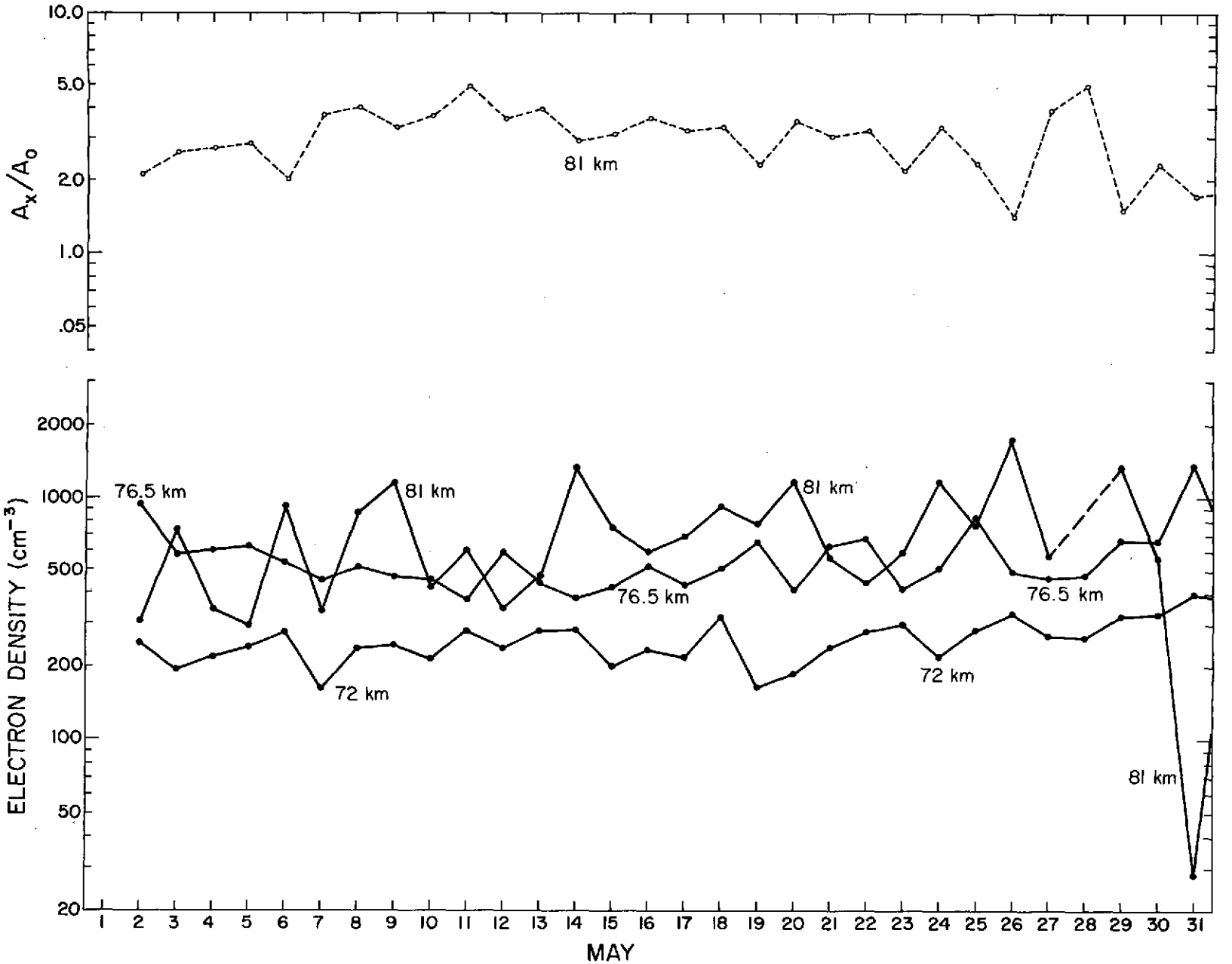

Figure 4.6 Daily plot of electron density at 72, 76.5 and 81 km and A_x/A_o ratio at 81 km for May, 1973.

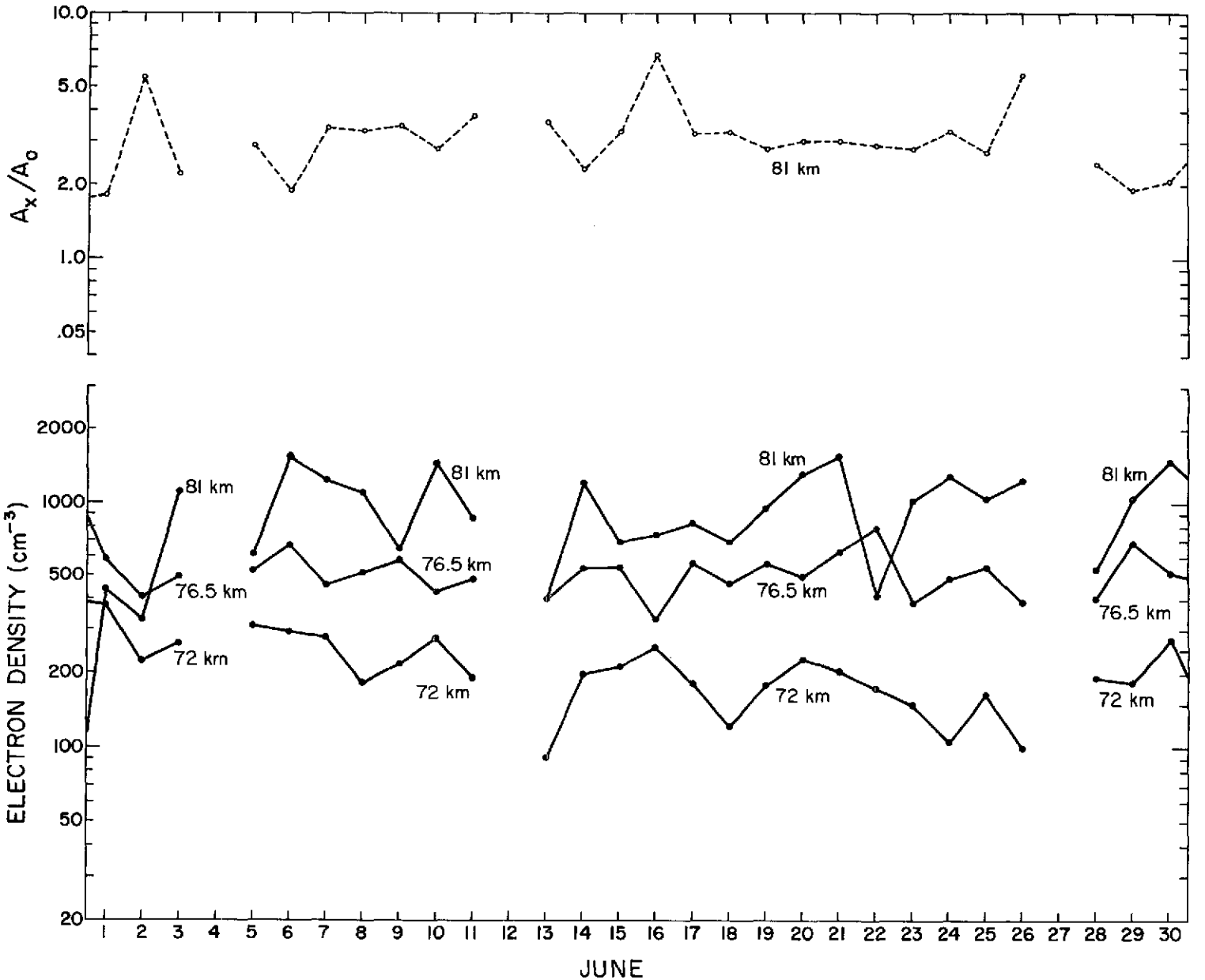

Figure 4.7 Daily plot of electron density at 72, 76.5 and 81 km and A_x/A_O ratio at 81 km for June, 1973.

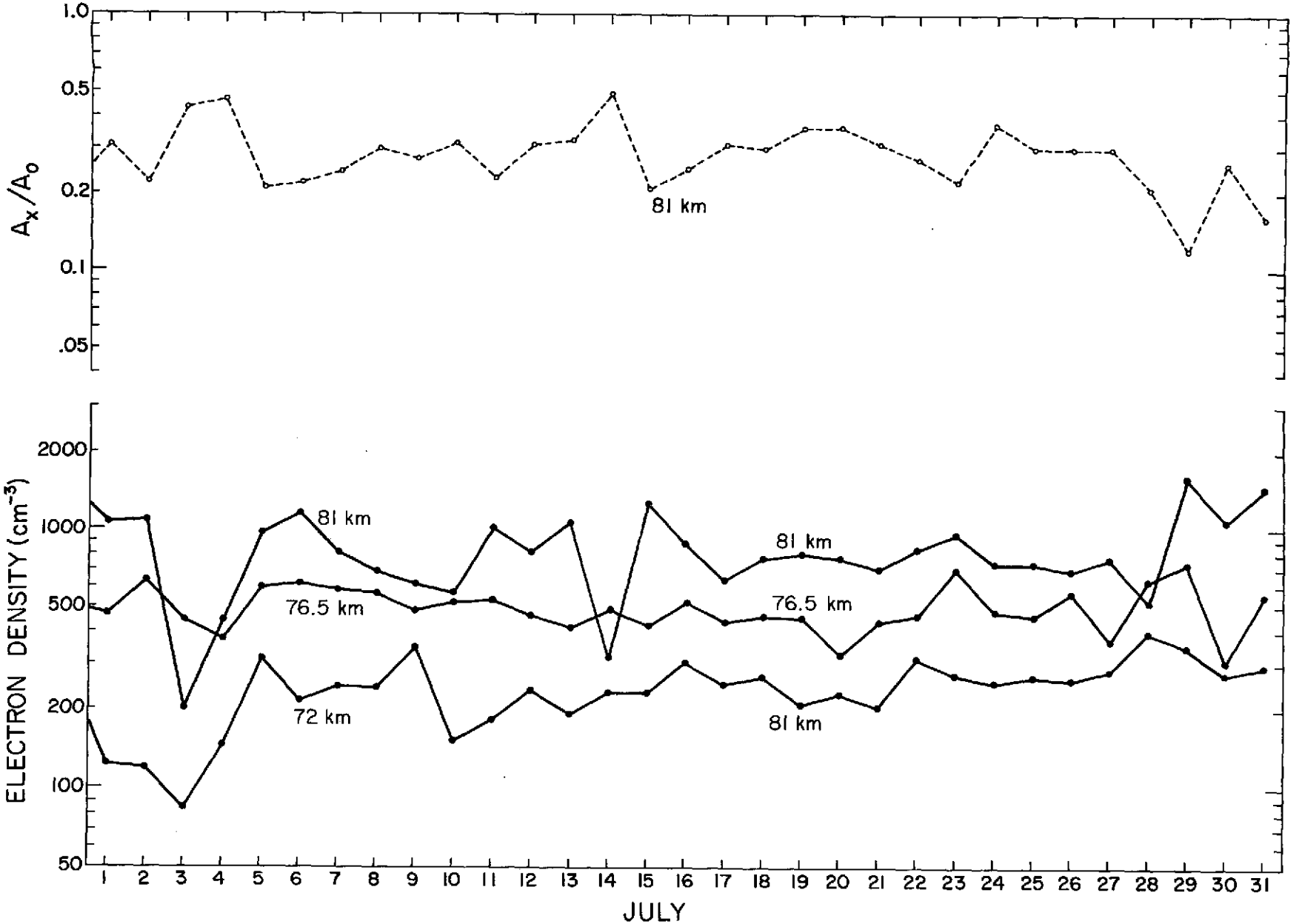

Figure 4.8 Daily plot of electron density at 72, 76.5 and 81 km and A_x/A_o ratio at 81 km for July, 1973.

1973, the electron density at 72 km is not plotted because the signal-to-noise ratio was very poor causing inaccurate measurements around this altitude.

The daily A_x/A_o ratio at 81 km is shown in Figures 4.1 to 4.8; its logarithm represents the total differential absorption occurring below the altitude of 81 km. Thus, a daily plot of the A_x/A_o ratio at 81 km represents a measure of the *D*-region ionization variation below 82 km. A high value of this ratio indicates a low absorption due to a low electron density, and vice versa; therefore, variations between the A_x/A_o ratio at 81 km and the electron density will be negatively correlated. In most cases, this is observed in Figures 4.1 to 4.8.

For the first half of January, the A_x/A_o ratio and the electron densities in Figure 4.2 were reasonably well behaved. However, beginning about January 13, a very pronounced wave-like variation with a period of about 5 days developed and lasted until early February; it is apparently associated with the development of a major stratospheric warming which occurred in early February. A closer examination of the electron-density curves shows that each of them vary by essentially the same ratio (as much as a factor of 5). Also, there is no phase difference in the variations; electron-density enhancements at the upper altitudes do not precede or follow those at the lower altitudes. This suggests that the same mechanism simultaneously produces electron-density enhancements throughout this height region. This conclusion is reinforced by Figure 4.9 which is a scatter plot of the electron densities at 72 km versus 76.5 km. A strong correlation is evident between the electron densities at these altitudes. A correlation is also evident in the scatter plot between the electron densities at 76.5 and 81 km as shown in Figure 4.10.

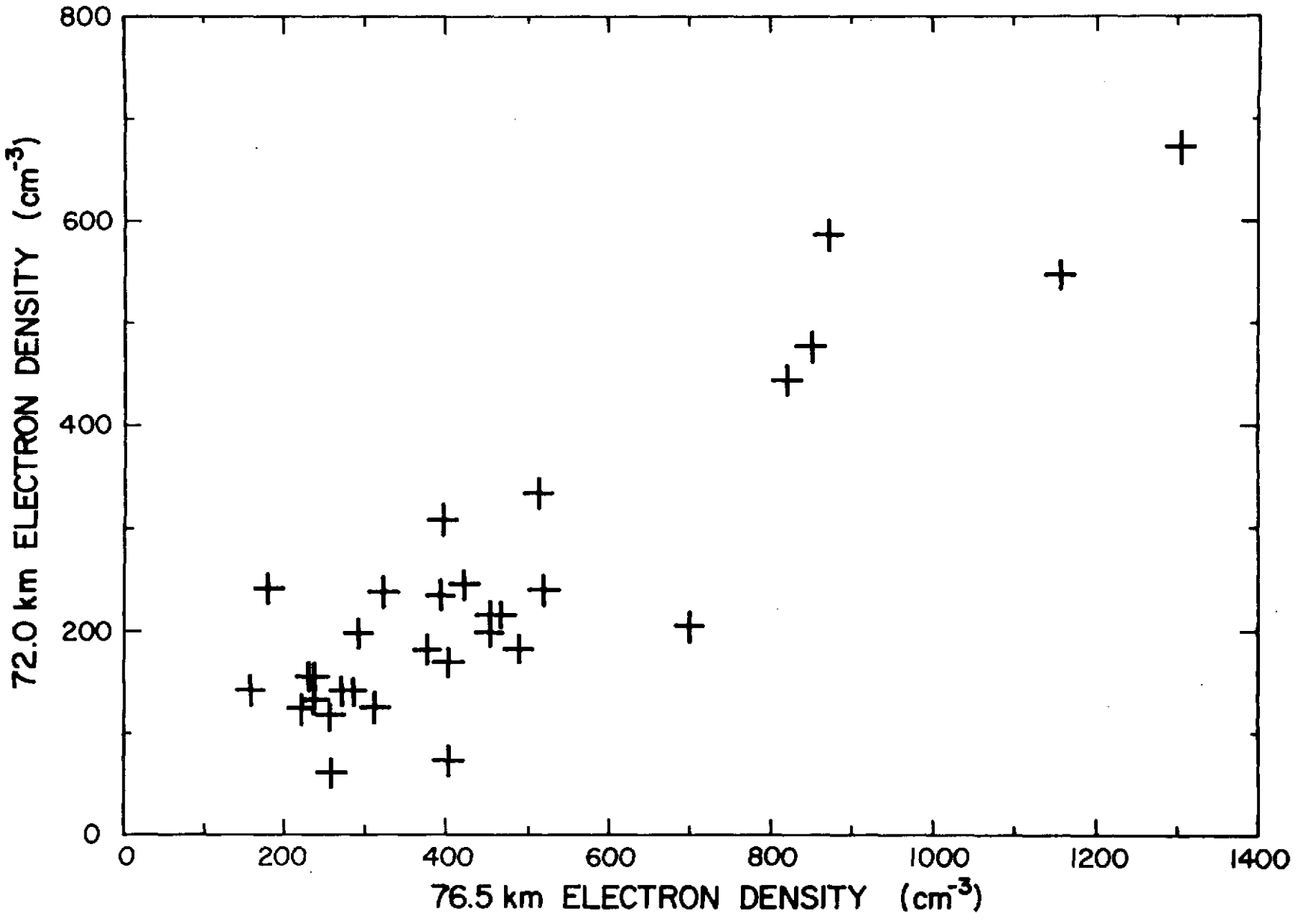

Figure 4.9 Scatter plot of the electron densities at 72 km versus those at 76.5 km.

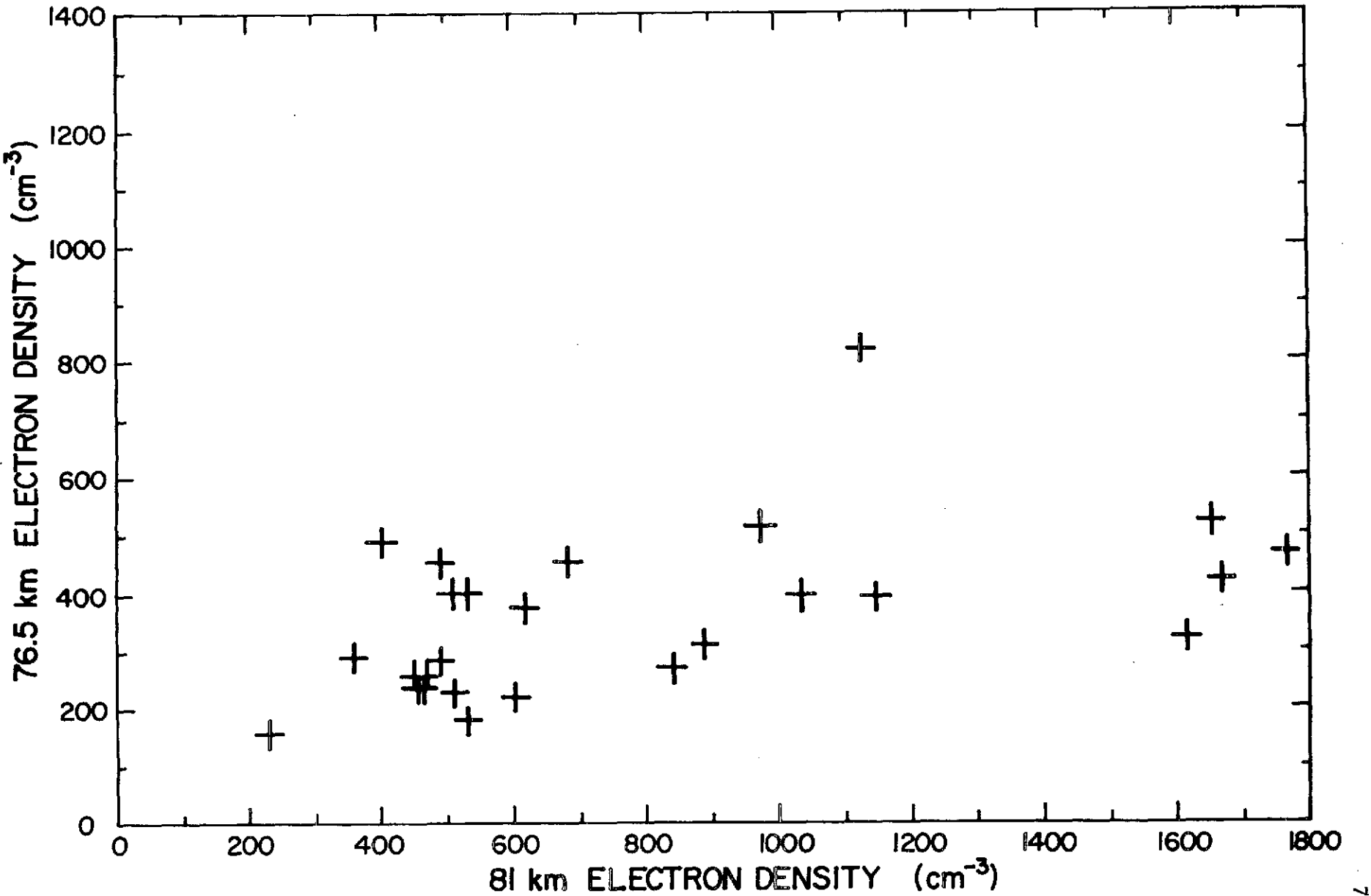

Figure 4.10 Scatter plot of the electron densities at 76.5 km versus those at 81 km.

These cyclical variations are observed at other periods during the winter months of December, January, and February, however, not as well pronounced. After February, the cyclical variations almost completely cease.

4.2 10-mb *Data*

The wave-like structure of the electron-density curves which are displayed in Figure 4.2 for the latter part of January is of particular interest, and is studied with data from 10-mb contour maps to determine the correlation between ionization changes in the *D* region and meteorological changes in the stratosphere.

Daily contour maps of the 10-mb height and temperature for the Northern Hemisphere were obtained from the National Meteorological Center in Maryland. 10-mb heights are read from these maps at 50° latitude by longitudinal increments of 20°, beginning at 90° longitude. These heights are used to determine the average 10-mb height at 50° latitude. The average is subtracted from the 10-mb height at 50° latitude and 90° longitude to determine its deviation from the average. The deviation is determined on a daily basis from January 10 to February 10, 1973, as shown in Figure 4.11.

Comparison of the 10-mb deviation curve of Figure 4.11 with the A_x/A_o-ratio and electron-density curves of Figures 4.2 and 4.3 does not reveal any obvious correlation. However, closer inspection of the 10-mb deviation curve from January 12 to 26 shows that cyclical variations with a period of about 5 days are discernible from the longer-period variations. In order to obtain a better representation of the shorter-period variations, the 10-mb deviation curve is numerically analyzed to eliminate all cyclical variations with a period greater than 7 days. The IBM subroutine called HARM is used to perform the numerical analysis.

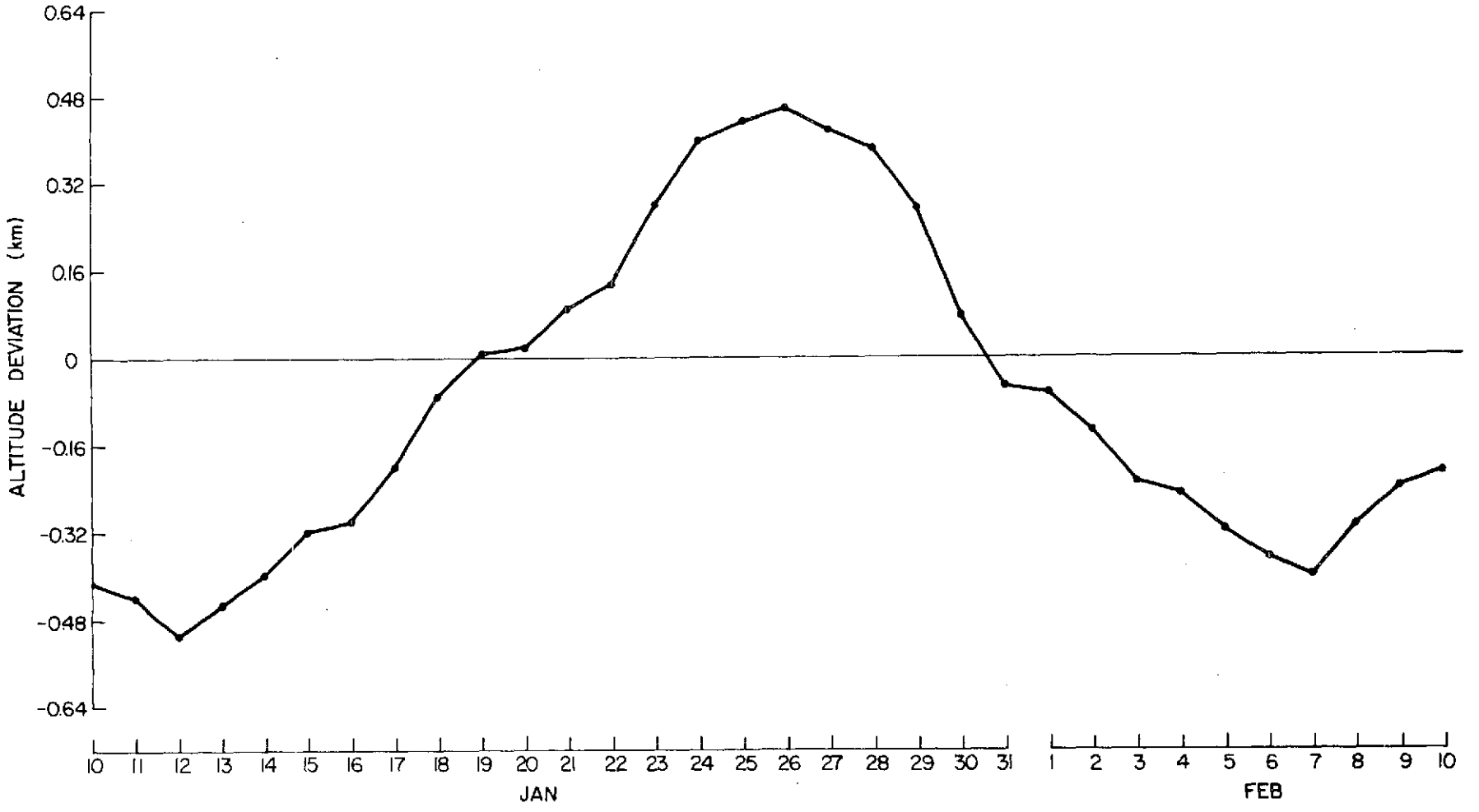

Figure 4.11 Deviation of the 10-mb height at 90° longitude and 50° latitude from the average 10-mb height at 50° latitude.

4.3 *Numerical Analysis of Data*

HARM is a FORTRAN subroutine that is described in the manual entitled *IBM System/360 Scientific Subroutine Package (360-CM-03X), Version III, Programmer's Manual* in sufficient detail to permit the reader to understand and use it. It is capable of performing the discrete Fourier transforms on a complex three-dimensional array using the method described by *Cooley and Tukey* [1965]. An example follows that shows how HARM is used.

The function given by equation (4.1) is sampled at a rate of 1 sample per second; the sampled waveform is shown in Figure 4.12(a)

$$f(t) = \sin\left(\frac{2\pi}{32}\,t\right) + \sin\left(\frac{8\pi}{32}\,t\right) \qquad (4.1)$$

t = time in seconds

By using HARM, the discrete Fourier transform of the waveform in Figure 4.12(a) is calculated, resulting in a frequency spectrum. The frequency spectrum is multiplied by the magnitude characteristic of an ideal high-pass filter with a cutoff frequency of 3/32 Hz; this eliminates the lower-frequency component. Finally, HARM is used to calculate the inverse discrete Fourier transform of the frequency spectrum after the lower-frequency component is removed. Ideally, the resulting waveform $g(t)$ in Figure 4.12(b) will be a sampled sine wave with a period of 8 seconds and a maximum amplitude of one. However, due to errors introduced when sampling a finite-length waveform, the ideal case can only be approximated. There is essentially no error at the middle of the waveform in Figure 4.12(b), but the error increases toward the ends.

The 10-mb height deviation of Figure 4.11 is numerically filtered to eliminate all variations with a period greater than 7 days. For the same

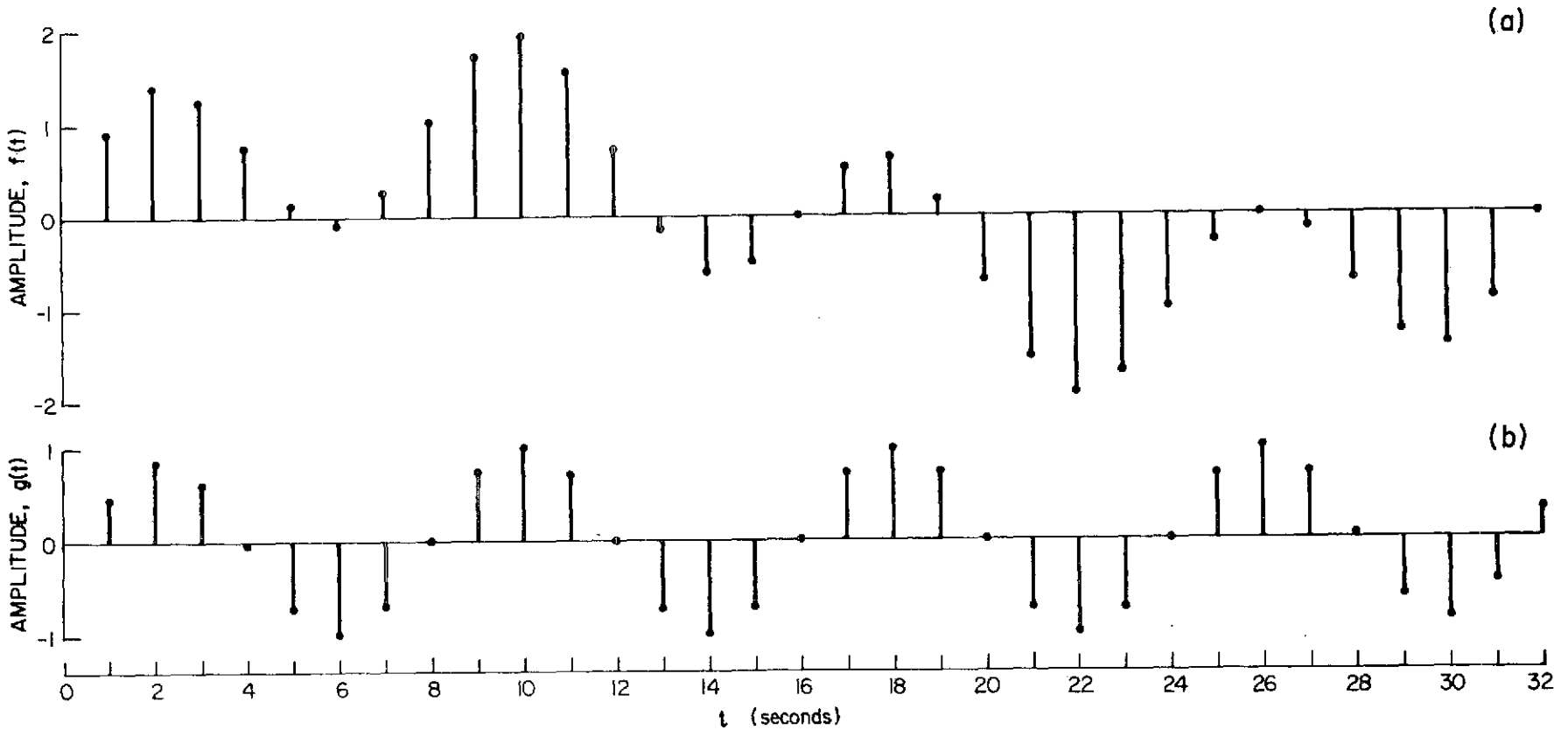

Figure 4.12 (a) Sampled waveform given by equation (4.1), (b) sampled waveform after being high-pass filtered to eliminate the lower frequency component.

time period, this process is applied to the natural logarithm of the A_x/A_o-ratio curve in Figures 4.2 and 4.3 and the electron-density curves at 72, 76.5, and 81 km in Figures 4.2 and 4.3. (Since HARM requires a constant sampling interval, the 81-km electron densities which are not plotted in Figure 4.2 were chosen from the values crossed by the dashed lines.) All the filtered waveforms are shown in Figure 4.13. It is obvious that a high correlation exists between the 10-mb height variations and the electron-density variations at 72 and 76.5 km; a strong negative correlation is evident between the 10-mb height variations and the $\ln(A_x/A_o)$ variations. A significant observation of Figure 4.13 is that the electron-density enhancements occur approximately at the same time as increases in the 10-mb height.

To get a better insight to the extent of the correlations, the correlation coefficient r between various parameters is calculated using the following equation

$$r = \frac{N\Sigma xy - (\Sigma x)(\Sigma y)}{\left[(N\Sigma x^2 - (\Sigma x)^2)(N\Sigma y - (\Sigma y)^2)\right]^{1/2}}$$

where N is the sample size of the parameters x and y. A correlation of 1 is a perfect correlation, while a -1 is a completely negative correlation, and 0 means the two parameters varied in a random manner.

4.4 *Correlation Between* 10-mb *Data and Partial-Reflection Measurements*

In Figure 4.13, it is apparent that from January 18 to February 6 the correlations between the electron densities at 72 and 76.5 km and the 10-mb height are much stronger; therefore, the correlation coefficients of Table 4.1 are calculated for two time periods.

The decreasing correlation (Table 4.1) between the $\ln(A_x/A_o)$ curve at 81 km and the electron densities at increasing altitudes indicates that the

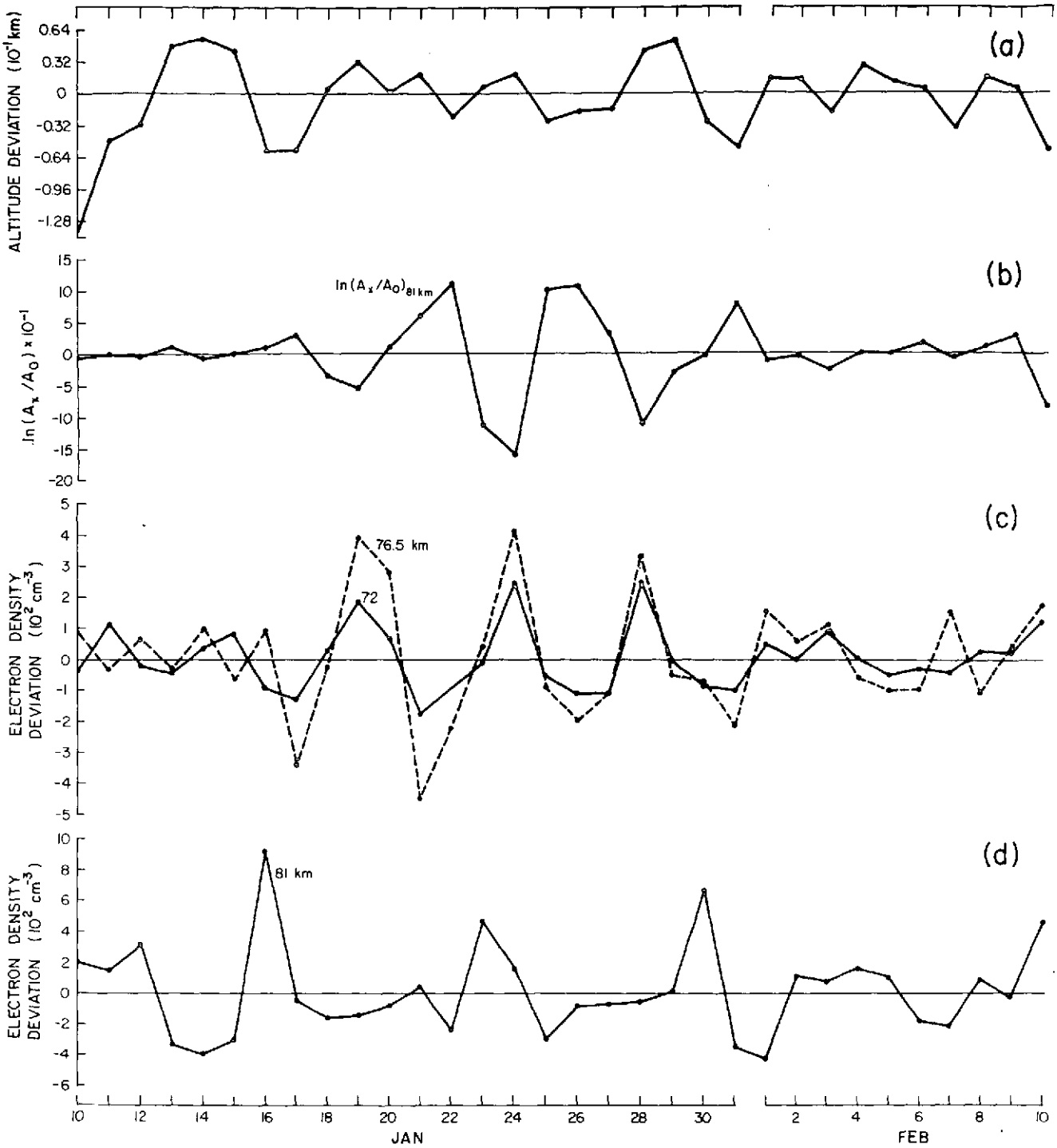

Figure 4.13 Each curve has cyclical variations with periods greater than 7 days removed, they are: (a) 10-mb height at 50° latitude and 90° longitude, (b) the natural logarithm of the A_x/A_o ratio at 81 km ($\ln(A_x/A_o)_{81\ km}$), (c) electron density at 72 and 76.5 km, and (d) electron density at 81 km.

TABLE 4.1

Correlation coefficients between parameters plotted in Figure 4.13.

Parameters		Correlation Coefficients	
x	y	January 10 to February 10	January 18 to February 6
$\ln(A_x/A_o)_{81\ km}$	$N_{72\ km}$	-0.75	-0.78
$\ln(A_x/A_o)_{81\ km}$	$N_{76.5\ km}$	-0.73	-0.74
$\ln(A_x/A_o)_{81\ km}$	$N_{81\ km}$	-0.33	-0.44
$N_{72\ km}$	$N_{76.5\ km}$	0.82	0.95
$N_{76.5\ km}$	$N_{81\ km}$	0.12	0.06
10-mb height	$\ln(A_x/A_o)_{81\ km}$	-0.25	-0.60
10-mb height	$N_{72\ km}$	0.35	0.57
10-mb height	$N_{76.5\ km}$	0.14	0.52
10-mb height	$N_{81\ km}$	-0.36	0.12

A_x/A_o ratio at 81 km was affected more by the differential absorption at the lower altitudes since the electron collision frequency is much greater at lower altitudes. From the correlation coefficients between the electron densities at the three altitudes, it is seen that the lower altitude electron densities are more highly correlated than the upper altitude electron densities. Finally, the correlation coefficients of Table 4.1 show that there is a strong correlation of the 10-mb height variations at 50° latitude and 90° longitude with electron-density changes at 72 and 76.5 km.

The lack of a high correlation between the 10-mb height variation and the electron density at 81 km can be explained by comparing the partial-reflection measurements with those made at Wallops Island (geographic coordinates 38°N, 76°W) on December 5, 1972, and January 16, 1973. Using a combined rocket-borne probe and radio frequency experiment, *Mechtly, et al.* [1973] measured the electron-density profile from 50 to 110 km as shown in Figure 4.14. The December 5 profile was measured on a day of low ionization while the January 16 profile was measured on a day of high ionization. (Electron densities in Figure 4.2 indicate that the ionization was even higher on January 19.) In the 80 to 95 km range of Figure 4.14, the electron-density difference is approximately a factor of 10. A comparison of the electron densities measured by the two techniques is presented in Table 4.2. The maximum difference occurring on December 5 is -13% at 76.5 km. On January 16 the differences at 72 and 76.5 km are extremely small, but a difference of -47% is observed at 81 km. However, this large value can possibly be explained if a steep gradient in electron density occurred over Urbana near 81 km, as it did at Wallops Island as shown in Figure 4.14. Errors in electron densities are introduced when partial-reflection measurements are made near altitudes

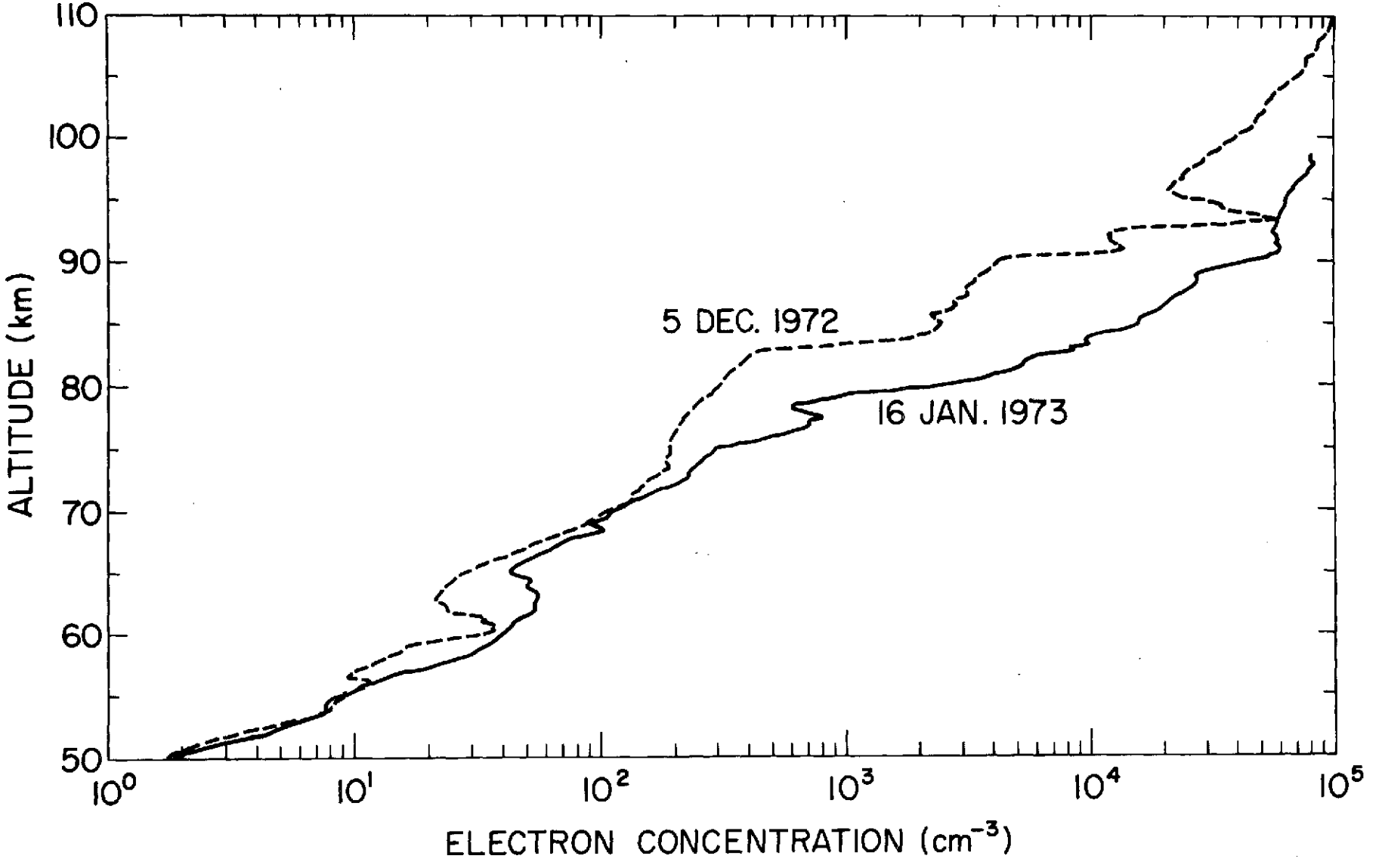

Figure 4.14 Rocket-borne measurements of the electron-density profile at Wallops Island, 38°N, 76°W [*Mechtly, et al.*, 1973].

TABLE 4.2

Comparison of electron densities determined by partial-reflection (P.R.) measurements at Urbana and the rocket measurements at Wallops Island.

	December 5, 1972			January 16, 1973		
	$N_{P.R.}$ (cm^{-3})	N_{Rocket} (cm^{-3})	% Difference	$N_{P.R.}$ (cm^{-3})	N_{Rocket} (cm^{-3})	% Difference
$N_{72\ km}$	140	150	-6.7%	205	200	+2.5%
$N_{76.5\ km}$	174	200	-13.0%	701	700	+0.1%
$N_{81\ km}$	336	340	-1.2%	2487	4700	-47.0%

of a steep electron-density gradient; since a finite pulse width is used, strong reflections caused by the high electron density above the gradient contaminate signals reflected near the gradient. Thus, the measured electron densities are smaller than the correct values at the altitudes where the contamination occurs. The results shown in Table 4.2 suggest that ionization changes below 82 km associated with the winter anomaly extend over a horizontal scale of at least 1000 km.

The monthly correlation coefficients between the electron densities at 72 and 76.5 km from Figures 4.1 to 4.8 are shown in Figure 4.15. A high correlation during the month of January, prior to the major stratospheric warming in early February, is evident. The correlation decreases to a minimum in March, and then reaches a peak in May which is a period of transition from the winter eastward winds to the summer westward winds.

4.5 *Monthly Profiles*

Monthly electron-density profiles are determined from the daily profiles discussed in Section 4.1 by using the median electron densities at each altitude. The monthly profiles of December to July are shown in Figures 4.16 to 4.19.

A pronounced "valley" in electron density around 66 km is observed in the profiles of December, January, and February; it disappears in the profiles of March and April, then reappears in May, June, and July. A similar valley is observed in the profiles determined by rocket measurements on December 15, 1965 (Figure 1.5), and December 5, 1972 (Figure 4.14); however, rocket measurements usually do not reveal a valley in electron density at this altitude.

A comparison of the profiles in the 70 to 80 km range indicates that a general increase in electron density occurred from December to March. The

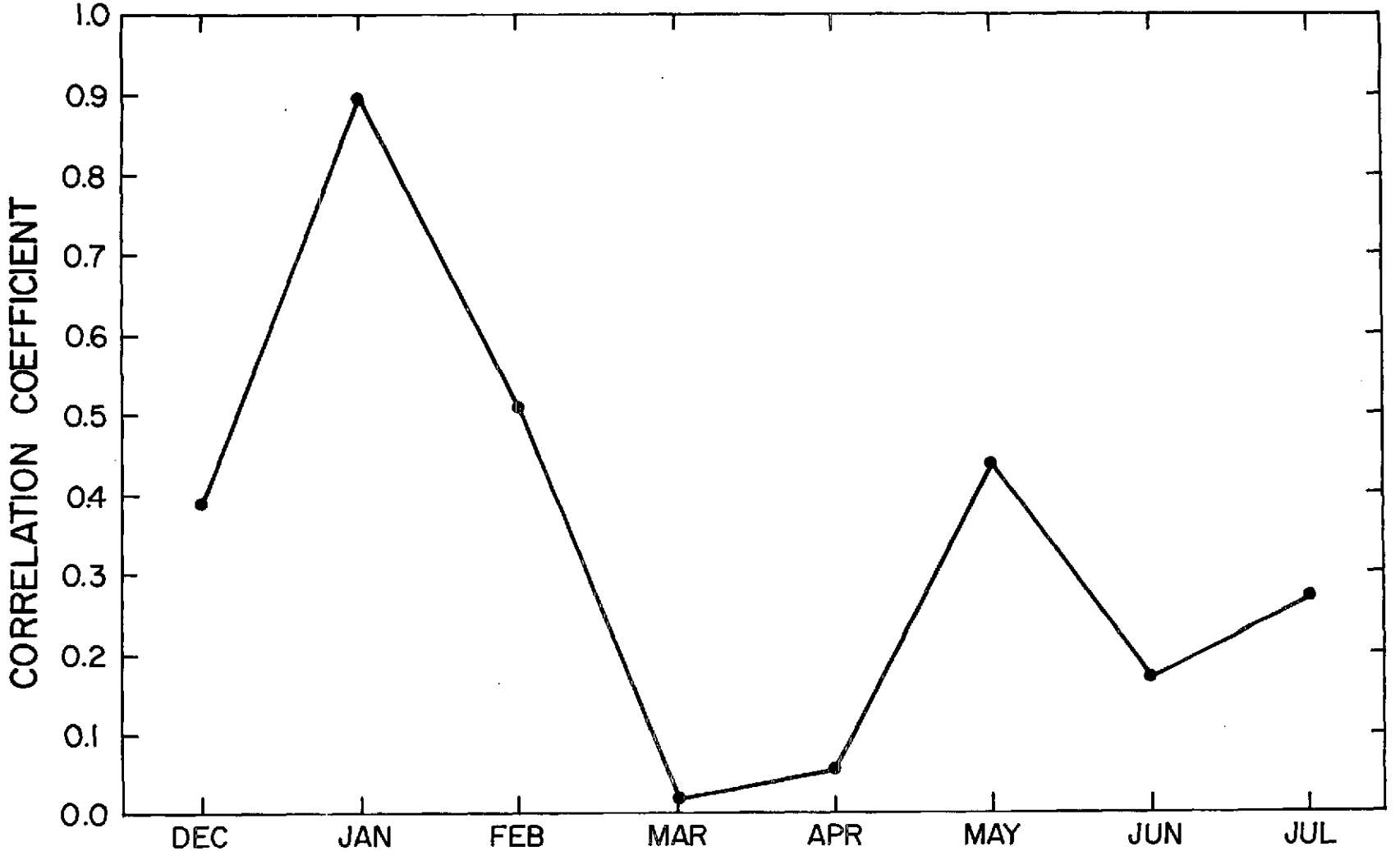

Figure 4.15 Monthly correlation coefficients between the electron densities at 72 km and 76.5 km in Figures 4.1 to 4.8.

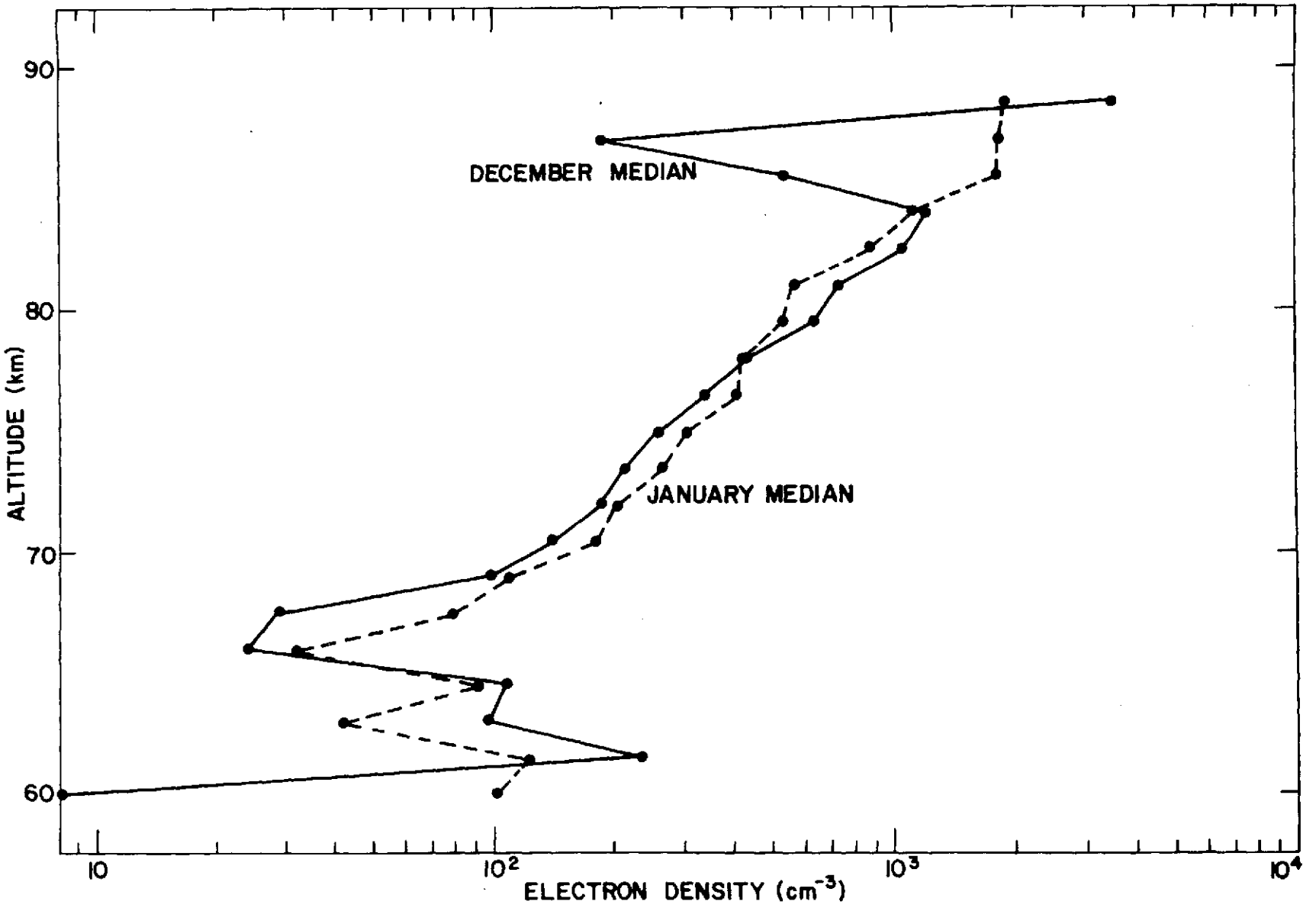

Figure 4.16 Median electron-density profiles for December, 1972 and January, 1973.

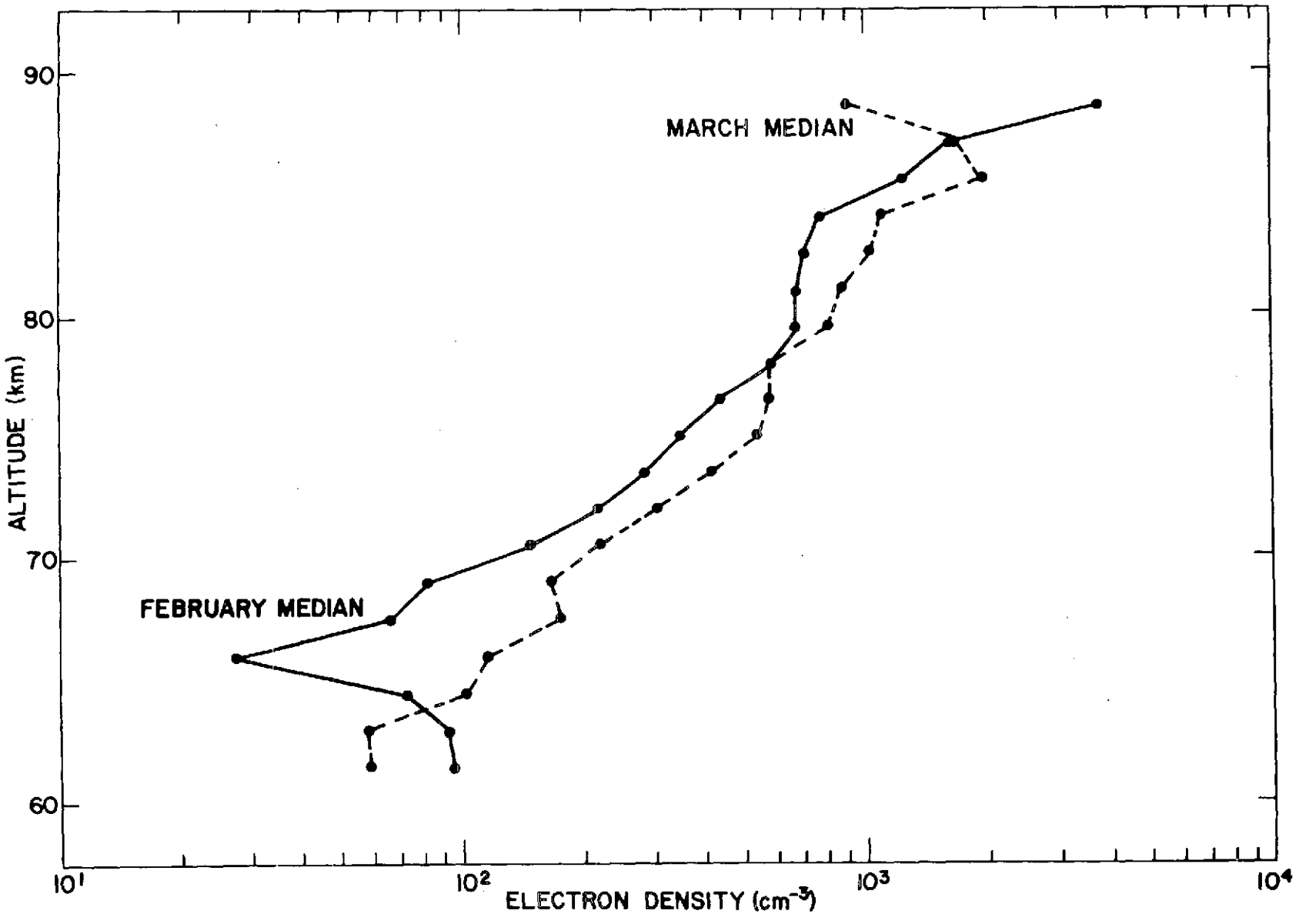

Figure 4.17 Median electron-density profiles for February, 1973 and March, 1973.

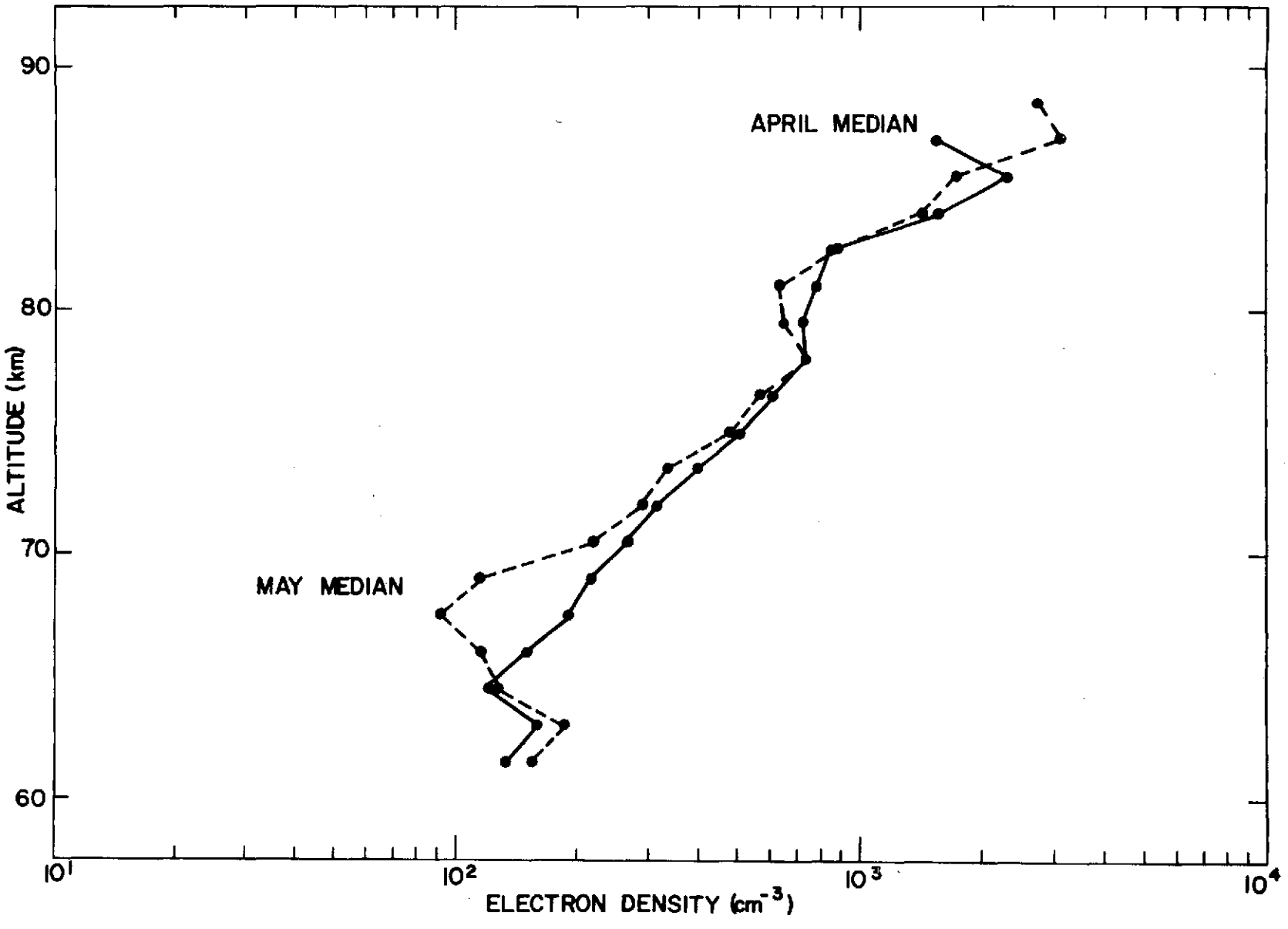

Figure 4.18 Median electron-density profiles for April, 1973 and May, 1973.

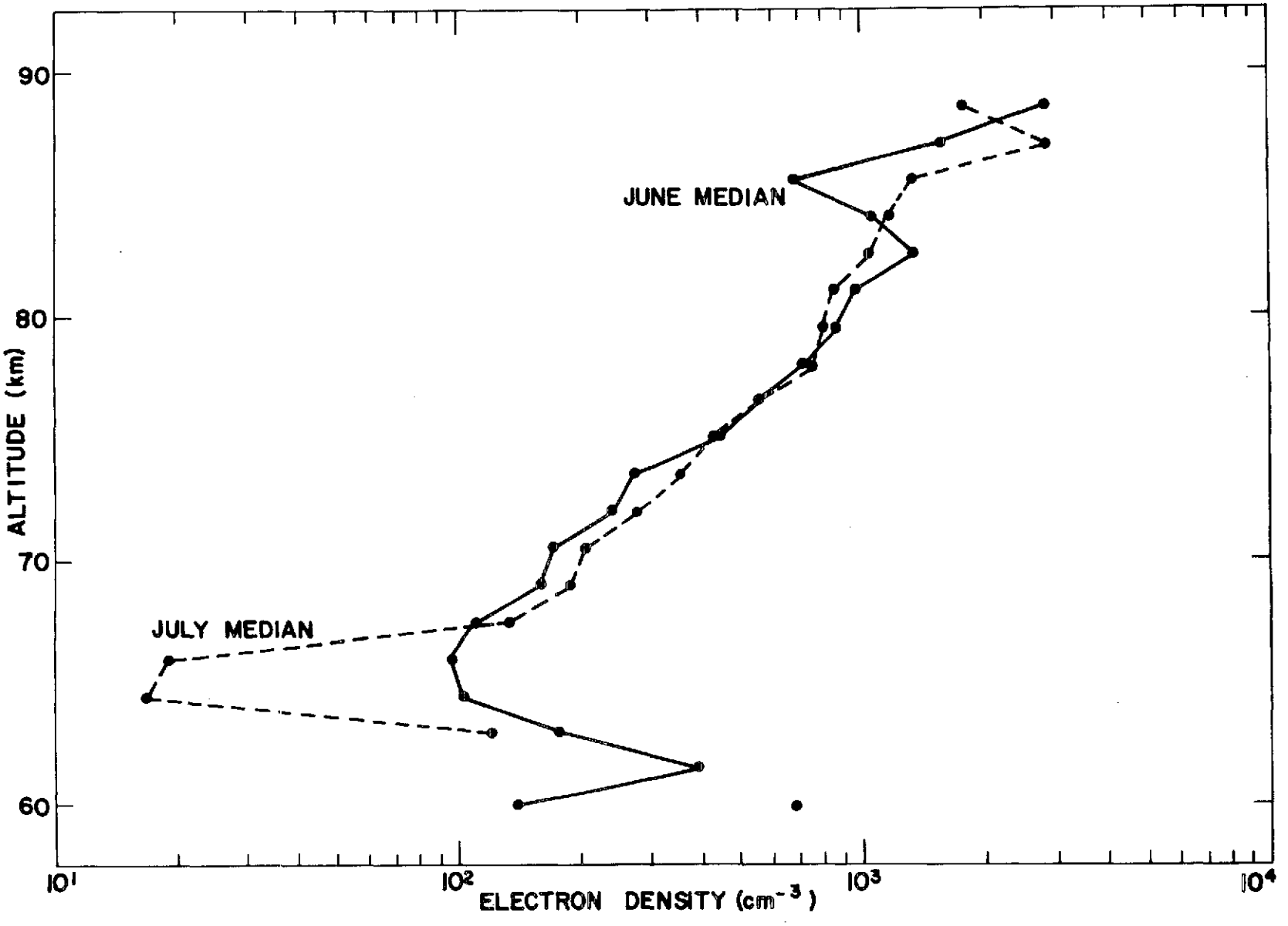

Figure 4.19 Median electron-density profiles for June, 1973 and July, 1973.

electron densities of the March and April profiles are about the same; then, a slight decrease occurred from April to June. The June and December profiles show that between 65 and 80 km the summer electron densities during the day are from a factor of 1.5 to 4 times larger than the winter electron densities; this agrees well with rocket results shown in Figure 1.5.

4.6 *Diurnal Electron-Density Variations*

On December 21, 1972, March 21, 1973, and June 21, 1973, diurnal partial-reflection measurements were made as shown in Figures 4.20, 4.21, and 4.22. The quantities plotted in these figures are similar to those in Figures 4.1 to 4.8 except they were determined on an hourly basis rather than daily. The dashed sections in the electron-density curves at 72 and 76.5 km indicate that the background noise was too high around sunrise and sunset for accurate measurements.

On June 21, the electron densities of Figure 4.22 had a relatively smooth variation with solar zenith angle. However, on December 21 the electron densities of Figure 4.20 increased very rapidly with the rising sun; then, they quickly decreased at sunset.

On March 21, a sharp increase in the electron densities of Figure 4.21 occurred near sunrise, but no decrease was observed at sunset. Apparently, the effects of particle precipitation are responsible for this observation, since *Solar-Geophysical Data* [May, 1973] reveals that the geomagnetic activity during March was most disturbed on March 19, 20, 21, 22, and 25.

4.7 *Additional Remarks*

To determine if the 10-mb height variation in Figure 4.13(a) is traveling along the 50° parallel of latitude, changes in the 10-mb height at

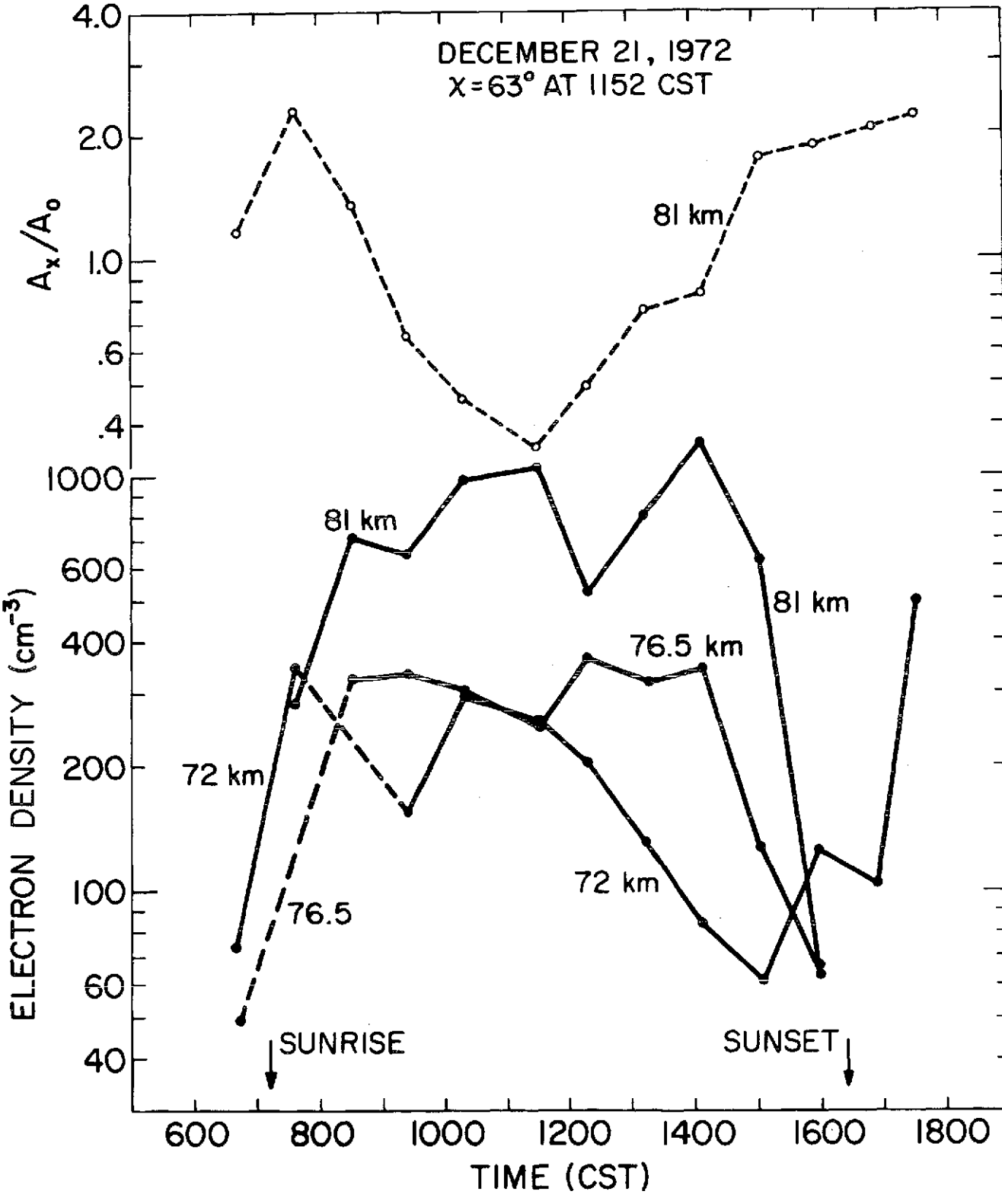

Figure 4.20 Electron density at 72, 76.5 and 81 km and A_x/A_o ratio at 81 km versus time, December 21, 1972.

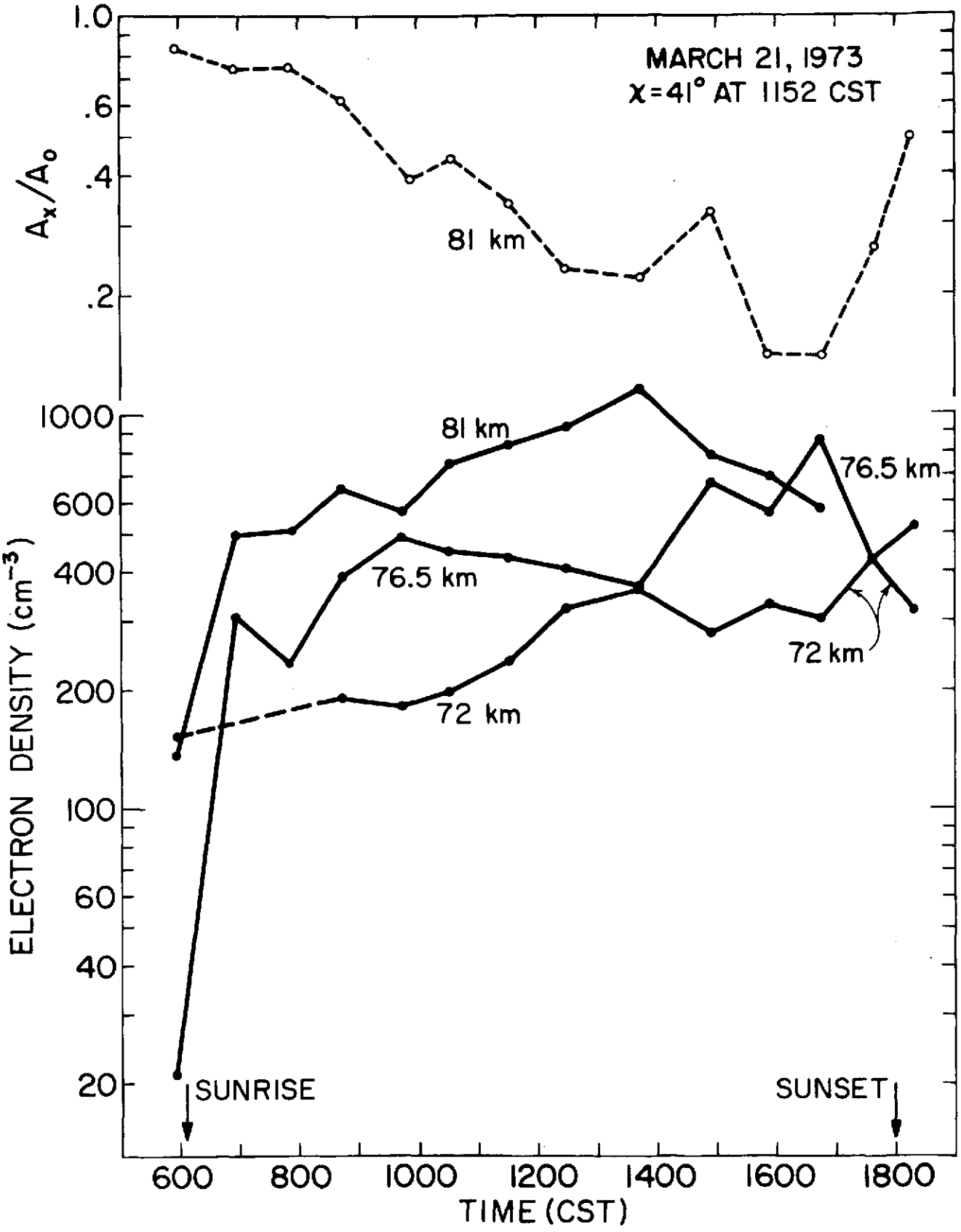

Figure 4.21 Electron density at 72, 76.5 and 81 km and A_x/A_o ratio at 81 km versus time, March 21, 1973.

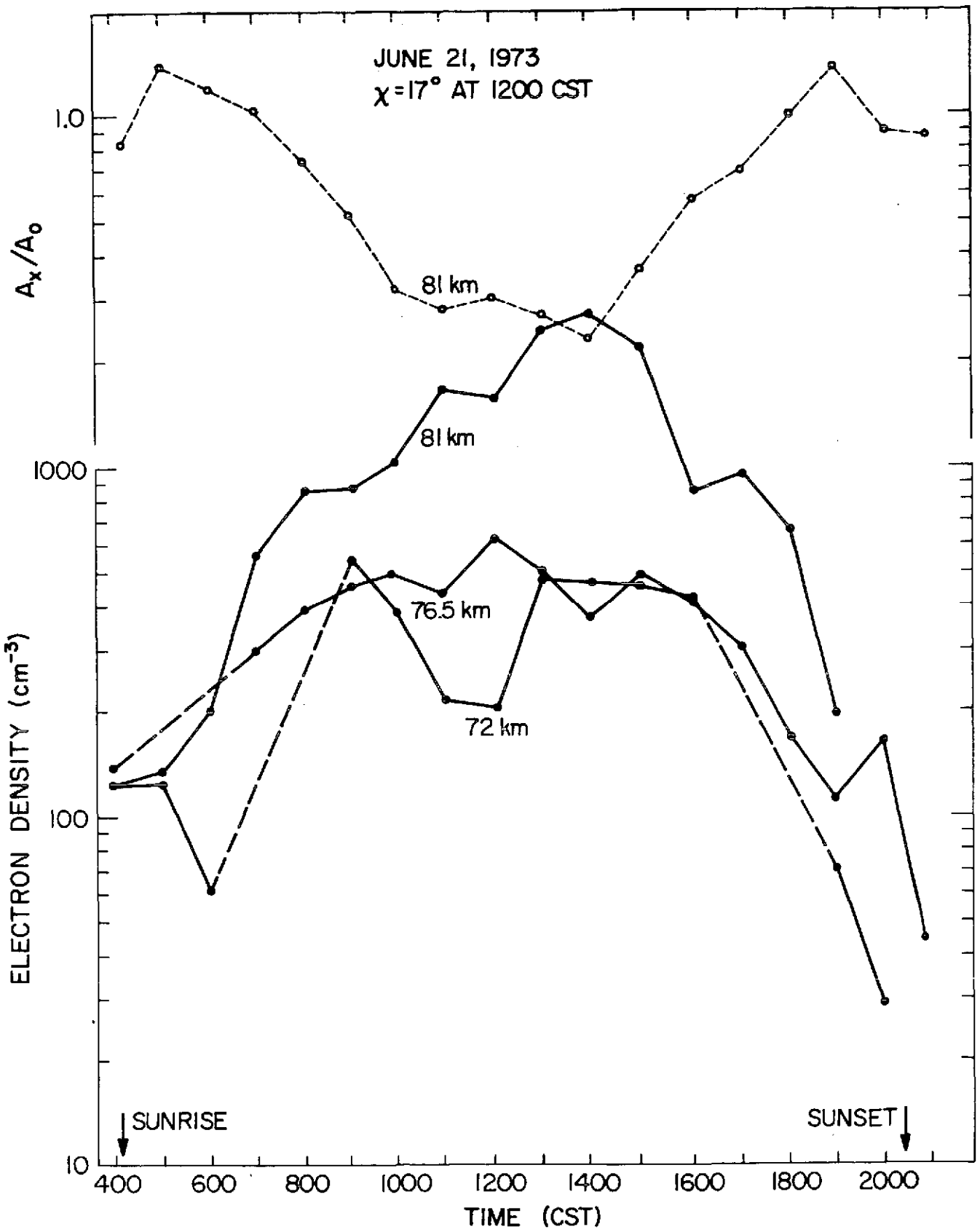

Figure 4.22 Electron density at 72, 76.5 and 81 km and A_x/A_o ratio at 81 km versus time, June 21, 1973.

50° latitude are observed at two more longitudes (70° and 110°). The 10-mb heights at these two points are read daily and numerically filtered in the manner discussed in Sections 4.2 and 4.3. Five-day running averages are determined for the height variations at the three longitudes as shown in Figure 4.23. The curves of Figure 4.23 indicate that a 10-mb height variation with a period of about 7 days is traveling westward; cross correlations between these wave-like variations indicate that its speed along the 50° parallel of latitude is about 10°/day (≈ 10 m/sec). Thus, the variation has a zonal period of about 77°.

Since Urbana is 12° west of Wallops Island and the period of the 10-mb height variation along 50° latitude is 77°, the 10-mb height deviation at the two locations will be similar at any instant in time. This may explain the close agreement between the Urbana and Wallops Island electron densities shown in Table 4.2, assuming the 10-mb height variation is responsible for the electron-density variation.

Schwentek [1973] presents some results of ionospheric absorption measurements at 16 midlatitude stations. The correlation coefficient between absorption data at each possible pair of stations is evaluated to provide a measure of the spatial correlation of winter absorption. His results, shown in Figure 4.24, indicate that the correlation coefficient decreases rapidly as the distance between stations increases; it reaches a constant level at a distance between stations of 500 km and remains significant up to 1000 km. The distance for the correlation coefficient to drop one-half of the way to the constant level is about 200 km which may be taken as the dominant scale in spatial distribution of absorption.

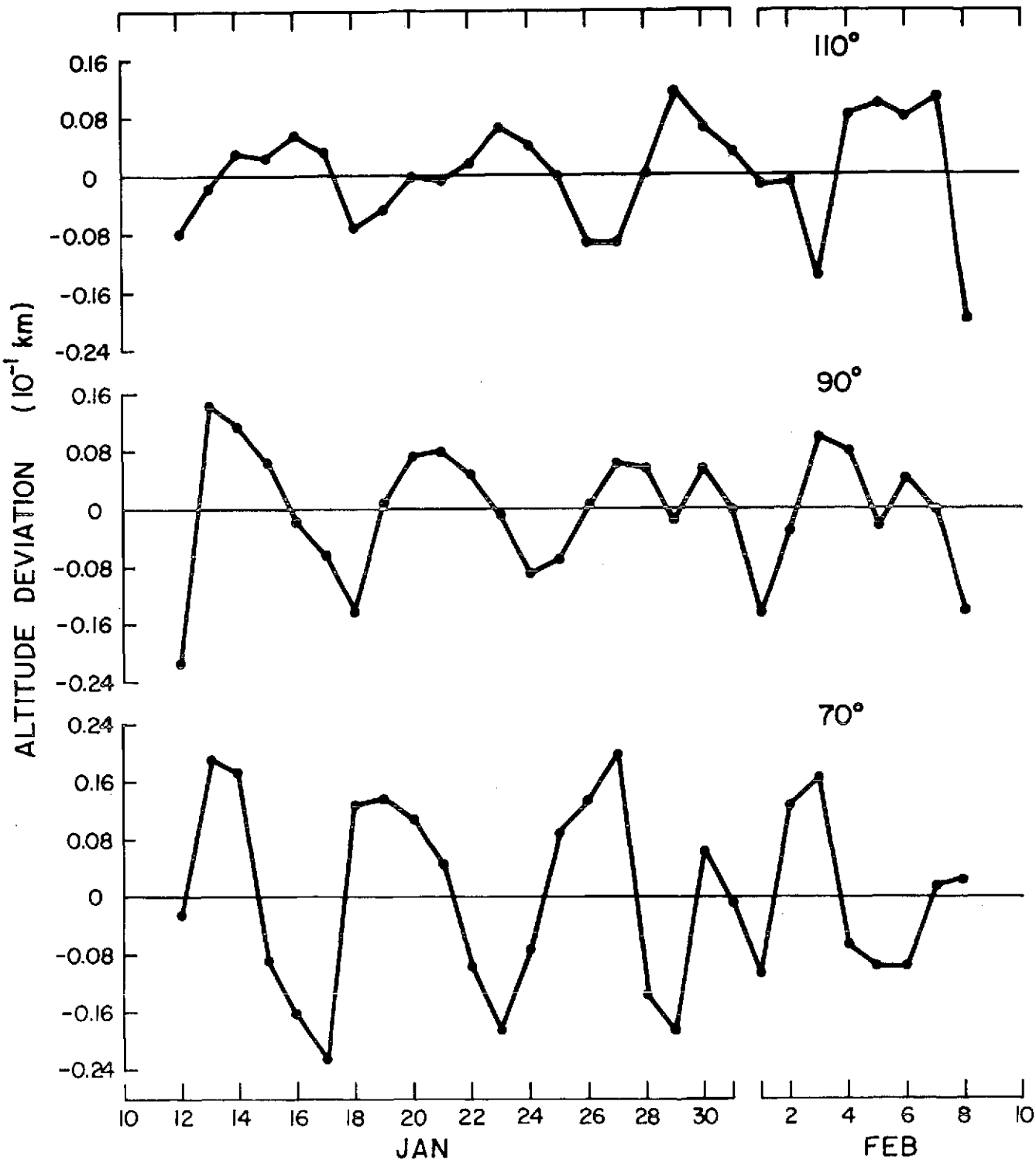

Figure 4.23 Five-day running average of the 10-mb height deviation at 50° latitude and longitudes of 70°, 90° and 100°.

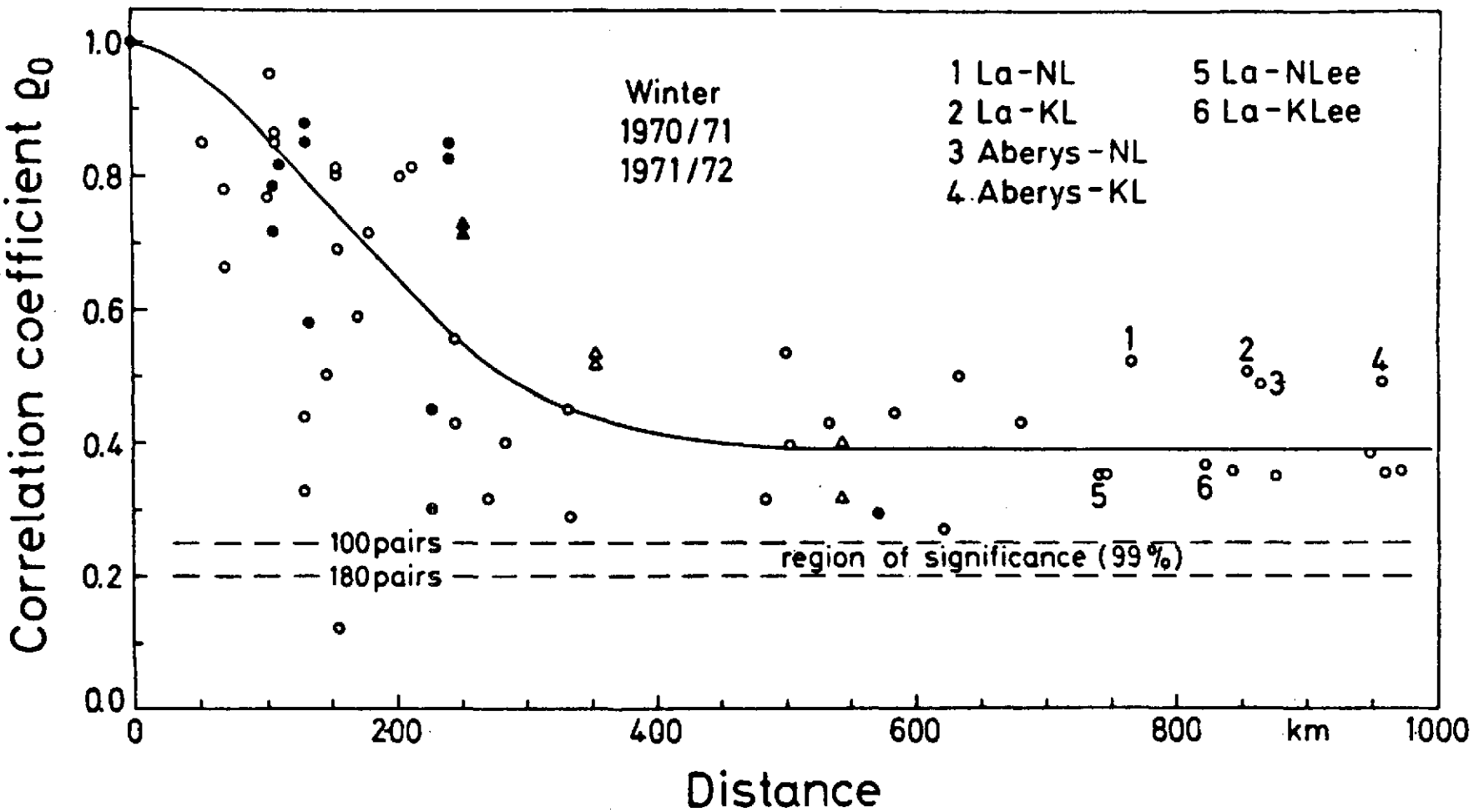

Figure 4.24 Correlation coefficient of absorption data obtained from pairs of A1 stations or A3 circuits, plotted as a function of distance between the stations, for winters 1970-71 and 1971-72. ● same frequency, ○ different frequencies, stations in Central Europe; ▲, △ stations in Japan.

The absorption measurements presented by Schwentek use the A1 or A3 technique. Both of these types of measurements are primarily indicators of ionization changes above about 82 km due to the effect of the high electron density on high-frequency radio waves at these altitudes. Thus, Schwentek's results in Figure 4.24 indicate that the winter anomaly in ionization above 82 km has a horizontal scale of about 200 km. The constant correlation coefficient from 500 to 1000 km may be explained by using the results of the electron-density comparison (Table 4.2) which indicate that the winter anomaly below 82 km extends for a horizontal scale of at least 1000 km. Ionization below 82 km affects absorption measurements to some degree, suggesting that the correlation coefficient in Figure 4.24 remains at a constant and significant level because the winter anomaly in ionization below 82 km extends over 1000 km. Thus, it appears that the winter anomaly in *D*-region ionization is divided into two types: "Type 1", above 82 km, extending horizontally for about 200 km and "Type 2", below 82 km, extending horizontally for at least 1000 km.

5. CONCLUSIONS AND SUGGESTIONS FOR FUTURE WORK

Techniques for studying the seasonal and daily variability of the *D* region involve the measurement of absorption suffered by a high-frequency radio wave as it travels through the ionosphere, using either vertical-incidence pulsed transmissions (the A1 technique) or oblique-incidence cw transmissions over paths sufficiently long that the ground wave may be neglected (the A3 technique). Both techniques mainly investigate the variability of the *D* region above 82 km, since the absorption of the transmissions is primarily affected by the high electron densities occurring at these altitudes. The present study, on the other hand, has investigated the *D*-region ionization variability below 82 km.

Daily measurements of the electron densities below 82 km have revealed cyclical changes occurring in the winter of 1972-3; the most pronounced wave-like variations occurred in January, 1973, during the development of a major stratospheric warming.

The technique of numerically filtering the daily measurements to determine correlations has proven to be a useful tool. It exposed cyclical variations with a period of about 5 days in the 10-mb height which prove to be highly correlated with electron-density changes at 72 and 76.5 km, further substantiating the existence of stratospheric-ionospheric coupling.

No pronounced tendency is observed for the electron density enhancements at the upper altitudes to either precede or follow those at lower altitudes. This suggests that the mechanism responsible for the winter anomaly in the *D*-region ionization applies throughout this altitude range. Comparison of measurements at Urbana and Wallops Island indicates that the horizontal scale of the winter anomaly below about 82 km is at least 1000 km. However.

Schwentek's [1973] results indicate that the horizontal scale of the winter anomaly above 82 km is about 200 km.

Partial-reflection measurements similar to those presented in this study need to be continued; this will enable further investigation of the wave-like variations observed in the *D*-region electron densities during winter. Absorption measurements which are an indication of ionization changes above about 82 km need to be used with the partial-reflection measurements to further investigate the relationship between the Type 1 and Type 2 anomalies.

Several improvements of the partial-reflection system are recommended. Below approximately 70 km, the signal-to-noise ratio of the Urbana system is poor, causing unreliable electron densities. This problem also occurs in the diurnal measurements at higher altitudes around sunrise and sunset. Higher transmitter power or improvements in the noise-defeating algorithm, such as using a weighting function to place more emphasis on strong reflections, would alleviate this problem.

Above about 82 km, the A_x/A_o ratio is very difficult to measure accurately due to high absorption. Simultaneous measurements at a higher frequency would improve results. Also, implementation of the differential-phase measuring system of *Wiersma and Sechrist* [1972] would permit the calculation of electron densities at the higher altitudes where Faraday rotation of the partially-reflected waves occurs.

The current partial-reflection system requires an operator during the entire hourly collection periods. By using the digital input/output device recently acquired by the Aeronomy Laboratory, much of the burden now placed on the operator can be eliminated. Longer measuring periods would be more convenient.

REFERENCES

Appleton, E. V. (1927), URSI Reports, Washington Assembly.

Appleton, E. V. (1937), Regularities and irregularities in the ionosphere, *Proc. Roy. Soc.*, London, *162*, 451-478.

Appleton, E. V. and W. R. Piggott (1948), Ionospheric absorption measurements throughout a sunspot cycle, *Proc. International Scientific Radio Union*, *7*, 320.

Appleton, E. V. and W. R. Piggott (1954), Ionospheric absorption measurements during a sunspot cycle, *J. Atmos. Terr. Phys.*, *5*, 141-172.

Bean, T. A. and S. A. Bowhill (1973), Analysis of partial-reflection data from the solar eclipse of July 10, 1972, *Aeron. Rep. 55*, Aeron. Lab., Dep. Elec. Eng., Univ. Ill., Urbana-Champaign.

Belrose, J. S. (1970), Radio wave probing of the ionosphere by the partial reflection of radio waves (from heights below 100 km), *J. Atmos. Terr. Phys.*, *32*, 567-596.

Belrose, J. S., I. A. Bourne, and L. W. Hewitt (1966), The winter variability of electron density in the lower ionosphere over Ottawa. A discussion of results and possible causes, *Electron Density Profiles in the Ionosphere and Exosphere*, (Ed.) J. Frihagen, North-Holland Pub. Co., Amsterdam.

Belrose, J. S. and M. J. Burke (1964), Study of the lower ionosphere using partial reflections, experimental technique and methods of analysis, *J. Geophys. Res.*, *69*, 2799-2818.

Belrose, J. S. and L. Thomas (1968), Ionization changes in the middle latitude *D*-region associated with geomagnetic storms, *J. Atmos. Terr. Phys.*, *30*, 1397-1413.

Berkowitz, J., W. A. Chupka, and D. G. Gutman (1971), Electron affinities of O_2, O_3, NO, NO_2, NO_3 by endothermic charge transfer, *J. Chem. Phys.*, *55*, 2733-2745.

Beynon, W. J. G. and K. Davies (1954), A study of vertical incidence ionospheric absorption at 2 mc/s. *Proc. Conf. Phys. Ionosphere*, Physical Society, London, 40-52.

Birley, M. H. and C. F. Sechrist, J. (1971), Partial-reflection data collection and processing using a small computer, *Aeron. Rep. 42*, Aeron. Lab., Dep. Elec. Eng., Univ. Ill., Urbana-Champaign.

Bossolasco, M. and A. Elena (1963), Absorption de la cauche *D* et témperature de la mésosphère, *C. R. Acad. Sci.*, Paris, *256*, 4491-4493.

Bourne, I. A. and L. W. Hewitt (1968), The dependence of ionospheric absorption of MF radio waves at mid-latitudes on planetary magnetic activity, *J. Atmos. Terr. Phys.*, *30*, 1381-1395.

Bowhill, S. A. (1969), *D*-region morphology and processes, from in Meteorological and Chemical Factors in *D*-Region Aeronomy--Record of the Third Aeronomy Conference, (Ed.) C. F. Sechrist, Jr., *Aeron. Rep. 32*, Aeron. Lab., Dep. Elec. Eng., Univ. Ill., Urbana-Champaign.

Bowhill, S. A. and B. W. Denny (1973), *D*-region electron-density variations during winter 1972-3, Summary of paper presented at COSPAR, Konstanz, F.R.G.

Budden, K. G. (1961), *Radio Waves in the Ionosphere*, University Press, Cambridge.

Chapman, G. E. (1969), Stratospheric-mesospheric circulation patterns and *D*-region absorption, *Rep. No. 22*, Planetary Circulations Project, Dept. of Meteor., MIT.

Chapman, S. (1931), The absorption and dissociative or ionizing effect of monochromatic radiation in an atmosphere on a rotating earth, *Proc. Phys. Soc.*, London, *43*, 26-45.

Charney, J. G. and P. G. Drazin (1961), Propagation of planetary scale disturbances from the lower into the upper atmosphere, *J. Geophys. Res.*, *66*, 83-110.

Christie, A. D. (1970), *D*-region winter anomaly and transport near the mesopause, *J. Atmos. Terr. Phys.*, *32*, 35-56.

Cooley, J. W. and J. W. Tukey (1965), An algorithm for the machine calculation of complex Fourier series, *Mathematics of Computations*, *19*, 297-301.

Coyne, T. N. R. and J. S. Belrose (1972), The diurnal and seasonal variation of electron densities in the mid-latitude *D* region under quiet conditions, *Radio Sci.*, *7*, 163-174.

Deeks, D. G. (1965), *D*-region electron distributions in middle latitudes deduced from the reflections of long radio waves, Internal Memorandum No. 219, Radio and Space Research Station (privately circulated).

Deland, R. J. and R. M. Friedman (1972), Correlation of fluctuations of ionospheric absorption and atmospheric planetary scale waves, *J. Atmos. Terr. Phys.*, *34*, 295-304.

Dickinson, R. E. (1968a), On the exact and approximate linear theory of vertically propagating Rossby waves forced at a spherical lower boundary, *Mon. Wea. Rev.*, *96*, 405-415.

Dickinson, R. E. (1968b), Planetary Rossby waves propagating vertically through weak westerly wind wave guides, *J. Atmos. Sci.*, *25*, 984-1002.

Dickinson, R. E. (1969), Vertical propagation of planetary Rossby waves through an atmosphere with Newtonian cooling, *J. Geophys. Res.*, *74*, 929-938.

Dieminger, W. (1952), On the causes of excessive absorption in the ionosphere on winter days, *J. Atmos. Terr. Phys.*, *2*, 340.

Donahue, T. M. (1972), Positive ion chemistry of the *D* and *E* regions, *Radio Sci.*, *7*, 73-80.

Edwards, B. (Ed.) (1971), Research in Aeronomy, *Prog. Rep. 71-2*, Aeron. Lab., Dep. Elec. Eng., Univ. Ill., Urbana-Champaign, 112-119.

Fejer, J. A. and R. W. Vice (1959), An investigation of the ionospheric *D*-region, *J. Atmos. Terr. Phys.*, *16*, 291-306.

Ferguson, E. E. (1972), *D*-region negative-ion chemistry, from COSPAR symposium record, (Eds.) C. F. Sechrist, Jr., and M. A. Geller, *Aeron. Rep. 48*, Aeron. Lab., Dep. Elec. Eng., Univ. Ill., Urbana-Champaign.

Friedman, H. (1960), *Physics of the Upper Atmosphere*, (Ed.) J. A. Ratcliffe, Academic Press, New York.

Ganguly, S. (1972), Some results of absorption measurements at a low latitude station, *J. Atmos. Terr. Phys.*, *34*, 2009-2023.

Gardner, F. F. and J. L. Pawsey (1953), Study of the ionospheric *D*-region using partial reflections, *J. Atmos. Terr. Phys.*, *3*, 321-344.

Geisler, J. E. and R. E. Dickinson (1968), Vertical motions and nitric oxide in the upper mesosphere, *J. Atmos. Terr. Phys.*, *30*, 1501-1521.

Geller, M. A. and C. F. Sechrist, Jr. (1971), Coordinated rocket measurements on the *D*-region winter anomaly--II. Some implications, *J. Atmos. Terr. Phys.*, *33*, 1027-1039.

Gregory, J. B. (1965), The influence of atmospheric circulation on mesospheric electron densities in winter, *J. Atmos. Sci.*, *22*, 18-23.

Gregory, J. B. and A. H. Manson (1969a), Seasonal variations of electron densities below 100 km at mid-latitudes--I. Differential absorption measurements, *J. Atmos. Terr. Phys.*, *31*, 683-701.

Gregory, J. B. and A. H. Manson (1969b), Seasonal variations of electron densities below 100 km at mid-latitudes--II. Electron densities and atmospheric circulation, *J. Atmos. Terr. Phys.*, *31*, 703-729.

Gregory, J. B. and A. H. Manson (1970), Seasonal variations of electron densities below 100 km at mid-latitudes--III. Stratospheric-ionospheric coupling, *J. Atmos. Terr. Phys.*, *32*, 837-852.

Hartree, D. R. (1929), The propagation of electro-magnetic waves in a stratified medium, *Proc. Camb. Phil. Soc.*, *25*, 97-120.

Henry, Jr., G. W. (1966), Instrumentation and preliminary results from shipboard measurements of vertical incidence ionospheric absorption, *Aeron. Rep. 13*, Aeron. Lab., Dep. Elec. Eng., Univ. Ill., Urbana-Champaign.

Holt, O. (1963), Some experimental studies of the ionospheric *D* region at high latitudes, Norwegian Defence Research Establishment, *Rep. No. 46*.

IBM System/360 Scientific Subroutine Package (360A-CM-03X), Version III, Programmer's Manual (H20-0205-3).

Kellogg, W. W. (1961), Chemical heating above the polar mesopause in winter, *J. Met.*, *18*, 373-381.

Lodato, R. F. and E. A. Mechtly (1971), Rocket measurements of electron collision frequency, *Aeron. Rep. 45*, Aeron. Lab., Dep. Elec. Eng., Univ. Ill., Urbana-Champaign.

Maehlum, B. (1967), On the 'Winter Anomaly' in the mid-latitude *D* region, *J. Geophys. Res.*, *72*, 2287-2299.

Manson, A. H. and M. W. J. Merry (1970), Particle influx and the 'Winter Anomaly' in the mid-latitude (L = 2.5 - 3.5) lower ionosphere, *J. Atmos. Terr. Phys.*, *32*, 1169-1181.

Matheson, R. J. (1971), High-impedance driver boost detector's dynamic range, *Electronics*, *44*, *(22)*, 79.

Mechtly, E. A., S. A. Bowhill, L. G. Smith, and H. W. Knoebel (1967), Lower ionosphere electron concentration and collision frequency from rocket measurements of Faraday rotation, differential absorption, and probe current, *J. Geophys. Res.*, *72*, 5239-5245.

Mechtly, E. A., S. A. Bowhill, and L. G. Smith (1972), Changes of lower ionosphere electron concentrations with solar activity, *J. Atmos. Terr. Phys.*, *34*, 1899-1907.

Mechtly, E. A. and L. G. Smith (1968), Seasonal variation of the lower ionosphere at Wallops Island during the IQSY, *J. Atmos. Terr. Phys.*, *30*, 1555-1561.

Mechtly, E. A., L. G. Smith, and G. W. Henry (1973), Rocket observations of the winter anomaly, Summary of paper presented at COSPAR, Konstanz, F.R.G.

Narcisi, R. S. and A. D. Bailey (1965), Mass spectrometric measurements of positive ions at altitudes from 64 to 112 kilometers, *J. Geophys. Res.*, *70*, 3687-3700.

Newell, R. E. (1968), The general circulation of the atmosphere above 60 km, *Meteorological Monographs*, *9*, *(31)*, American Meteorological Society, 98-113.

Newell, R. E., J. M. Wallace and J. R. Mahoney (1966), The general circulation of the atmosphere and its effect on the movement of trace substances, *Tellus*, *18*, 363-380.

Nicolet, M. (1965), Nitrogen oxides in the chemosphere, *J. Geophys. Res.*, *70*, 679-689.

Phelps, A. V. and J. L. Pack (1959), Electron collision frequencies in nitrogen and the lower ionosphere, *Phys. Rev. Letters*, *3*, 340-342.

Pirnat, C. and S. A. Bowhill (1968), Electron densities in the lower ionosphere deduced from partial reflection measurements, *Aeron. Rep. 29*, Aeron. Lab., Dep. Elec. Eng., Univ. Ill., Urbana-Champaign.

Ratcliffe, J. A. (1972), *An Introduction to the Ionosphere and Magnetosphere*, Cambridge University Press.

Reid, G. C. (1970), Production and loss of electrons in the quiet daytime *D* region of the ionosphere, *J. Geophys. Res., 75*, 2551-2562.

Reynolds, D. A. and C. F. Sechrist, Jr. (1970), Measurement of average electron density between 75 and 80 kilometers, *Aeron. Rep. 36*, Aeron. Lab., Dep. Elec. Eng., Univ. Ill., Urbana-Champaign.

Schwentek, H. (1973), Some results obtained from the European Cooperation concerning studies of the winter anomaly in ionospheric absorption, Summary of paper presented at COSPAR, Konstanz, F.R.G.

Sechrist, Jr., C. F. (1967), A theory of the winter absorption anomaly at middle latitudes, *J. Atmos. Terr. Phys., 29*, 113-136.

Sechrist, Jr., C. F. (1970), Interpretation of *D*-region electron densities, *Radio Sci., 5*, 663-671.

Sechrist, C. F., E. A. Mechtly, J. S. Shirke, and J. S. Theon (1969), Coordinated rocket measurements on the *D*-region winter anomaly--I. Experimental results, *J. Atmos. Terr. Phys., 31*, 145-153.

Sen, H. K. and A. A. Wyller (1960), On the generalization of the Appleton-Hartree magnetoionic formulas, *J. Geophys. Res., 65*, 3931-3950.

Shapley, A. H. and W. J. G. Beynon (1965), "Winter anomaly" in ionospheric absorption and stratospheric warmings, *Nature*, London, *206*, 1242.

Shirke, J. (1961), Ionospheric absorption on 2.5/2.6 Mc/s at Ahmedabad, *Proc. IGY Symposium, 1*, 142-148.

Solar-Geophysical Data, Part I (Prompt Reports), a United States Department of Commerce Publication, Boulder, Colorado, May, 1973, *No. 345*.

Thomas, L. (1971), The lower ionosphere, *J. Atmos. Terr. Phys.*, *33*, 157-196.

Thomas, L. (1962), The winter anomaly in ionospheric absorption, in *Radio Wave Absorption in the Ionosphere*, (Ed.) N. C. Gerson, Pergammon Press, New York, 301-317.

Thrane, E. V. (1969), Diurnal variation of electron production rates in the *D* region, *J. Geophys. Res.*, *74*, 1311-1316.

Thrane, E. V., A. Haug, B. Bjelland, M. Anastassiades, E. Tsagakis (1968), Measurements of the *D*-region electron densities during the International Quiet Sun Years, *J. Atmos. Terr. Phys.*, *30*, 135-150.

Whitten, R. C. and I. G. Poppoff (1971), *Fundamentals of Aeronomy*, John Wiley & Sons, Inc., New York.

Wiersma, D. J. and C. F. Sechrist, Jr. (1972), Differential phase measurements of *D*-region partial reflections, *Aeron. Rep. 47*, Aeron. Lab., Dep. Elec. Eng., Univ. Ill., Urbana-Champaign.

APPENDIX I

Electron attachment, detachment, and negative ion-molecule reactions considered in Figure 1.4.

	Reaction	Rate Constant (c.g.s. units*)
1.	$e + O_2 + O_2 \rightarrow O_2^- + O_2$	1.6×10^{-30}
2.	$O_2^- + O \rightarrow O_3 + e$	3.3×10^{-10}
3.	$O_2^- + O_2(^1\Delta_g) \rightarrow 2\ O_2 + e$	2.0×10^{-10}
4.	$O_2^- + O_3 \rightarrow O_3^- + O_2$	3.0×10^{-10}
5.	$O_3^- + NO \rightarrow NO_3^- + O$	1.0×10^{-11}
6.	$O_3^- + CO_2 \rightarrow CO_3^- + O_2$	4.0×10^{-10}
7.	$CO_3^- + O \rightarrow O_2^- + CO_2$	8.0×10^{-11}
8.	$CO_3^- + NO \rightarrow NO_2^- + CO_2$	9.0×10^{-12}
9.	$NO_2^- + O_3 \rightarrow NO_3^- + O_2$	1.8×10^{-11}
10.	$O_2^- + O_2 + M \rightarrow O_4^- + M$	$> 10^{-30}$
11.	$O_4^- + O \rightarrow O_3^- + O_2$	4.0×10^{-10}
12.	$O_4^- + CO_2 \rightarrow CO_4^- + O_2$	4.3×10^{-10}
13.	$O_4^- + NO \rightarrow NO_3^- + O_2$	2.5×10^{-10}
14.	$CO_4^- + O \rightarrow CO_3^- + O_2$	1.5×10^{-10}
15.	$CO_4^- + NO \rightarrow NO_3^- + CO_2$	4.8×10^{-11}
16.	$O_2^- + NO_2 \rightarrow NO_2^- + O_2$	8.0×10^{-10}
17.	$CO_3^- + NO_2 \rightarrow NO_3^- + CO_2$	8.0×10^{-11}

*2-body rate constants in $cm^6\ sec^{-1}$

3-body rate constants in $cm^9\ sec^{-1}$